Semiconductor Corrugated Ridge Waveguide Distributed Feedback Lasers: Experimental Characterization and Design Considerations

Kais Dridi

A thesis submitted to the
Faculty of Graduate and Postdoctoral Studies
in partial fulfillment of the requirements for the degree of
Doctor of Philosophy
in Electrical Engineering and Computer Science

Ottawa-Carleton Institute for Electrical and Computer Engineering
School of Electrical Engineering and Computer Science
Faculty of Engineering
University of Ottawa

Abstract

Semiconductor corrugated ridge waveguide (CRW) distributed feedback (DFB) lasers offer compelling advantages over standard DFB lasers. Indeed, the use of surface gratings etched on the ridge waveguide sidewalls in CRW-DFB devices avoids any epitaxial overgrowth. This provides a considerable simplification in the fabrication process, reducing cost and time of manufacturing, and ultimately increasing yield. It offers also the potential for monolithic integration with other devices, paving the way towards low-cost and mass-production of photonics integrated circuits. In recent years, the re-consideration of growth-free DFB lasers has drawn considerable attention, particularly with the current state-of-the-art photolithography machines. In this work, we present an experimental investigation on two generations of InGaAsP/InP multiple-quantum-well (MQW) CRW-DFB lasers that have been fabricated using stepper lithography. An early developed 1310 nm CRW-DFB laser showed stable single mode with high side-mode suppression ratios (SMSR) (>50 dB), albeit with thresholds higher than anticipated. A subsequent single-mode 1550 nm CRW-DFB laser showed stable operation with SMSR (>50 dB) and narrow spectral linewidths (≤250 kHz), observed for a wide range of current injection. Besides, novel multi-electrode CRW-DFB lasers have been tested. The experimental investigation showed that narrower linewidth (<150 kHz) and wide wavelength tunability (>3 nm) have been recorded using different multi-electrode current injection configurations.

The application of a time-domain modeling approach for semiconductor CRW-DFB lasers is then described for the first time. We numerically studied the effect of the radiation modes on CRW-DFB laser properties by using time-domain coupled wave equations. High-order corrugated gratings with λ/4 phase-shit were analyzed, where the degree of longitudinal spatial hole burning (LSHB) can be effectively reduced by means of fine tuning of the grating duty cycle. Additionally, we showed how the side-mode suppression ratio can be predicted depending on the device geometry.

Acknowledgments

First and foremost, I would like to thank Almighty ALLAH for giving me the health, patience, and strength to accomplish my graduate studies at the Centre for Research in Photonics (Photonic Technology Laboratory at the University of Ottawa).

I would like to take this chance to express my sincere appreciations to all people who offered guidance and support in the last few years. Especially, I would like to express my gratitude to my supervisor, Prof. Trevor J. Hall, for his support and patience. I am also grateful to Prof. Hall for providing the financial support, which partially made this work possible. Aside from collaborating with many academic and industrial partners, I would like also to emphasize on the fact that Prof Hall gave me a large space to think freely and to develop a self-attitude towards problem solving. Great thanks are as well dedicated to Dr. Karin Hinzer, who gave me a lot of encouragement and advices. I really appreciated working with her.

Many thanks also go to all my colleagues and friends at the photonic technology laboratory and CRPuO for their kindness and help. I would like to especially thank my colleagues Dominic Olivier and Hassan Teimoori who initiated me to the photonic laboratory environment, Ronald Millet for the initial training on devices test and measurement, and Abdessamad Benhsaien for sharing his experience, and for his valuable discussions and advices.

Finally, it is my great pleasure to say thank you to my entire family, who have always been there when I have needed them.

Publications

The following publications are on work directly covered in this thesis:

Papers in refereed journals

1. K. Dridi, A. Benhsaien, J .Zhang, and T. J. Hall, "Narrow linewidth 1560 nm InGaAsP split-contact corrugated ridge waveguide DFB lasers," Optics Letters, vol. 39, no. 21, pp. 6197-6200, Nov. 2014.
2. K. Dridi, A. Benhsaien, J. Zhang, K. Hinzer, and T. J. Hall, "Narrow linewidth two-electrode 1560 nm laterally coupled distributed feedback lasers with third-order surface etched gratings," Optics Express, vol. 22, no. 16, pp. 19087-19097, Aug. 2014.
3. K. Dridi, A. Benhsaien, J. Zhang, and T. J. Hall, "Narrow Linewidth 1550 nm Corrugated Ridge Waveguide DFB Lasers," IEEE Photonics Technology Letters, vol. 26, no. 12, pp. 1192-1195, Jun. 2014.
4. A. Akrout, K. Dridi, and T. J. Hall, "Dynamic Analysis of High-Order Laterally Coupled DFB Lasers Using Time-Domain Traveling-Wave Model," IEEE Journal of Quantum Electronics, vol. 48, no. 10, pp. 1252-1258, Oct. 2012.
5. R. Millett, K. Dridi, A. Benhsaien, H. Schriemer, K. Hinzer, T. Hall, "Fabrication-tolerant 1310 nm laterally coupled distributed feedback lasers with high side mode suppression ratios", Photonics and Nanostructures - Fundamentals and Applications, vol. 9, no. 2, pp. 111-118, Apr. 2011.

The following publications were also produced during my PhD studies but are not directly related to the thesis scope:

6. A. Akrout, K. Dridi, S. Abdul-Majid, J. Seregelyi, and T. J. Hall, "Numerical Study of Dual Mode Generation Using a Sampled-Grating High-Order Quantum-Dot Based Laterally-Coupled DFB Laser," IEEE Journal of Quantum Electronics, vol. 49, no. 10, pp. 821-828, Oct. 2013
7. A. Akrout, K. Dridi, A. Benhsaien, and T. J. Hall, "Time-Domain Analysis of Third-Order Quantum-Dot-Based Laterally-Coupled Distributed Feedback Lasers Using Travelling-Wave Approach," IEEE Journal of Quantum Electronics, vol. 49, no. 5, pp. 491-498, May 2013.

Papers in refereed conference proceedings

1. Abdessamad Benhsaien, Kais Dridi, Jessica Zhang, Trevor J. Hall, "Multi-electrode laterally coupled distributed feedback InGaAsP/InP lasers: a prescription for longitudinal mode control", Proc. SPIE 8915, 891510, Oct. 2013.

2. Kais Dridi, Abdessamad Benhsaien, Akram Akrout, Jessica Zhang, and Trevor J. Hall, "Narrow-linewidth three-electrode regrowth-free semiconductor DFB lasers with uniform surface grating", Proceedings of SPIE Vol. 8640, 864009, Mar. 2013.
3. Akram Akrout, Kais Dridi, Trevor J. Hall, "Dynamic analysis of high-order quantum dot based laterally-coupled distributed feedback lasers", Proceedings of SPIE Vol. 8619, 861911, Mar. 2013.
4. K. Dridi, A. Benhsaien, J. Zhang, and T. J. Hall, "Narrow-Linewidth and Single-Mode 1.55 μm Laterally-Coupled Distributed Feedback Laser Fabricated By Standard I-Line Stepper Lithography," in Asia Communications and Photonics Conference, OSA Technical Digest (online) (Optical Society of America, 2012), paper ATh2B.5.
5. K. Dridi, R. Maldonado-Basilio, A. Benhsaien, X. Zhang, and T. Hall, "Low-Threshold and Narrow Linewidth Two-Electrode MQW Laterally Coupled Distributed Feedback Lasers at 1550 nm," in European Conference and Exhibition on Optical Communication, OSA Technical Digest (online) (Optical Society of America, 2012), paper Mo.1.E.4.
6. A. Akrout, K. Dridi, and T. Hall, "Time-Domain Analysis of High-Order Laterally-Coupled DFB Lasers," in Integrated Photonics Research, Silicon and Nanophotonics, OSA Technical Digest (online) (Optical Society of America, 2012), paper IM4B.7.
7. Kais Dridi, Abdessamad Benhsaien, Jessica Zhang, and Trevor Hall, "1.55 μm laterally coupled ridge-waveguide DFB lasers with third-order surface grating," Proc. SPIE 8412, Photonics North 2012, 84121R, Oct. 2012.
8. Akram Akrout, Kais Dridi, Trevor J. Hall, "Investigation of longitudinal spatial-hole burning in high-order laterally coupled distributed feedback lasers", Proc. SPIE 8412, Photonics North 2012, 841219, Oct. 2012.
9. R. Millett, K. Dridi, A. Benhsaien, H. Schriemer, K. Hinzer, and T. Hall, "Fabrication-tolerant 1310 nm laterally-coupled distributed feedback lasers with high side mode suppression ratios", American Institute of Physics (AIP) Conf. Proc. 1288, 88 (2010), DOI:10.1063/1.3521380.
10. Kais Dridi, Henry Schriemer, Karin Hinzer, and Trevor Hall, "On the performance of fabricated third order laterally coupling distributed feedback 1310nm lasers", Proc. SPIE 7750, 775013, Sep. 2010.
11. A. Assadihaghi, H. Teimoori, R. Millett, A. Benhsaien, K. Dridi, T. Hall, H. Schriemer, and K. Hinzer,"Threshold current reduction in third-order laterally coupled DFB lasers," 2nd Microsystems and Nanoelectronics Research Conference (MNRC 2009), Ottawa, Canada, pp. 21-24, 13-14 October 2009.

Poster

1. K. Dridi, A. Benhsaien, J. E. Nkanta, J. Zhang, S. Abdul-Majid, and T. J. Hall, "Multi-electrode Semiconductor Corrugated Ridge Waveguide DFB Lasers", University of Ottawa Engineering and Computer Poster Competition, Ottawa, March 2014 (**First Prize**).

Table of contents

Chapter 1 | Introduction

1.1. Motivation

The proliferation of numerous bandwidth-hungry IT consumerization based applications continues to boost the demand for higher capacity communication networks. To assuage this demand, there has been rapid growth and profound penetration of fiber optics into multi-user access networks. Indeed, passive optical networks combined with Ethernet or OFDM standards, appear as the most promising solutions in terms of bandwidth flexibility and scalability as well as cost effectiveness. A vital element in such systems is the optical transceiver, which is essentially responsible for the up and down-stream between the end users and central offices. Due to the high bit rate data exchanges, semiconductor distributed feedback (DFB) lasers have been massively deployed as source emitters and local oscillators in coherent optical communication systems. DFB laser diodes have been an essential ingredient in these applications thanks to their stable single mode operation, direct high-speed modulation capability, low power requirements, narrow linewidth, and small foot print. In the context of optical networks, the most important wavelength windows around 1310 nm and 1550 nm have driven the design of DFB lasers based on indium phosphide (InP) and other related III-V semiconductor materials. Besides, it is well known that the wavelength selectivity in these lasers is achieved through the incorporation of a periodic change of refractive index along the laser cavity. This requires having the Bragg gratings patterned and etched between two separate growth steps. It has been found that this interruption may induce technical challenges when it comes to preserve the gratings structure while ensuring high quality epitaxial regrowth. An alternative solution suggests having the selective feedback achieved after depositing all the epitaxial layers: this defines what has

been known as corrugated ridge waveguide (CRW) DFB lasers. In these devices, the gratings are patterned and etched along the sidewalls of the ridge waveguide. Doing so, both longitudinal distributed feedback and lateral optical confinement are simultaneously achieved. The elimination of any re-growth steps is therefore highly desired while seeking a great simplification in the fabrication process and keeping high performance levels. Still, the use of lithography techniques such as nanoimprint lithography and stepper lithography will open the doors for low-cost mass-production laser sources, which will be well suited to low cost photonic integrated circuits – an attractive solution for low cost optical transceivers.

For the CRW-DFB lasers to be widely deployed as an alternative solution, they must satisfy the same or better performances than conventional DFB lasers. As will be seen in this thesis, these devices showed interesting features, such as stable single-mode operation with high side mode discrimination (≥50 dB) and narrow linewidth (≤200 kHz). The application of the multi-electrode concept into the CRW-DFB lasers with uniform etched gratings enhances further the results and makes these devices more attractive for optical transceivers.

1.2. Objective

In this thesis, we propose to experimentally characterize InGaAsP/InP multiple quantum well corrugated ridge waveguide lasers at different wavelength windows. The devices used in this work have been modelled and designed using a modified coupled mode theory that has been customized to take into account the radiating partial waves, which are inherent to CRW with higher-order gratings. The devices have been fabricated using the stepper lithography and inductively-coupled plasma etching techniques at the Canadian Photonics Fabrication Centre (CPFC). The current work preliminary aims at providing a general, but rich enough picture of the optical characteristics of these CRW-DFB lasers. Moreover, the development of time-domain model based on the travelling wave approach for CRW-DFB lasers is another contribution of this thesis. The

numerical model constitutes an initial foundation for such structures to help understanding their performance. In addition, both the experimental findings and numerical model – developed within this thesis – will help optimizing these structures further in any future work.

1.3. Thesis scope and outline

This thesis is a *manuscript*-based thesis consisting of a collection of scientific articles presented in different chapters. The remainder of this document is organized as follows. Chapter 2 describes the general operation principle behind CRW-DFB lasers, before reviewing other laser designs that already exist in the literature. This includes a summary of the performance and manufacturing techniques that have been developed to date. Chapter 3 describes in its first sub-section the optical characteristics of 1310 nm CRW-DFB lasers. In the second sub-section, performances of 1550 nm CRW-DFB lasers are described. Chapter 4 presents the results of the application of the multi-electrode current injection concept into CRW-DFB lasers. Optical characteristics are described for two and three electrode lasers at 1560 nm in the first and second sub-sections, respectively. Chapter 5 describes a novel time-domain model that can be applied for CRW-DFB lasers in general. Appendix A describes the extraction of the modal gain. Appendix B gives general directions and steps on the determination and extraction of the linewidth of these lasers.

Chapter 2 |

Literature review on corrugated ridge waveguide DFB lasers

In this chapter we start by giving a general description of the operation principle behind corrugated ridge waveguide lasers, where basically the longitudinal distributed feedback and the lateral optical confinement are simultaneously achieved. It is also shown why these structures suffer from low coupling efficiencies and how the coupling strength could be enhanced. On the other hand, we show how the CRW-DFB lasers can be made and how this technology, when combined with photolithography-based fabrication techniques, can bring a simplification in the fabrication process and can ultimately lead to a cost reduction. In addition, the literature review on the CRW DFB lasers shows that these devices can be designed using different structures and materials, fabricated with different techniques, and deployed in various applications. The results in this study are useful when comparing the device performance obtained in this thesis.

2.1. Concept

Standard semiconductor distributed feedback (DFB) lasers are built based on a wavelength selective element known as the gratings. The formation of well-defined periodic gratings structure is the main challenge of DFB fabrication. Indeed, to ensure high single-mode yield with a high level of wavelength accuracy, it is of great importance to have a process that can simultaneously achieve low-damage, uniform and reproducible gratings. If we look at the DFB fabrication, we find that the gratings are defined during an interruption in the growth process, or through an etch and regrowth process. These multiple growth techniques require additional processing steps that make them more complex and difficult to implement; they are used routinely, in particular for high-

performance InGaAsP/InP based lasers for telecommunications, but are a source of yield and reliability problems. Etch and regrowth is also a significant challenge for Al-containing materials (GaAs/AlGaAs and InAlGaAs/InP) and GaSb devices. Corrugated ridge waveguide (CRW) – known also as laterally-coupled distributed feedback (LC-DFB) – lasers (Miller *et al.*, 1991) combine the advantages of Fabry-Perots (single growth) with the wavelength performance of DFB lasers. In these lasers, the periodic gratings structure is etched out of the upper growth layers that are used to form the ridge waveguide, as shown in Fig.2. 1(a). This process can be achieved once a single epitaxial growth process is done. In other words, there is no need for epitaxial regrowth or growth on corrugated layers as in DFB lasers fabrication, hence counteracting all the aforementioned shortcomings. This is in contrast with the conventional DFB lasers, where the gratings are etched near the active region, before being buried with other upper epitaxial material, as depicted in Fig.2. 1(b).

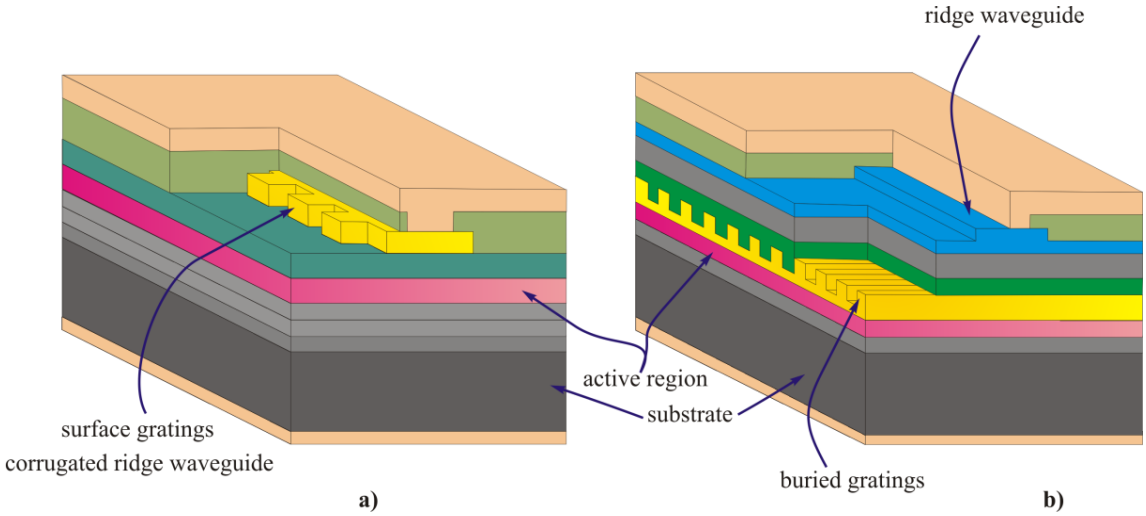

Fig.2. 1. Comparison between the placement of the Bragg gratings in (a) a corrugated ridge waveguide (CRW)-DFB laser, and (b) a conventional DFB laser.

Although an early demonstration of regrowth free DFB laser use gratings that have been etched on the ridge (Liau *et al.*, 1985), lateral gratings can be exclusively etched in the ridge sidewalls (*i.e.* corrugated ridge waveguide lasers) (Miller *et al.*, 1991), exclusively beside the ridge (Martin *et al.*, 1995) or over both

regions (Chen *et al.*, 1991). CRW-DFB lasers that use metallic rather than etched semiconductor gratings on the cladding beside the ridge have also been investigated (Kamp *et al.*, 1999; Muller *et al.*, 2001).

In this work, the gratings are patterned and etched along both sidewalls (*i.e.* sidewall gratings) of the ridge waveguide, which turns out to be corrugated along the cavity, as shown in Fig.2. 1(a). The lateral placement of these gratings results in an effective ridge waveguide where the lateral optical confinement is assured by the lower average refractive index in the gratings' region. Let n_{rd} be the refractive index of the intact portion of the gratings (ridge material) and n_{ins} the refractive index of etched portion of the gratings (insulator material). The resulting effective material index of the gratings' region can be estimated as:

$$n_{gr} = \sqrt{\gamma {n_{rd}}^2 + (1-\gamma){n_{ins}}^2} \tag{2.1}$$

The term 'γ' is the duty cycle of the gratings defined as a/Λ, where 'a' is the length of the intact portion of the gratings and Λ is the gratings' period. For example, an effective CRW can be defined with 50% duty cycle, an InP ridge (n_{rd} ~ 3.2), and an insulator material (e.g. SiO_2, n_{ins} ~ 1.45), would lead to an effective material index in the gratings' region n_{gr} of ~ 2.48, which is < 3.2. In this case the resulting effective CRW enhances the lateral (or horizontal) optical mode waveguiding. On the other hand, the vertical optical confinement of the propagating mode is due to the differences in refractive indices in the active and surrounding layers.

The periodic perturbation induced by the gratings results in Bragg reflection and a bidirectional coupling of the guided modes. The Bragg reflection generates a longitudinal optical distributed feedback, which is a wavelength dependent. It occurs when the Bragg condition (2.2) is satisfied:

$$\Lambda = \frac{p\lambda}{2n_{eff}} \tag{2.2}$$

In (2.2), 'p' is the gratings order; 'λ' is the emission wavelength of the laser, and 'n_{eff}' is the effective index of the optical waveguide mode. It is therefore evident, that in contrast to conventional DFB structures, the CRW can induce simultaneously a lateral optical confinement and a longitudinal distributed feedback.

The gratings, which have been etched with the same period on the ridge sidewalls, create a bi-directional coupling between contra-propagating waves along the gratings axis. The coupling efficiency depends on the corrugated ridge waveguide structure and is directly proportional to the overlap of the evanescent electromagnetic fields of the waveguide mode with the etched gratings, as can be clearly seen by the mode profile shown in Fig.2. 2. The coupling coefficient can be estimated as (Agrawal and Dutta, 1968):

$$\kappa = \frac{\sin(\pi p \gamma)}{p} \frac{({n_{rd}}^2 - {n_{ins}}^2)}{\lambda n_{eff}} \Gamma \qquad (2.3)$$

Where Γ is the field overlap integral between the gratings and the mode field.

Obviously a low coupling would be expected from such structure given the small interaction of the evanescent fields and the lateral gratings. To achieve acceptable performance it is important for the corrugated ridge waveguide gratings to be smooth and vertical enough to minimize scattering losses, fine enough to have the proper Bragg wavelength, and most importantly deep enough to achieve a strong coupling with the evanescent fields. In addition, optimum coupling coefficient values can be obtained by careful control of ridge parameters such as the ridge width, ridge depth, and gratings' etch depth. (Choi *et al.*, 1996; Millet *et al.*, 2008).

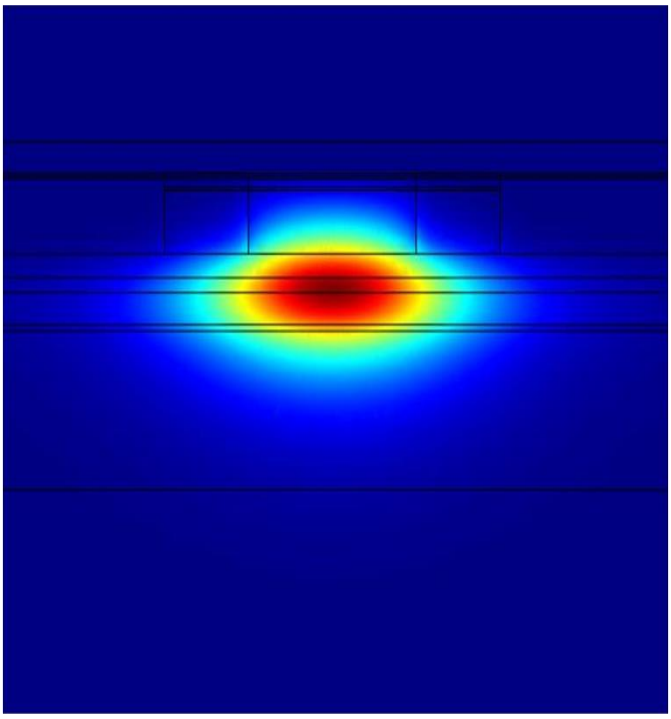

Fig.2. 2. Mode profile in the 2D cross section of a CRW-DFB laser showing the overlap between the mode and the gratings regions.

2.2. Fabrication process

The definition of the gratings can be achieved after a single epitaxial growth. In other words, there is no need for epitaxy regrowth as in DFB lasers fabrication, where there is a process interruption that may affect the performance of the fabricated device by inducing some perturbations to the interface between the gratings and the upper cladding and cap layers. This simplicity in device fabrication has been considered as a major motivator and driver for considering CRW-DFB technology since 80's. Fig.2. 3(a)-(f) illustrates the main fabrication steps required to realize conventional semiconductor DFB lasers. The process starts first by choosing a semiconductor wafer (substrate formation) depending on the targeted wavelength (*e.g.* InP substrate for 1310/1550 nm). Then semiconductor layers are grown above the substrate by means of epitaxial growth methods such as the metal organic chemical vapour-deposition (MOCVD) or the molecular-beam epitaxy (MBE).

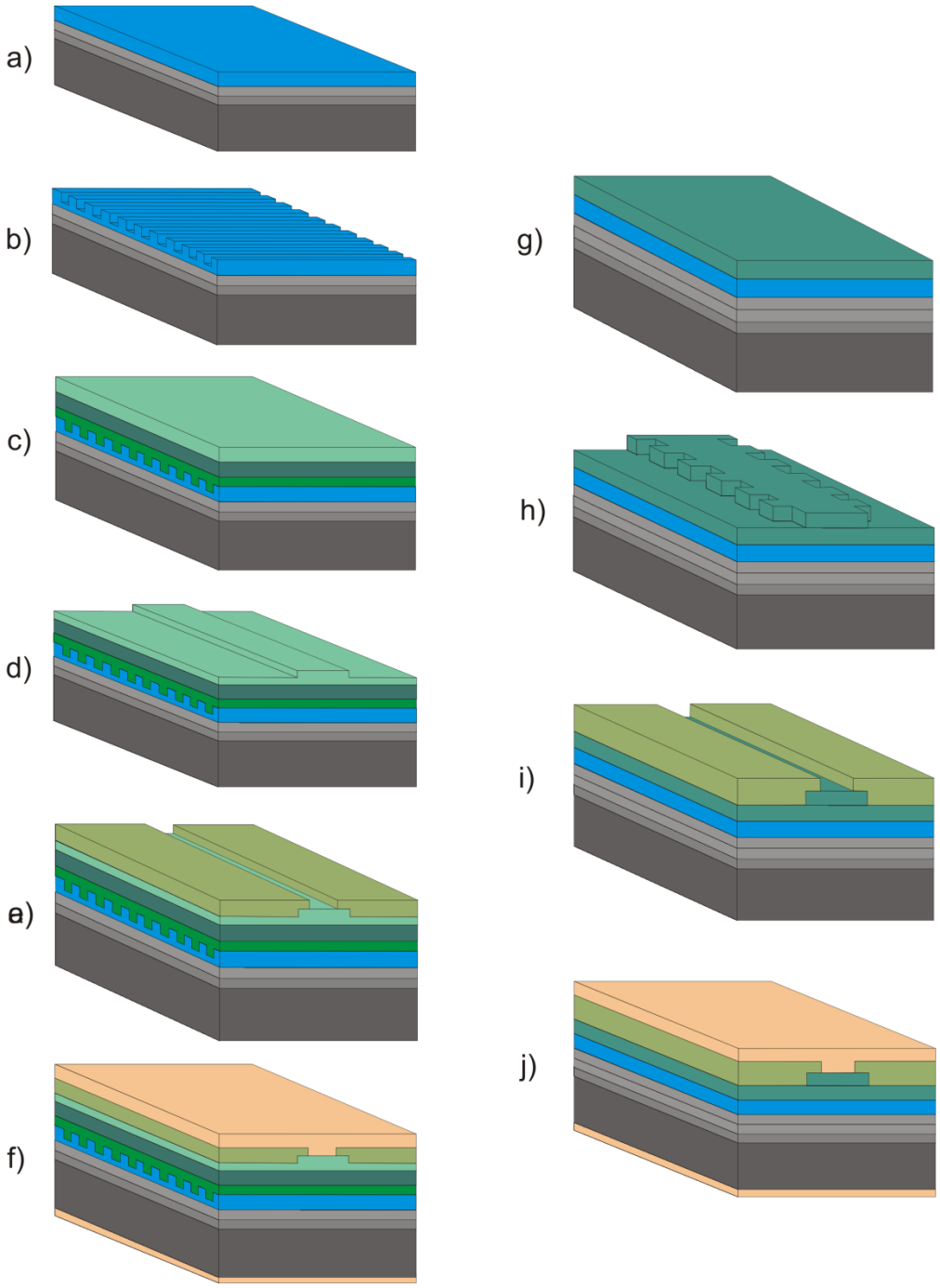

Fig.2. 3. The fabrication process of standard DFB laser: (a) Growth of lower layers, (b) etching of the gratings (c) growth of the upper material layers (regrowth), (d) waveguide etching, (e) dielectric deposition and via etch, and (f) metal deposition; and CRW-DFB laser: (g) growth of all epilayers, (h) etching of the gratings, (i) dielectric deposition and via etch, and (j) metal deposition.

These layers form the confining layers and the active layer. The former ones are responsible for the optical and electrical confinement in the active layer. The optical confinement has been explained earlier as the vertical waveguiding of the optical mode through changes in refractive index. The electrical confinement is assured by the (doped) heterostructure layers by that surround the active layer. The active gain-region can consist of a bulk material or can be formed from different material layers forming a multi-quantum well (MQW) region. Hence after growing the lower layers, the gratings – which can be lithographically defined in a resist – can be etched either below or above the gain region. Fig.2. 3(b) shows gratings that have been etched above the active region. Then the gratings are overgrown with upper material layers (*i.e.* regrowth step). Afterwards, the ridge waveguide is etched prior to electrical isolation (dielectric) layer deposition. The via-opening or contact opening can be made by means of photolithography to open a window for metal contact deposition used for electrical injection. The device is completed by the deposition of p- and n-type contacts through a metallisation evaporation process. In contrast, CRW-DFB lasers require fewer fabrication steps, as shown in Fig.2. 3 (g)-(j). In fact, all the epitaxial layers are built in one step, before the definition and etching of the CRW. An insulator is then deposited on the p-side ridge and in between the gratings' teeth. A narrow window is open in the dielectric layer as shown in Fig.2. 3(i). The contact metal layers are finally evaporated. From these steps we see how the vertical laser design (*i.e.* semiconductor layers) can be completely decoupled from the CRW structure, which is major advantage for semiconductor DFB lasers.

2.3. Literature review

As stated earlier, the elimination of any regrowth steps, which are technically very challenging particularly when it comes to the quality of the interface between the gratings and the upper cladding and cap layers, would simplify the overall fabrication process and ultimately increase the device yield. The onset of

this concept has been seen by Walpole *et al.* who demonstrated a regrowth-free distributed feedback IV-VI laser by corrugating the surface after completing all the epitaxy (Walpole *et al.*, 1976). A following first demonstration of an III-V compound semiconductors-based distributed feedback (DFB) laser without epitaxial regrowth, by direct etching of the gratings on the top of the ridge and providing a side current injection, has been demonstrated by Liau *et al.* (Liau *et al.*, 1985). Their fabricated devices with 470 μm-long cavity showed a threshold current (I_{thr}) as low as 16 mA at room temperature and side mode suppression ratio (SMSR) values up to 32 dB. In 1991, Miller *et al.* proposed DFB laser with lateral high-order gratings patterned with electron-beam (EB) lithography along the ridge on either side of the contact stripe, as shown in Fig.2. 4 (Miller *et al.*, 1991). For a third-order gratings device with a 735 μm-long cavity, an I_{thr} of 54 mA has been measured in the pulsed mode at room temperature. Although the results were not so promising in terms of single-mode oscillation (due to the presence of Fabry-Perot oscillating modes), the feasibility of laterally-coupled DFB lasers with third and fifth-order gratings has been ascertained.

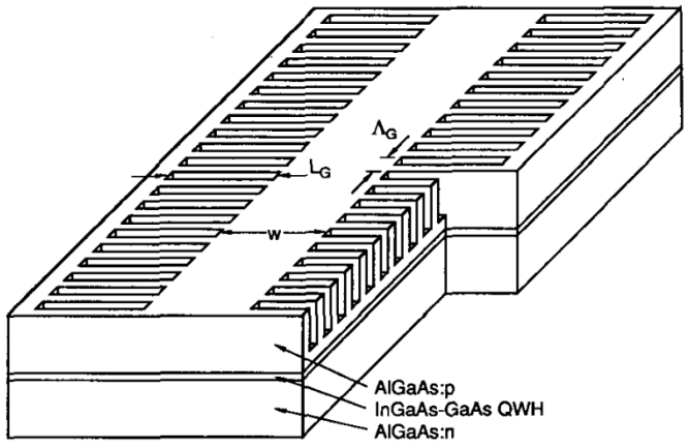

Fig.2. 4. Schematic diagram for the DFB laser with lateral high-order gratings as proposed by Miller et al. (Miller *et al.*, 1991)

Two years later, Wong *et al.* described a distributed feedback structure in which first-order gratings have been patterned onto the sidewalls of a ridge waveguide using x-ray (XR) lithography (Wong *et al.*, 1993). Despite the relevant description of the fabrication steps no testing results have been ever revealed by

this group. Martin *et al.* reported on InGaAs-GaAs-AlGaAs CRW-DFB laser, as shown in Fig.2. 5, using EB lithography and chemically-assisted ion beam etching (CAIBE) (Martin et al., 1994). For an as-cleaved 1.5 mm-long device, an I_{thr} of 15.2 mA and a maximum output power (P_{out}) of ~ 36 mW have been obtained under pulsed conditions at room temperature. Their measurements on 1 mm-long anti-reflected (AR)-coated devices revealed good results with an I_{thr} of 25 mA under continuous-wave (CW) operation, a SMSR of 30 dB at a wavelength of 937 nm, a P_{out} of 11 mW, and an extracted coupling coefficient of 5.8 cm^{-1} (Martin et al., 1995).

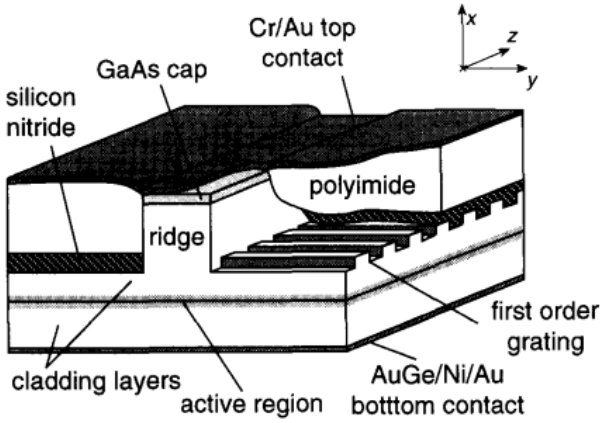

Fig.2. 5. Schematic diagram for the DFB laser with first-order shallow gratings as proposed by Martin *et al.* (Martin *et al.*, 1995)

A similar structure to (Wong *et al.*, 1993) has been fabricated and characterized by Watanabe *et al.* (Watanabe *et al.*, 1998). Their GaInAsP-InP MQW CRW-DFB lasers contain third-order gratings that were fabricated, on and beside the sidewalls of the ridge waveguide, using EB lithography and a wet-dry hybrid etching process. The wet etching step has been added to remove any damaged layer formed by the dry etching. Various as-cleaved devices with different cavity lengths (320, 460, and 600 μm) have been tested under the CW operation. Typical $I_{thr} \leq 24$ mA at 20 °C has been reported for all devices. In particular, the 460 μm-long device showed CW lasing oscillation around 1572 nm, an I_{thr} of 18.5 mA, a SMSR of ≥ 40dB, a P_{out} of 15 mW, and an extracted coupling coefficient of 70 cm^{-1} (Watanabe *et al.*, 1998).

Following the design guidelines for this work, they succeeded in demonstrating 1300 nm CRW-DFB lasers whose 3D structure is shown in Fig.2. 6, in which first-order gratings have been fabricated on and beside the ridge waveguide sidewalls using EB lithography (Chen *et al.*, 2000). The device characteristics revealed a room temperature threshold of 17 mA and SMSR of 45 dB for a 380 µm-long device.

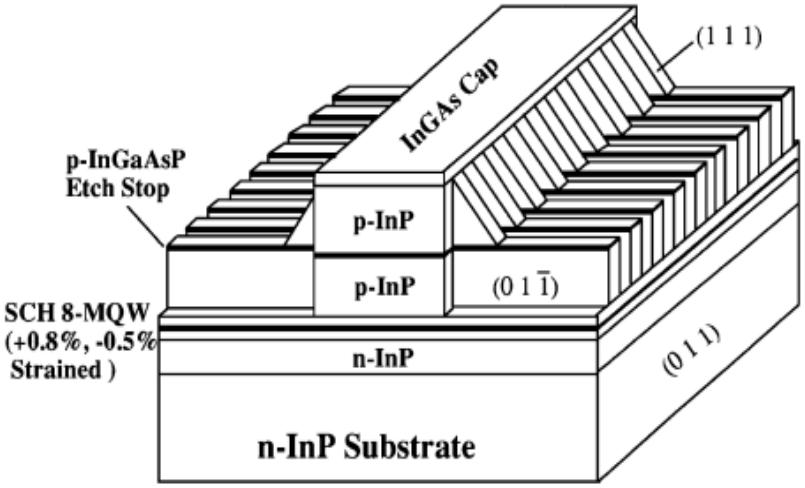

Fig.2. 6. Schematic diagram for the CRW-DFB lasers developed by Chen *et al.* using first-order gratings etched on and beside the ridge waveguide sidewalls (Chen *et al.*, 2000).

CRW-DFB lasers that use metallic rather than etched semiconductor gratings have also been investigated. Indeed, Kamp *et al.* proposed an InGaAs-GaAs-AlGaAs graded-index separate-confinement heterostructure (GRINSCH) CRW-DFB laser that uses laterally-positioned chromium (Cr) gratings, as depicted in Fig.2. 7 (Kamp *et al.*, 1998). First-order gratings were defined by EB lithography. The Cr was then evaporated on each side of the ridge waveguide before applying a lift-off process to define the lateral gratings. An 800 µm-long device exhibited a CW I_{thr} of 12 mA, and a P_{out} of up to 32 mW (A maximum P_{out} of 64 mW has been achieved under pulsed excitation), and a SMSR of 45 dB at 975 nm. The same device but with a smaller cavity length (600 µm) showed an I_{thr} of 9 mA (Kamp *et al.*, 1999).

Later on, Müller *et al.* reported on the use of Cr binary superimposed (BS) gratings in InGaAsP QWs two-section CRW-DFB lasers (Muller *et al.*, 2001). This has allowed a tuning range over 25 nm, an I_{thr} of 32 mA, a P_{out} of 10 mW, as well as an SMSR > 30 dB around 1580 nm for 600 µm-long devices. Yet, the consideration of InGaAs-GaAs quantum-dot (QD) in an 800 µm-long device with Cr BS gratings showed better performances: tuning range of 30 nm, an I_{thr} of 13 mA, a P_{out} of 30 mW, and an SMSR up to 40 dB around 960 nm (Muller *et al.*, 2002).

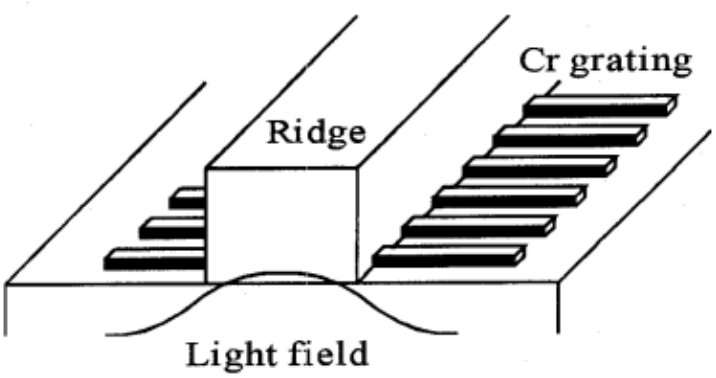

Fig.2. 7. Schematic of the DFB laser using metal (Cr) gratings patterned laterally to the ridge waveguide as proposed by Kamp's group (Kamp *et al.*, 1998).

König *et al.* proposed a complex coupled GaInAsP/InP DFB laser fabricated by using focused ion beam (FIB) lithography (Konig *et al.*, 1999). Once the ridge waveguide was defined, lateral first-order gratings were written by focusing a 100 keVGa+ ion beam. After the implantation an ultrasonic bath was applied to etch the disordered implantation area with high contrast. Smooth refractive index gratings were thus obtained with high aspect ratio and etch depths (Konig *et al.*, 1999). Typical as-cleaved 700 µm-long devices showed a SMSR ≥ 40 dB around 1550 nm, an I_{thr} of 80 mA, and a maximum P_{out} of 4.7 mW at room temperature under CW operation. A linewidth ≤ 2 MHz was obtained with the self-homodyne technique with a Lorentzian fitting.

Reid *et al.* of Bookham Technology successfully attempted to realize an InGaAsP CRW-DFB laser with third-order gratings (Reid *et al.*, 2003). Their

device structure closely replicates the current work undertaken at the Photonic Technology Laboratory since Bookham closed its research operation in Ottawa. In contrast with most of the previous designs, which have been fabricated with EB lithography, the gratings in this design were patterned with stepper photolithography (SL) and etched by induction-coupled plasma (ICP) on the ridge sidewalls. As for the achieved results, a threshold current of ~ 80 mA, an SMSR ≥ 55 dB, a linewidth ≤1 MHz, and optical output power over 100 mW were reported for coated 1.5 mm-long devices. No information about the coupling coefficient has been disclosed; however, the authors claimed that the gratings are stronger than expected. This led to trap more light in the cavity, which favours the onset of spatial hole burning as the power increases. This would explain the kinks observed in their light-current characteristic (Reid *et al.*, 2003). As a consequence, a more reliable design optimization is needed.

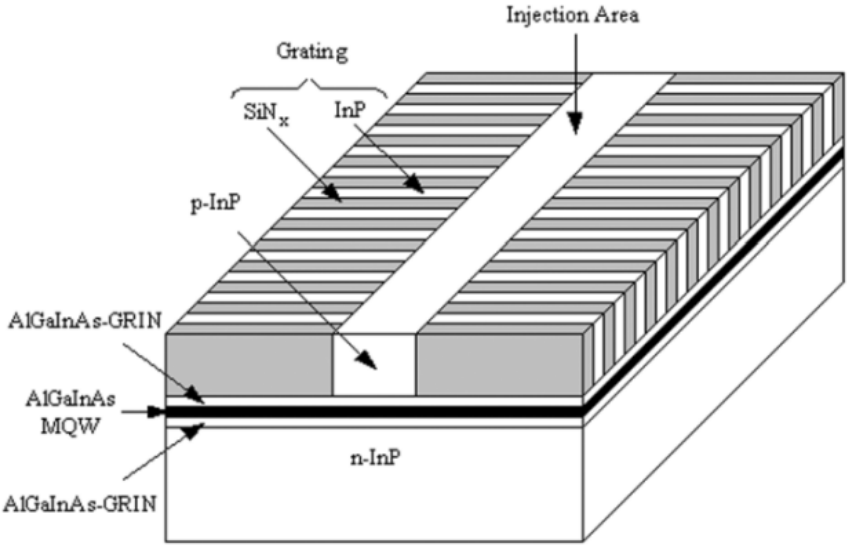

Fig.2. 8. Schematic structure of the LC-DFB lasers with deep etched gratings as proposed by Wang *et al.* (Wang *et al.*, 2005).

Das *et al.* disclosed an InGaAs/AlGaAs strained quantum well (SQW) GRINSCH λ/4 phase-shifted CRW-DFB laser fabricated by EB lithography with a conventional reactive ion etching (RIE) (Das *et al.*, 2004). Fabricated devices with 500 µm-long cavity achieved an I_{thr} of 15 mA, and a maximum P_{out} of 19 mA under CW operation at room temperature. Single mode oscillation with a SMSR

of 46 dB at 967.8 nm was observed, although the laser has been designed to oscillate at 975 nm. Wang *et al.* demonstrated a 1550 nm AlGaInAs-InP CRW-DFB laser whose schematic structure is shown in Fig.2. 8. It used second-order 1.7 µm-deep-etched gratings patterned using optical holographic exposure (HE) and etched by inductively coupled plasma (ICP) dry etching technique (Wang *et al.*, 2005). Stable single mode was observed with an SMSR over 45 dB, an I_{thr} of about 34 mA, and a Pout of 4 mW at 70 mA at room temperature and CW operation for 470 µm-long devices.

Golka *et al.* presented a mid-infrared (MIR) quantum cascade (QC) CRW-DFB laser emitting at 10.7 µm (Golka *et al.*, 2005). The laser has a GaAs/GaAlAs active region and a corrugated ridge waveguide with first-order gratings fabricated by contact UV lithography with an ICP-RIE process. For as-cleaved 950 µm-long devices, an I_{thr} of 590 mA, a maximum P_{out} of 90 mW, and a SMSR of 20 dB were measured under pulsed mode operation (repetition rate of 4.9 kHz) and at a low temperature of ~ -195 °C. The extracted coupling coefficient from measured emission spectra was approximately 29 cm^{-1}.

Kaiser *et al.* reported on InAs/InP quantum dashes (QDash) CRW-DFB laser comprising lateral gratings fabricated by focused ion beam (FIB) implantation and selective wet chemical etching (Kaiser *et al.*, 2005-a). Successful single-mode operation around 1510 nm was recorded with a SMSR of 44 dB, an I_{thr} of 62 mA and a maximum P_{out} of 30 mW at 15 °C for 1 mm-long devices. Small signal modulation response measurements were carried out as well showing a modulation bandwidth of up to 7.6 GHz. In addition, by using the Dash in Well principle, the emission wavelength was shifted to 1900 nm based on laterally coupled gratings (Kaiser *et al.*, 2005-b).

To emphasize on the great advantage that the lateral gratings offer in terms of design flexibility, Reid *et al.* (Reid *et al.*, 2003) proposed devices with different gratings on both ridge sidewalls without showing any results. Pozzi *et al.* demonstrated that dual-wavelength oscillation can be observed in CRW-DFB lasers based on gratings that have different periods on either side of the ridge,

as shown in Fig.2. 9 (Pozzi *et al.*, 2006). In fact, by ensuring a gratings period difference of 0.07 nm, an optical spectrum with two peaks at 1346.32 and 1346.47 nm was recorded. After the photomixing of these optical modes on a fast photodetector, a beat signal at 22.5 GHz was detected.

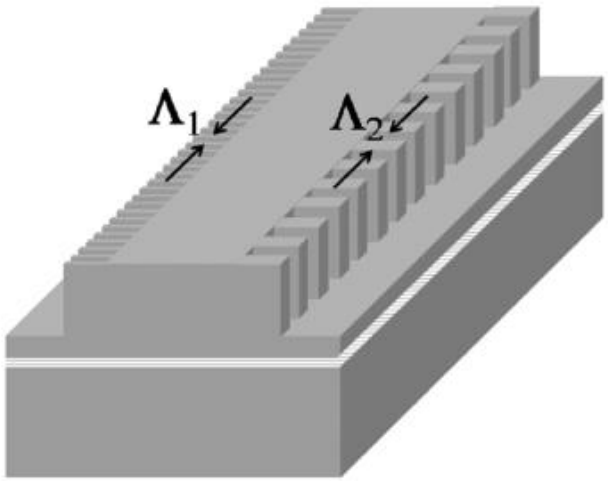

Fig.2. 9. Schematic of the proposed corrugated ridge waveguide with two different gratings by Pozzi *et al.* (Pozzi *et al.*, 2006)

Tolstikhin *et al.* demonstrated an AlGaInAs 1310 nm CRW-DFB laser with fifth-order gratings fabricated by stepper optical lithography (SL) (Tolstikhin *et al.*, 2009). A fabricated 800 µm-long device showed an I_{thr} of 40 mA and an SMSR of ~ 55 dB around 1312 nm at room temperature. The laser has been developed as key part of a transmitter, as shown in Fig.2. 10, for photonic integrated circuits (PICs) applications.

Laakso *et al.* disclosed a CRW-DFB laser with third-order gratings fabricated using UV-based nano-imprint lithography (UV-NIL) (Laakso *et al.*, 2009). Their 570 µm-long laser showed single mode oscillation at 975 nm with an SMSR as high as 50 dB, an I_{thr} of 30 mA, and a maximum P_{out} of 10 mW at 10 °C. Using the same fabrication technique, Haring *et al.* succeeded in fabricating an InGaSb/GaSb CRW-DFB laser emitting at ~ 1945 nm (Haring *et al.*, 2010). The fabricated 1000 µm-long GaSb-based devices exhibited an SMSR over 30 dB, a maximum P_{out} of 2 mW, and an I_{thr} of 90 mA at room temperature. Continuing with the NIL process, Telkkala *et al.* disclosed an InP-based CRW-DFB laser

operating at 1550 nm (Telkkala *et al.*, 2011). A narrow linewidth (~200 kHz), an SMSR of up to 50 dB, a P_{out} of 6 mW, and an I_{thr} of 34 mA were measured for as-cleaved 300 µm-long devices at 20 °C. In addition, a substantial modulation bandwidth increase (>20 GHz) was experimentally proved by exploiting the photon-photon resonance from a 1600 µm-long CRW-DFB laser (Dumitrescu *et al.*, 2011).

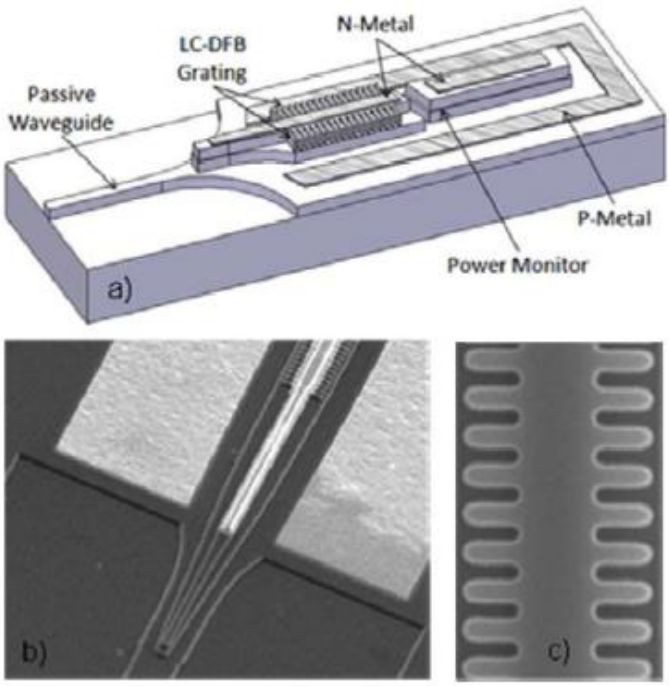

Fig.2. 10. (a) Schematic of transmitter block as proposed by Tolstikhin *et al.*, (b) CRW-DFB laser top view, and (c) top view of the gratings (Tolstikhin *et al.*, 2009)

Yeo *et al.* disclosed a 1300 nm laterally tapered ridge waveguide (RWG) InGaAsP QW DFB laser with second-order metal (Cr) surface gratings, as shown in Fig.2. 11, fabricated by holographic lithography (HL) (Yeo *et al.*, 2010). Three types of devices with 600 µm-long cavity were investigated: conventional, single-tapered, and double-tapered ridge waveguide CRW-DFB lasers. Under CW operation at 20 °C, the conventional laser showed an I_{thr} of 20 mA and a P_{out} of 8.5 mW. For the lasers with tapered ridges, a slight increase in I_{thr} and a decrease in P_{out} have been noticed in comparison with the conventional case.

According to the authors the tapered sections may increase the scattering losses, which then have an impact on the threshold current. On the other hand, the consideration of tapered RWG, particularly the double tapered one, allowed an improvement in the single-mode operation stability: an SMSR of 42 dB at 1334.3 nm and dλ/dT~ 0.071 nm/K were found (Yeo *et al.*, 2010).

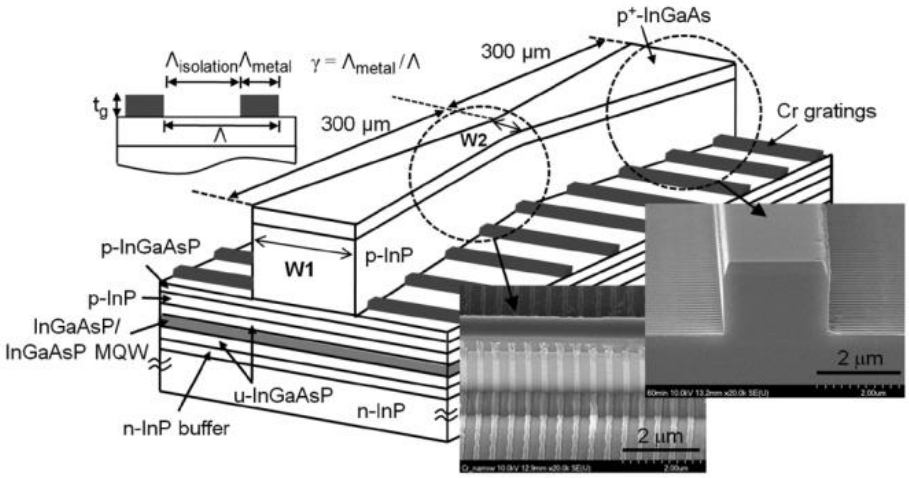

Fig.2. 11. Schematic diagram of laterally tapered ridge waveguide DFB lasers with second-order Cr surface gratings as proposed by Yeo et al. (Yeo *et al.*, 2010).

Forouhar *et al.* reported on GaSb-based CRW-DFB laser operating near 2950 nm (Forouhar *et al.*, 2012). The InGaAsSb/AlInGaAsSb QW laser has a corrugated ridge waveguide with second-order gratings that were fabricated using EB lithography with an inductively coupled plasma reactive-ion etching along a 2 mm-long cavity. An I_{thr} of 34 mA, an SMSR>25 dB, and a P_{out}> 40 mW were measured at 10 °C under CW operation (>80 mW CW output power can be reached at -10 °C). The relatively high power can be due to the use of etched gratings, rather than metal gratings which result in additional losses (Salhi *et al.*, 2006). The fabricated CRW-DFB laser showed a linewidth below 1 MHz over 10 ms-observation times (Briggs *et al.*, 2012). Recently, Briggs *et al.* extended the previous approach to wavelength near 2650 nm for atmospheric gas detection applications (Briggs *et al.*, 2013). These lasers emitted more than 25 mW and exhibited a threshold of 150 mA at 20 °C.

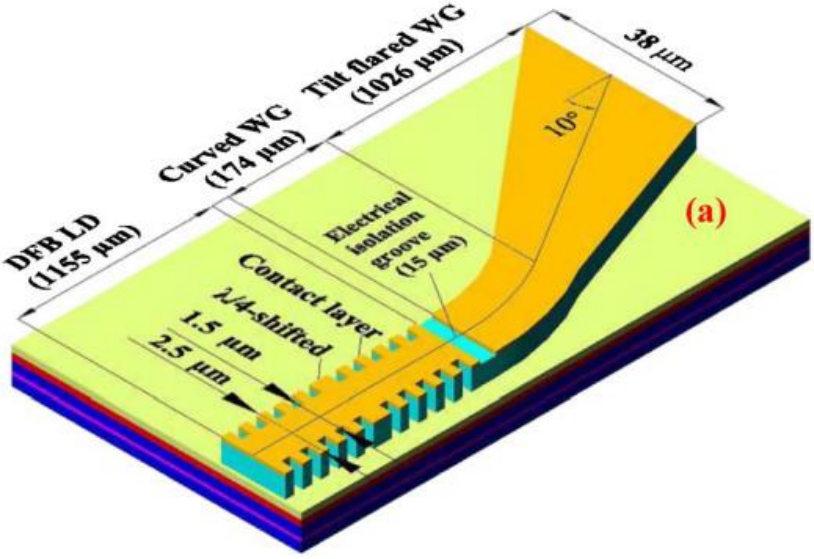

Fig.2. 12. Schematic of the device, including the DFB laser plus the SOA, as proposed by Hou *et al.* (Hou *et al.*, 2012)

Hou *et al.* presented a 1550 nm AlGaInAs/InP CRW-DFB laser monolithically integrated with a curved tapered semiconductor optical amplifier (SOA), as shown in Fig.2. 12 (Hou *et al.*, 2012). The laser extends over 1155 μm-long cavity housing a λ/4-phase-shift section in the middle and first-order gratings fabricated with EB lithography along with RIE dry etching. At 20 °C and under CW conditions, the laser exhibited a 50 mA threshold current, an SMSR > 45 dB, and a narrow linewidth of 64 kHz at 300 mA. The combination with the SOA allowed an output power of up to 210 mW. Using the subthreshold spectra-fitting method, the measured coupling coefficient was approximately 24 cm^{-1}. Besides, Hou et al. have demonstrated also the integration of four AlGaInAs/InP CRW-DFB lasers with a monolithically integrated 4×1 multimode-interference (MMI) optical combiner, an SOA, and an electro-absorption modulator (EAM), as shown in Fig.2. 13. Using this monolithic integration, they successfully demonstrated a coarse wavelength division multiplexing (CWMD) source with 12 nm channel spacing in the 1550 nm range (Hou *et al.*, 2011).

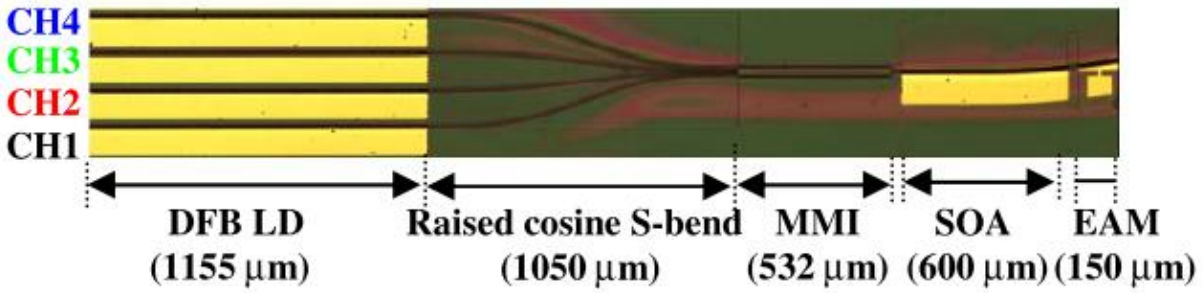

Fig.2. 13. The CWDM source based on four monolithically integrated AlGaInAs/InP CRW-DFB lasers as proposed by Hou *et al.* (Hou *et al.*, 2011)

Most recently, Zanola *et al.* presented an interesting example where the CRW-DFB lasers can be used with other photonic components for particular applications. Indeed, they proposed a semiconductor monolithic optoelectronic device designed and fabricated for the generation of narrow linewidth millimeter-wave signals that can be continuously and widely tunable (Zanola *et al.*, 2013). As shown in Fig.2. 14, the AlGaInAs/InP DFB lasers used lateral gratings with a wide width ridge of 2.4 µm, a lateral recess of 0.3 µm (or narrow ridge with of 2.1 µm), and a cavity length of 400 µm. The gratings were patterned by EB lithography and defined by RIE process. To ensure a single-mode operation a λ/4-phase-jump was placed in the middle of the cavity. Each of the three lasers showed single-mode operation around 1550 nm with a SMSR of 60 dB, an I_{thr} of 25 mA, and a maximum P_{out} of 10 mW. A continuous tuning of 3.5 nm has been achieved by tuning the biasing current from I_{thr} up to 150 mA (*i.e.* a wavelength tuning of ~ 24 pm/mA). The optical linewidth for each DFB laser has been determined using a coherent heterodyne technique where a Lorentzian fitting showed a linewidth of 13 MHz. For more details about the device principle, which is based on the photomixing assisted by mutual injection locking via four-wave mixing (FWM), the reader can consult (Zanola *et al.*, 2013; Soldo *et al.*, 2009). We just wanted to emphasize on the potential useful applications of these lasers.

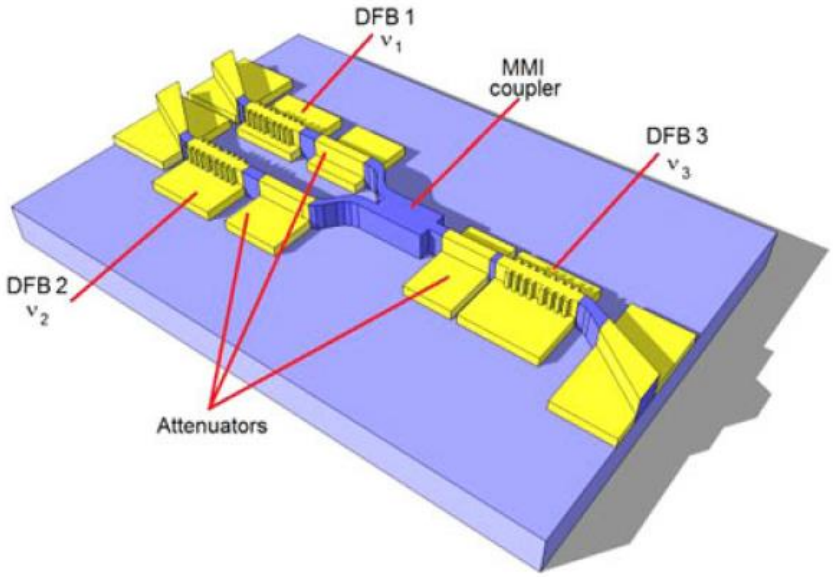

Fig.2. 14. Schematic diagram of the proposed semiconductor monolithic photonic device for the generation of mm-wave signals by Zanola *et al.* (Zanola *et al.*, 2013)

Table2. 1 summarizes the performance of a large number of CRW-DFB lasers that have been developed so far. It is clear that the CRW-DFB lasers have been implemented on different gain medium material using different gratings designs to target wide range of wavelength windows. Also it is clear that the EB lithography has been the technique of choice for many laser designs. Most of the fabricated CRW-DFB lasers showed SMSR values ≥ 30 dB, which is important in WDM systems to avoid any inter-channel interference. As for the other device performance, we see that the threshold currents were varying from 9 to ≥ 90 mA. For the coupling coefficient there were a few publications that revealed the experimental extracted values. The extraction was based on the subthreshold spectra-fitting method, which will be applied for our laser designs. The linewidth determination was also revealed for a few designs. We also see that the CRW-DFB lasers have been fabricated for different applications going from telecom to gas detection applications.

Table2. 1 Performance of the most known CRW-DFB lasers (HL: Holographic lithography; RIE: Reactive-ion-etching; ICP: Inductively coupled plasma; FIB: Focused ion beam; SL: Stepper lithography; SOA: Semiconductor optical amplifier)

Device	Gain medium	Gratings (order/type)	Fabrication technique	L (μm)	λ (nm)	SMSR (dB)	I_{thr} (mA)	P_{out} (mW)	κ (cm^{-1})	Δν (MHz)
Miller *et al.*	InGaAs-GaAs-AlGaAs /QWH	3rd – 5th / etch	EBL & RIE	735	~ 1050	n/a	54	~ 40	n/a	n/a
Martin*et al.*	InGaAs-GaAs-AlGaAs/GRINSCH	1st / etch	EBL & CAIBE	250	921.7	30	11	15	n/a	n/a
				1000	935		25	11		
				1500	937.2		15.2	36	5.8 / extr	
Watanabe *et al.*	GaInAsP-InP MQW	3rd / etch	EBL & wet-dry etch	420	1572	40	18.5	15	70 / extr	n/a
Kamp *et al.*	InGaAs/AlGaAs /GRINSCH	1st / metal (Cr)	EBL	600	975	45	9	31	10 / calc	n/a
Müller *et al.*	InGaAs-GaAs QD /GRINSCH	BSG / metal (Cr)	EBL	800	960	40	13	30	n/a	n/a
Reid *et al.*	InGaAsP-InP / MQW	3rd / etch	SL & ICP	1500	~ 1480	55	80	100	n/a	≤ 1
Das *et al.*	InGaAS/AlGaAs SQW-GRINSCH	2nd / etch (λ/4-phase-shift)	EBL & RIE	500	967.8	46	15	19	n/a	n/a
Wang *et al.*	AlGaInAs-InP	2nd / etch	HL & RIE & ICP	470	1545	45	34	4 /70 mA	18.3 / calc	n/a
Kaiser *et al.*	AlInGaAs/InAs/InP Q-Dash	1st / etch	FIB implantation	1000	1513	44	62 /15 °C	30 /15 °C	10 / calc	n/a
Tolstikhin *et al.*	AlGaInAs-InP SCH MQW	5th / etch	SL	800	1312	55	40	11 /20 °C	30 / calc	n/a
Laakso*et al.*	GaInAs MQW	3rd / etch	NIL	570	975	50	30 /10 °C	10 /10 °C	25 / calc	n/a
Haring *et al.*	InGaS MQW	3rd / etch	NIL	1000	1945	30	90	3	n/a	n/a
Yeo*et al.*	InGaAsP-InP MQW	2nd / metal (Cr)	HL	600	1334	42	20-25	8.5	5-17 / calc	n/a
Telkkälä *et al.*	InP-based	3rd / etch	NIL	300	1555	50	34	6	n/a	~ 0.2
Forouhar *et al.*	InGaAsSb/AlInGaAsSb MQW	2nd / etch	EBL & ICP-RIE	2000	2050	20	34 /10 °C	80 /-10 °C	3-4 / calc	≤ 1
Hou *et al.*	AlGaInAs/InP	1st / etch (λ/4-phase-shift + SOA)	EBL & RIE	1155	1550	45	50	210	24 / extr	0.064

Furthermore, as can be seen previously, various CRW structures have been proposed and mostly fabricated with electron-beam (E-beam) lithography. This technique enables easier first-order gratings writing thanks to its greater resolution. In addition, with E-beam lithography, complex structures such as CRW with chirped gratings or CRW with phase shift sections can easily be made (Carroll *et al.*, 1998). Nevertheless, this technique is slow and expensive if compared to standard optical lithography techniques (Reid *et al.*, 2003). In contrast, stepper lithography is a well suited technique for mass-production (Reid *et al.*, 2003). In stepper lithography, patterns are optically projected in a rapid step and repeat fashion across a wafer. An image or feature on a mask, called also a reticle, is reduced by a certain factor when it is projected onto the wafer. The stepper machine available at the Canadian Photonics Fabrication Facility (CPFC) uses a demagnification factor of 5×. The machine has an I-line lenses which are exposed to a mercury lamp line at 365 nm. An historical outline of stepper systems has been highlighted by Fay of Nikon Research Corporation of America (Fay, 2002). Given that the available stepper machine at CPFC is limited to resolutions of 365 nm, the first- and second-order Bragg gratings are not reachable for 1310 nm lasers; however, the third- order gratings are just possible. This constraint dictated the choice of high-order (≥3) gratings, where the larger gratings periods allow for more stringent manufacturing tolerances. Yet, the consideration of high-order gratings that induce radiating partial waves requires a full two-dimensional (2D) model. This has been done by extending the modified coupled mode theory (Streifer *et al.*, 1976) to 2D cross section, where gratings' geometries that are both fabrication-tolerant and having high performance are thereby identified (Millet *et al.*, 2008a-b).

An automated and precise experimental setup has been built allowing an accurate assessment for the fabricated device performance (Dridi *et al.*, 2010). As will be described subsequently, different CRW-DFB lasers have been developed targeting different wavelength windows (1310, 1550, 1560 nm).

Typical 1310 nm lasers showed stable single-mode operation with a SMSR ≥ 50 dB, I_{thr} ≥ 60 mA, Pout ≥ 10 mW, and an extracted coupling coefficient of ~12 cm^{-1} at 25°C, as will be described in Chapter 3, section 1. Besides, CRW-DFB lasers at 1550 nm showed stable single mode operation with a SMSR≥ 54 dB, I_{thr}≤ 65 mA, Pout ≥ 7 mW, wavelength tunability of ~ 2 nm, an extracted coupling coefficient of ~10 cm^{-1}, and linewidth ≤250 kHz at 25°C, as will be described in Chapter 3, section 2. In addition, devices with CRW having uniform gratings have been fabricated with multi-electrode contact for the first time. We recorded SMSR ≥ 54 dB, wavelength tunability ≥ 3 nm, and linewidths ≤ 140 kHz at 25°C, as will be shown in Chapter 4.

Chapter 3|

Standard corrugated ridge waveguide DFB lasers at 1310/1550 nm

In this chapter we start by presenting the experimental results for corrugated ridge waveguide DFB (CRW-DFB) lasers that have been designed at 1310 nm in the first section. The results demonstrated the successful application of the modified coupled mode theory for this structure (Millet *et al.*, 2008a). This model has been upgraded to design 1550 nm laser source based on the CRW concept. In the second section we present the results of these devices.

3.1. Corrugated ridge waveguide DFB lasers at 1310 nm

Summary

An earlier work aimed at developing 1310 nm corrugated ridge waveguide DFB (CRW-DFB) laser sources under the project "Optical Coherent Transmission for Access Network Extensions (OCTANE)". The goal was to develop a CRW-DFB laser as a local oscillator to be integrated in optical coherent receivers targeted to fiber-optic access network applications. In the fabrication of these sources, stepper lithography with limited resolution of ~ 0.3 μm has been used at the Canadian Photonics Fabrication Facility (CPFC). InGaAsP devices at 1310 nm have been successfully fabricated using high-order gratings. Their design and experimental results are presented in this chapter. A series of experimental results, including light-current, voltage-current, temperature sensitivity, optical spectrum, and coupling coefficient allow for device assessment.

Contribution

The experimental results in this chapter were published in the journal of Photonics and Nanostructures – Fundamentals and Applications. I have done

almost all the experimental characterization, processed data, generated, interpreted the results, and wrote the entire manuscript. Dr. Millet did the design and modelling and the extraction of the coupling for this work. I have been working with him to provide the experimental results for his PhD thesis. Mr A. Benhsaien helped in the writing and in the verification of the coupling extraction. Drs Schriemer, Hinzer, and Hall were supervising this work and contributed to the revision of the manuscript. I have also presented other results and described the experimental setups in another publication (Dridi *et al.*, 2010).

Article

The published paper follows. I have reproduced[1] the paper in the same format as the main thesis text.

Citation

R. Millett, K. Dridi, A. Benhsaien, H. Schriemer, K. Hinzer, and T. Hall, "Fabrication-tolerant 1310 nm laterally coupled distributed feedback lasers with high side mode suppression ratios," Photonics and Nanostructures – Fundamentals and Applications, vol. 9, no. 2, pp. 111-118, Apr. 2011.

[1] This includes the formatting (without content changes) of: the text, figures captions, and reference citations. I deleted the references section from the paper, given that they all appear in the bibliography section of the thesis. The abbreviation of LC-DFB in the following paper has the same meaning as CRW-DFB.

Fabrication-tolerant 1310 nm laterally-coupled distributed feedback lasers with high side mode suppression ratios

R. Millett[1], K. Dridi[1], A. Benhsaien[1], H. Schriemer[1], K. Hinzer[1] and T. Hall[1*]

Centre for Research in Photonics, University of Ottawa, 800 King Edward Ave., Ottawa, ON, K1N 6N5, Canada
* thall@site.uottawa.ca, 1-613-562-5800 ext. 2121,
http://www.photonics.uottawa.ca/index.shtml

Abstract. 1310 nm laterally-coupled distributed feedback (LC-DFB) laser was designed and fabricated using stepper lithography. Such DFB lasers eliminate the need of the commonly required regrowth steps in a conventional DFB laser fabrication process. With LC-DFB lasers, the gratings can be lithographically patterned out of the ridge waveguide. Gratings with higher order can enhance the lithographic tolerance for lower resolution patterning, yielding lasers more amenable to mass-manufacturing. 1310 nm InGaAsP/InP LC-DFB laser with third-order gratings has been fabricated using I-line 5× stepper lithography. Excellent side mode suppression ratio over 53 dB has been measured with a single mode lasing around 1310 nm.

Keywords: distributed feedback lasers, third-order gratings, side mode suppression ratio, and stepper lithography.

3.1.1. Introduction

Unlike standard Fabry-Perot (FP) lasers, distributed feedback (DFB) lasers - thanks to their wavelength-selective grating- feature an improved spectral purity, wavelength stability and temperature sensitivity. Moreover, DFB lasers offer an enhanced longitudinal mode selectivity that can be specified by the side mode suppression ratio (SMSR) separating the lasing peak and its adjacent highest spectral peak. DFB lasers find applications in different areas including spectroscopy and optical communication systems. They are increasingly

integrated in DWDM applications due to their low linewidth and good stability. DFB lasers are typically manufactured with a gratings' layer near the active region. The growth of DFB structures starts with the lower epitaxial layers, then patterning the gratings, and finally the upper epitaxial layers. Such a sequential growth process thus involves the use of re-growth techniques. In contrast, laterally-coupled DFBs (LC-DFB), such as our structure shown in Fig.3. 1, eliminate the redundant requirement of two separate epitaxial growth steps by directly pattering the gratings along the sidewalls of the waveguide ridge. Therefore, LC-DFB lasers can increase the manufacturing throughput and shorten the fabrication time.

Since LC-DFB lasers require deep, smooth, and finely-etched gratings, the electron-beam (e-beam) lithography has so far been the manufacturing method of choice (Martin *et al.*, 1995; Muller *et al.*, 2002). Although e-beam lithography is a direct-write technique, it is often costly and slow for mass-manufacturing. Stepper lithography, despite its stringent fine-etching requirements, is capable of simultaneous patterning of many gratings. In particular, stepper lithography becomes amenable to high-yield and low-cost manufacturing with high order gratings (Millet *et al.*, 2008a-b-c).

First-order gratings have been extensively studied (Whiteaway *et al.*, 1989; Li *et al.*, 1998); however, comparatively little work has been done for higher-order gratings. Most existing treatments of high-order gratings generally assumed one-dimensional slab waveguides in either transverse direction (Streifer *et al.*, 1976; Shams-Zahdeh-Amiri *et al.*, 2000). Such treatments are also inadequate for the case of LC-DFB lasers with higher order gratings because the properties of the laser strongly depend on the two-dimensional cross-section.

In our previous work, we have extended the modified coupled-mode theory, which has been demonstrated by Streifer *et al.* (Streifer *et al.*, 1976; Streifer *et al.*, 1977), to a two-dimensional cross-section (Millet *et al.*, 2008b). Gratings' geometries that are both highly performing and fabrication-tolerant are thereby identified (Millet *et al.*, 2008b). We have also demonstrated by comprehensive

two-dimensional analysis that such high-order gratings can provide improved longitudinal mode discrimination, minimizing radiation loss through grating parameter optimization (Millet *et al.*, 2008a).

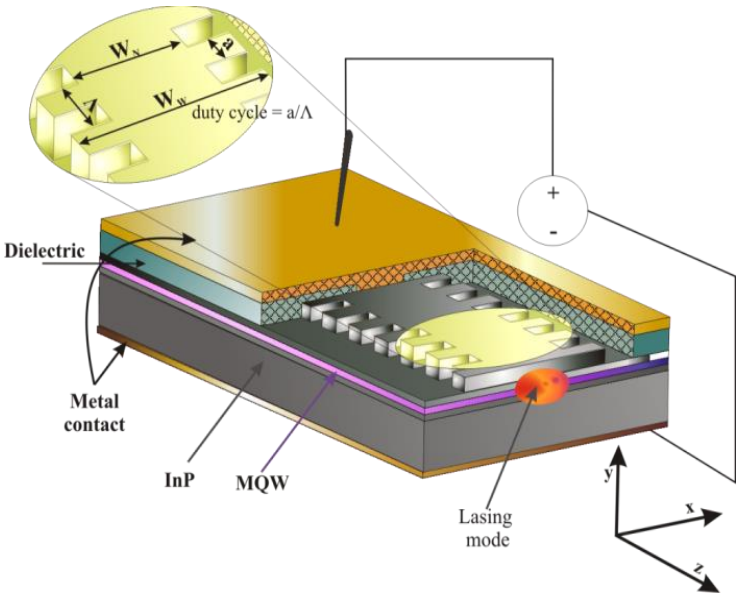

Fig.3. 1. Cutaway schematic for the laterally-coupled distributed feedback (LC-DFB) laser.

In this paper, 1310 nm InGaAsP/InP LC-DFB laser fabricated using stepper lithography is presented. Our laser, designed with third-order gratings, has particularly higher SMSR than a range of commercially available 1310 nm DFB lasers.

3.1.2. LC-DFB Device Fabrication

Laterally-coupled DFB structure

The LC-DFB laser active region consists of a five-fold vertical stack of 0.9% compressively strained 6-nm-thick quantum-wells embedded in 0.1% tensile strained 10-nm-thick barriers. Fig.3. 2 gives the chosen epitaxial growth structure.

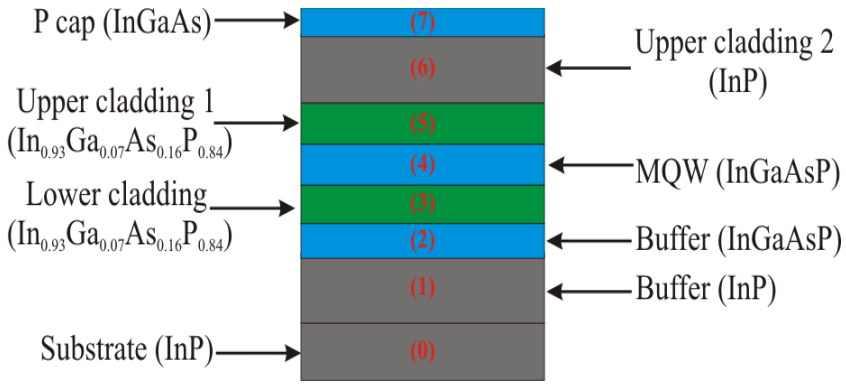

Fig.3. 2. Epitaxial structure used to fabricate the LC-DFB laser

Mask design

The LC-DFB laser mask was designed with six layers: two dry-etching layers, an evaporated metal layer, a dielectric via layer, an InGaAs removal layer, and an electroplated metal layer. The two-dry etching layers is composed of one layer for the detailed etching around the ridge and one layer for the coarser etching of the trench around the ridge. Different designs variations were included in the mask: the narrow and wide ridge widths have variations between 1.5 and 2.5 µm and 2.5 and 5 µm, respectively. There were gratings' order variations, which determine the period – 600 nm for the third-order and 800 nm for the fourth-order. There are also Fabry-Perot laser test structures on the mask. The layout of these design variations on the mask was created using the dw-2000 software from Design Workshop Technologies based on 'p-cells" technology.

Device Fabrication

The fabrication process of our design, which was funded by the Canadian Microelectronics Corporation (CMC), has been performed at the Canadian Photonic Fabrication Centre (CPFC) in Ottawa, ON. The fabrication of the gratings used the i-line 5× stepper lithography technique. They were etched by an inductively-coupled reactive ion etch (RIE) process (for the fine gratings' features) and a wet chemical etch (for coarser features such as the trench surrounding the gratings).

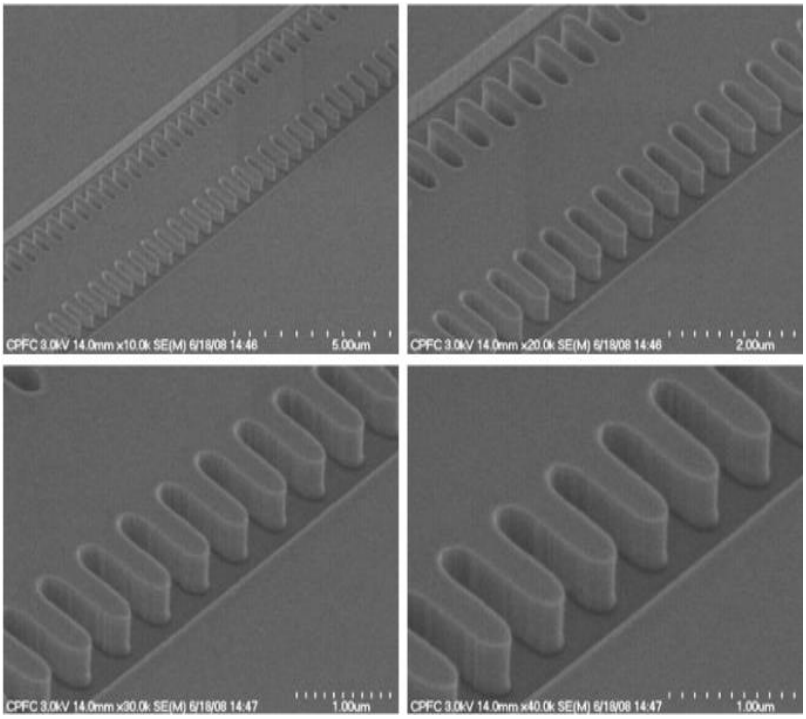

Fig.3. 3. Tilted view of gratings at various magnifications

Some scanning electron microscope (SEM) photos of the gratings were taken at CPFC along the fabrication of the lasers. Fig.3. 3 shows smooth, vertical, and well-defined gratings: the gratings periods are consistent over the appeared length scale without any missing or poorly-defined grating teeth. Moreover, the aspect ratio remains steady along the gratings' length. Therefore, a stable and consistent manufacturing process can be inferred while observing these photos. However, the gratings are not perfectly squared as they were expected. The fabricated gratings revealed that the grating teeth are rounded as shown in Fig.3. 3. This changing in the grating shape shall need another analysis, different from the one that has been carried out with rectangular shape (Millet *et al.*, 2008a-b), regarding particularly the influence of this shape on the coupling coefficient. In this analysis we perform some calculations based on exact measurements of the grating geometry taken from the SEM photo.

Due to the resolution of the stepper lithography process, very fine gratings' features didn't always turn out as intended. Such features tended to be washed out during the etching process.

The laser chips were cleaved into device lengths of 500, 750, 1000, 1250, and 1500 μm. The laser bars were all-tested with as-cleaved facets. Figure 3.4 shows the top view of a 500 μm cavity length laser. The metal contacts show no noticeable lift-off. Few of the lasers tested showed any visible evidence of cleave damage from above. A facet inspection is the best way to see the quality of the cleave. This task is in the pipeline.

Fig.3. 4. Top view of fabricated third-order LC-DFB with cavity length of 500 μm

3.1.3. Measurements and analysis

To characterize our LC-DFB we performed four basic measurements: current-voltage (IV), optical output power vs. bias current (LI), optical spectrum and side-mode suppression ratio (SMSR).

IV Characteristic

The current-voltage (IV) characteristic provides an indication of the quality of the p-i-n junction and metal contacts. It can help reveal how efficiently carriers are injected into the structure. An example of a laser IV curve for 1500 μm cavity length device, with ridge widths W_N/W_W = 1.5/4 μm, is shown in Fig.3. 5. A typical operating range region for this laser is from 100 to 200 mA. A LC-DFB with a low dynamic resistance will have less heating and more overall carriers injected into the active region. Therefore, a lower threshold and better efficiency are expected.

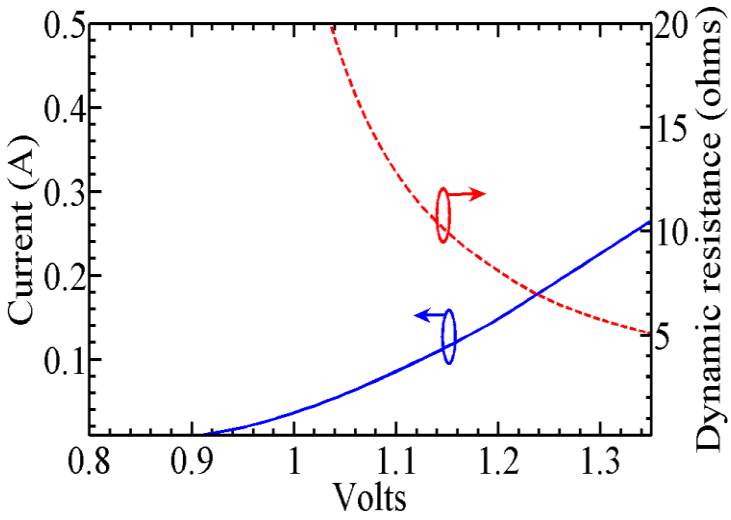

Fig.3. 5. IV characteristic for 1500 μm cavity length device (W_N/W_W = 1.5/4 μm) at 298 K.

L-I Characteristic

The L-I characteristic or the optical output power for a given bias current is a fundamental laser measurement. From a LI graph several fundamental characteristics can be extracted. The threshold current, I_{th}, defines the point after which the carrier injection into the active region is sufficiently high for the optical gain to be greater than the optical losses. The stimulated emission hence begins to dominate the spontaneous emission. After the threshold point the output power initially increases with the bias current. The slope of the linear fit is known as the slope efficiency or the device efficiency. When thermal roll-off begins to occur, the output power reaches a maximum value, P_{max}. Beyond this maximum, the output power decreases until catastrophic failure occurs at very high bias currents. In addition to the main aforementioned three parameters, LI curve provides information on the quantum efficiency η, and the characteristic temperature, T_0. It also offers a good way to approximate the optical loss of the laser. In addition, the external quantum efficiency (η_d) can be obtained from the slope of the LI characteristic $\eta_s=\Delta P/\Delta I$, using (Mobarhan, 1999):

$$\eta_d = \eta_s\left(\frac{q\lambda}{hc}\right) \tag{3.1}$$

where λ is the free-space wavelength (1310 nm in our case), while the other constants are q = 1.6022×10^{-19} C, the fundamental electronic charge, h=6.6263×10^{-34} J.s, the Planck's constant, and c = 2.99×10^{8} m.s^{-1}, the vacuum speed of light. The quantum efficiency of the laser is a measure of how efficiently the laser can convert electrons into photons via stimulated emission. An example of LI-characteristic for 3rd-order gratings 1000 µm long is shown in Fig.3. 6.

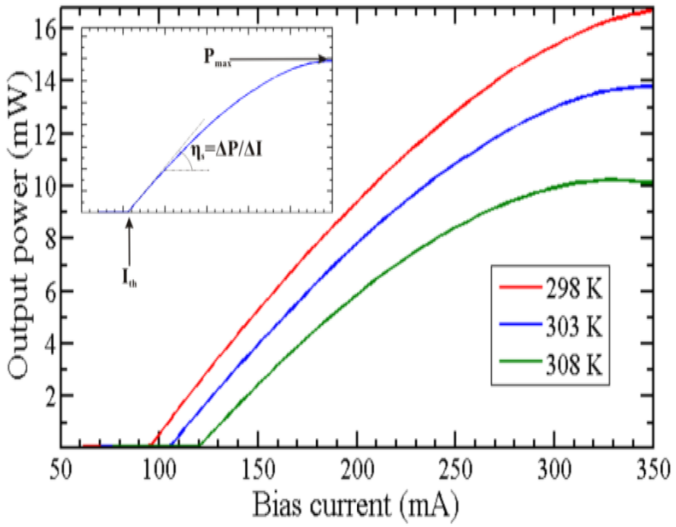

Fig.3. 6. LI-characteristic for 3rd-order gratings 1000 µm-long cavity (Relevant parameters are shown in the top-left inset).

The measured threshold currents, corresponding to the three temperatures 298 K, 303 K, and 308 K, are 94, 103, 118 mA, respectively. The LI curves shown in Fig.3. 6 exhibit three different maximum output powers: 17, 14, and 10 mW. The calculated values for the efficiency slope are 0.099, 0.083, and 0.076 mW/mA, for the three mentioned temperatures, respectively. The typical average threshold current for the tested devices is 95 mA. It's higher than expected from the LAS2D simulations due to additional losses, likely because of the proximity of the optical mode to the metal contacts. The threshold currents of both LC-DFB and Fabry-Perot lasers were compared for the highest yield cavity length of 1000 µm. The distribution of threshold currents for this cavity length is plotted in Fig.3. 7 (a). For purpose of comparison, the average threshold current of 1000

μm cavity length Fabry-Perot lasers is shown in Fig.3. 7 (a) with ridge widths of 1.5 and 4 μm. For wide ridge width FP lasers, the average threshold current is 85 +/- 1mA. This is an encouraging comparison, as a significant number of LC-DFB lasers had a lower threshold current than the average FP laser current.

Fig.3. 7(b) shows a comparison between the slope efficiencies of 1000 μm cavity length FP and LC-DFB lasers. The average efficiency of most of the DFB lasers is 0.096 mw/mA. This efficiency is poor in comparison with that of the narrow ridge FP laser. The additional gratings' loss is the main reason for the somewhat poorer efficiency of these lasers compared to complementary FP designs. However, with only a 20 % poorer average slope efficiency, and 12% higher average threshold current, compared to the wide ridge FP laser, the penalty for the additional gratings' loss is very modest, particularly for the benefit of having a high side-mode suppression ratio.

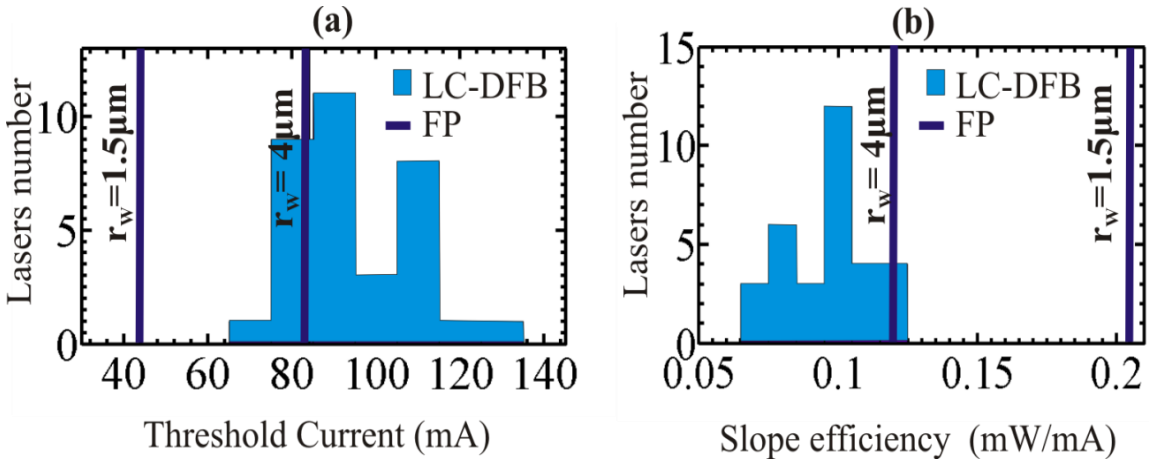

Fig.3. 7. Distribution of (a) threshold currents, and (b) slope efficiencies for 1000 μm-long cavity LC-DFB lasers with 3rd order gratings and FP lasers with ridge width of 1.5 and 4 μm. (r_W: ridge width). The average threshold current of 1000 μm-long cavity FP lasers is shown inside

From the ridge width analysis, the 2 μm narrow ridge width lasers show the lowest threshold currents and highest slope efficiencies. For instance, for the 1000 μm cavity length lasers, the W_N/W_W = 2/4 μm design demonstrated one of the best designs in terms of slope efficiency and threshold current with average slope efficiency of 0.104±0.005 mW/mA and an average threshold current of 86

+/- 3 mA. For this design, a balance between strong gratings and good electrical injection is maintained.

Temperature sensitivity

Characteristic temperatures were measured for a wide range of cavity and ridge width sizes as shown in Table3. 1. The DFB lasers had an average characteristic temperature T_0 of 303.2 K. This value agrees with the FP lasers results, with measured T_0 = 313 K. This indicates that the LC-DFB lasers don't have a significantly greater threshold current sensitivity to temperature compared to FP lasers.

Table3. 1. Characteristic temperatures for some cavity lengths and ridge widths

Cavity length (μm)	750		1000		1250	
W_N/W_W (μm)	1.5/4.5	2.0/4.0	1.5/4.5	2.0/4.5	2.5/4.5	FP
T_0 (K)	303.4	305.1	308.3	309.2	300.2	313

Optical Spectrum and Side-Mode Suppression Ratio (SMSR)

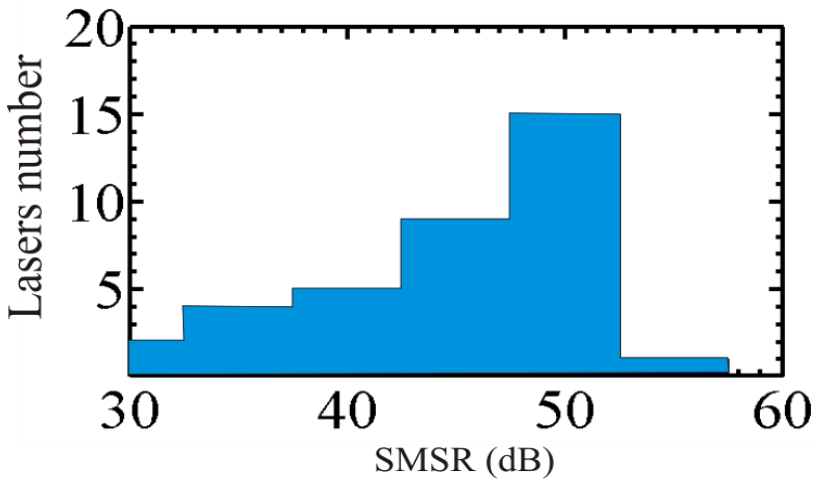

Fig.3. 8. Distribution of side-mode suppression ratio of LC-DFB lasers with third-order gratings.

Our measurements showed excellent SMSR values as depicted in Fig.3. 8. A significant number of LC-DFB lasers have a SMSR greater than 40 dB or even 50 dB without any additional facet coatings to produce an AR/HR laser cavity.

Many operational lasers demonstrated excellent SMSR greater than 50 dB, a value indeed better than many commercially-available DFB lasers. Standard devices (*i.e.* 3rd-order gratings with a narrow ridge width of 1.5 μm and a wide ridge width of 4 μm) particularly showed a SMSR above 50 dB.

The optical spectrum of a 1000 μm long standard device is shown in Fig.3. 9. We measured an SMSR of 52 dB for this device.

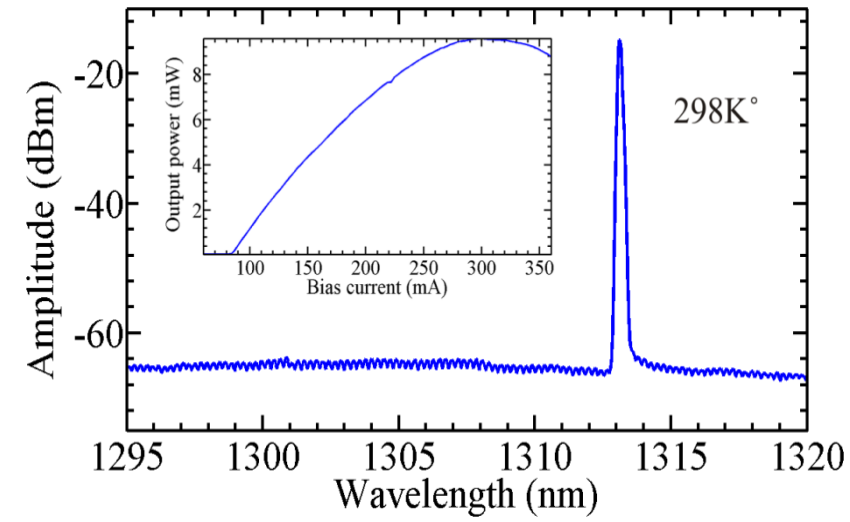

Fig.3. 9. Standard gratings 1000 μm-long LC-DFB at 150 mA injection and 298 K. Inset is the L-I characteristic of this laser with I_{th}=84 mA.

Furthermore, devices with λ/4 phase-shift grating have been also designed and fabricated in the purpose to get better longitudinal mode discrimination. However, due to the rounded gratings and the limitation of the resolution in the fabrication process, the results showed slightly worse performance than the standard devices. In fact, the average threshold current of the standard gratings lasers of 102 +/- 8 mA is lower than that of the phase-shift gratings of 116 +/- 6 mA, while the SMSR of the standard gratings lasers is 47.3 +/- 2.4 dB, higher than average SMSR of the phase-shifted lasers of 40.7 +/- 2.1 dB.

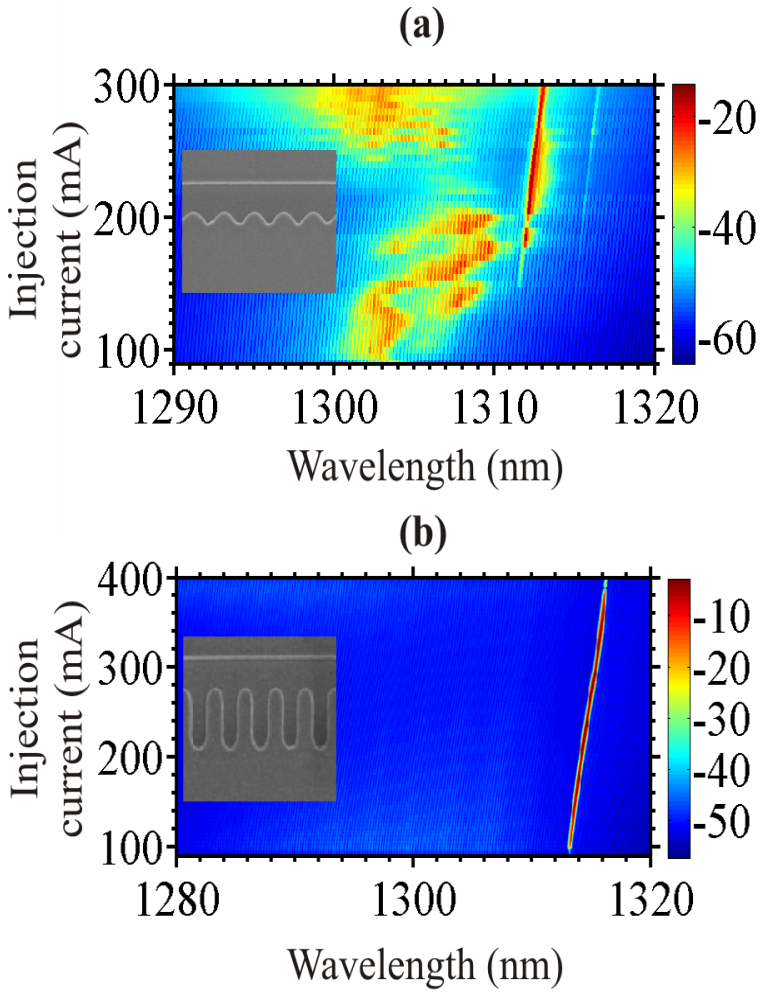

Fig.3.10. 2D optical spectra for a range of injection currents: (a) higher duty cycle (0.6); (b) half-duty cycle (0.5). Inset top view of gratings' teeth for 3rd-order gratings with duty cycles of 0.6 and 0.5, respectively

Another parameter with an important effect on the longitudinal mode discrimination is the duty cycle. Indeed, with gratings designed with duty cycles > 0.5, a conditionally-stable DFB lasing in the range of 200-250 mA is observed with a maximum SMSR of 27 dB. Fig.3.10(a) demonstrates that these lasers are more like FP than DFB lasers. The insert in Fig.3.10(a) shows a top view of gratings' teeth for third-order gratings with a duty cycle of 0.6. The grating is almost completely washed out. At this duty cycle and above, the obtained shallow and sinusoidal shape of the gratings' teeth provides very little coupling. This

would explain why the performance of these devices is expected to be more like an FP laser rather than DFB laser. It can be inferred that a more precise fabrication method than I-line stepper lithography will be required to create the narrow spacing between the gratings' teeth with duty cycles > 0.5. However, for the half duty-cycle devices, a single strong DFB lasing peak with SMSR > 50 dB is observed as shown in Fig.3.10(b).

As for the ridge width, its variations have demonstrated the best single-mode DFB lasing as well as excellent characteristics including the highest SMSR. Over 53 dB has been measured for a 750 μm long device with widths of W_N/W_W = 1.5/4.5 (μm). However, the best yielding design was for W_N/W_W = 1.5/3.5 (μm) for the 1000 μm cavity length lasers. There have been also some poorer yield, particularly for the designs with W_N/W_W = 1.5/2.5 μm, 2.5/4 μm, and 2.5/4.5 μm. As it can be seen in Fig.3. 11(b), the 1.5/2.5 μm gratings are nearly washed out in contrast to the 1.5/4.5 μm gratings shown in Fig.3. 11(a). The fabricated corrugated ridge waveguide resulted in weaker gratings, and therefore, in a lower coupling coefficient and poorer yield. Since this coefficient is already degraded due to rounding of the gratings, the additional widening of the narrow ridge is likely to weaken the gratings too much for achieving a DFB lasing. Although a gradual improvement for the coupling coefficient is predicted, it may be counteracted by increased diffusion of carriers into the teeth of the gratings. These carriers contribute to a larger lateral leakage current, which not only reduces the injection efficiency but also decreases the amount of gain that's possible for lasing operation.

The temperature dependence of the lasers was experimentally determined. The DFB lasing spectrum has been measured for the 1000 μm device with W_N/W_W = 2/3.5 μm at an injection current of 200 mA for a range of temperatures. The red-shift in the lasing peak was only 0.06 nm/K, much less than the 0.65 nm/K measured for the FP lasers. The shift in the DFB lasers is due to the Bragg wavelength shifts that are chiefly due to the refractive index changes with

temperature. These shifts are much less that the shift in material gain wavelength with temperature, as with FP lasers.

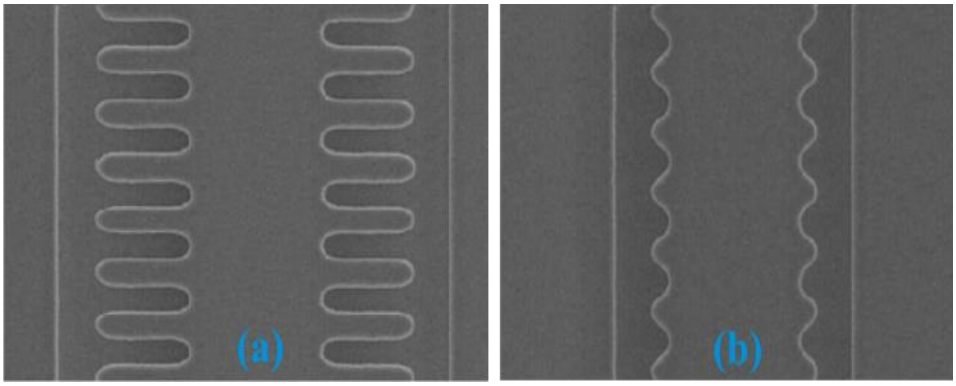

Fig.3. 11. Top view SEM micrographs of third-order gratings with intended W_N/W_W values of (a) 1.5/4.5 µm, and (b) 1.5/2.5 µm.

Experimental coupling coefficient extraction

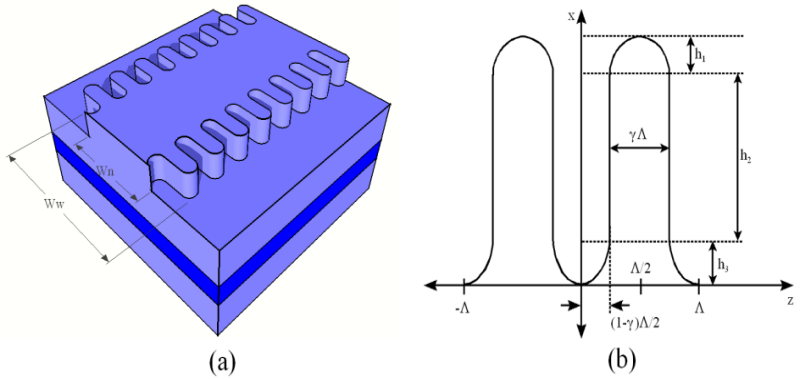

Fig.3. 12. Rounded gratings in (a) perspective view, (b) with detailed teeth of rounded gratings.

The fabricated gratings revealed that the rectangular gratings' shape, assumed in the analysis of (Millet *et al.*, 2008a-b), is rounded during the manufacturing process as shown in Fig.3. 3. Hence, this gratings' shape needs to be accurately modeled with gratings' teeth that are elliptical at the gratings' ends. Assuming this model, the rounded gratings' shape shown in Fig.3. 12 are defined within a gratings' period by four parameters, h_1, h_2, h_3, and the duty cycle, γ.

Using this model, the calculation of the effective coupling coefficient is shown in Fig.3. 13.

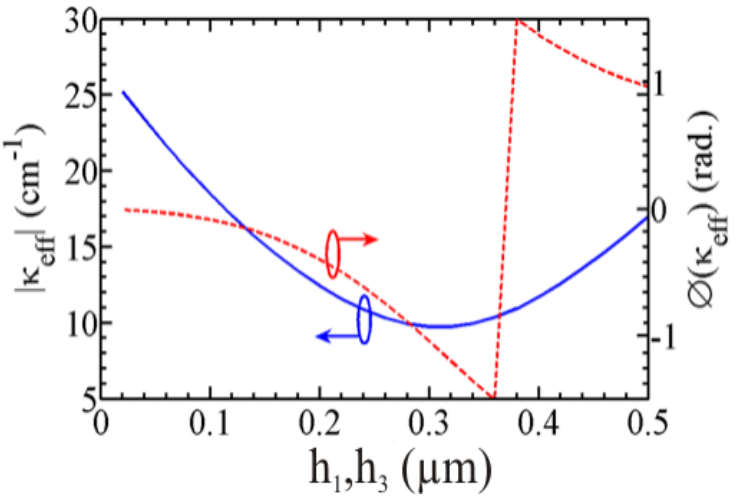

Fig.3. 13. Effective coupling coefficient *vs.* h_1, h_3 for a third-order rounded gratings with W_N/W_W = 1.5/4 μm, where $h_1 = h_3$ and the duty cycle = 0.5.

To accurately assess the gratings' strength, as defined in (Millet *et al.*, 2008a-b), of the manufactured gratings, exact dimensions were taken from the available SEM photos. The measured rounding parameters show an effective coupling coefficient of $\kappa_{eff} = 12.2\angle -0.16$ cm^{-1}. The extraction of the modified coupled-mode coefficients from the experimental data is the most challenging data analysis task. The extraction of these coefficients will provide experimental data for comparison with the two-dimensional simulations outlined in our previous work (Millet *et al.*, 2008a-b). Only the standard gratings have been treated due to the time-consuming nature of this data extraction. The purpose of this task is to show how well the rounded grating coefficients shown in Fig.3. 13 fit the experimental data. The generally accepted method of extracting these coefficients is to use the below-threshold spontaneous emissions spectrum. We have used a variation of this technique using the Green's function method described by Wenzel (Wenzel, 2003), specifically for gain- or loss-coupled lasers with complex coupling coefficients.

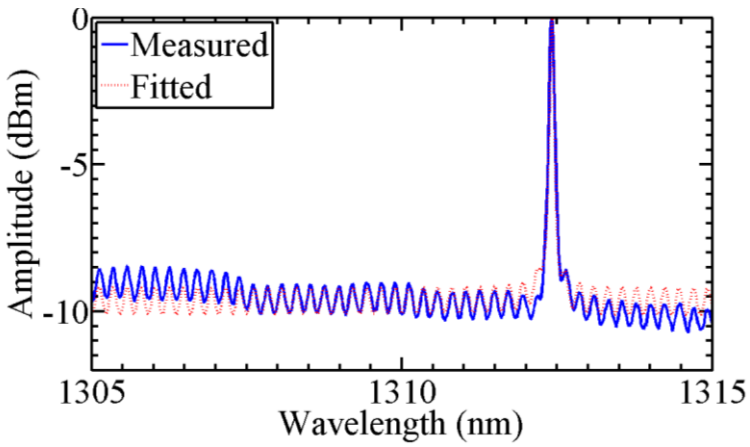

Fig.3. 14. Measured and fitted amplified spontaneous emission spectrum of 1000 μm cavity length laser with W_N/W_W = 1.5/4 (μm) ridge widths at 298 K and an injection current of 70 mA.

The spectrum to be fitted, shown in Fig.3. 14, resulted from a 1000 μm long standard LC-DFB laser with W_N/W_W = 1.5/4 μm. The measured and fitted spectrums agree reasonably well with an average deviation of 7.5 %. The fitted result shows an effective coupling coefficient κ_{eff} =12.5∠1.38 +/- 1.4∠0.05 cm^{-1}. Comparing this value to that calculated of the standard gratings of 12.2∠−0.16 cm^{-1}, we see excellent agreement in the magnitudes, but not in the phase of the coupling coefficient. The difference in the coupling coefficient can be explained by the variations in the rounded gratings' parameters.

For example, a rough first-pass approximation of the parameters that match the measured coupling coefficient are W_N= 1.68 μm, γ=0.48, h_1 = 0.17 μm, h_2=0.54 μm, and h_3 = 0.25 μm. These fitting parameters actually match quite well with the SEM photo of the standard grating taken in Fig.3. 15(a), rather than the standard gratings pictured in Fig.3. 15(b), as the overlay of the SEM photo and the theoretical gratings with the parameters given above in Fig.3. 15(c) demonstrates. The effective coupling coefficient calculated for these rounded gratings is κ_{eff} =12.3∠1.41 cm^{-1}, a difference of 2% from the measured coupling coefficient, well within the tolerance of this measurement. This

measurement of the coupling coefficient validates the theoretical calculations of the coupling coefficient.

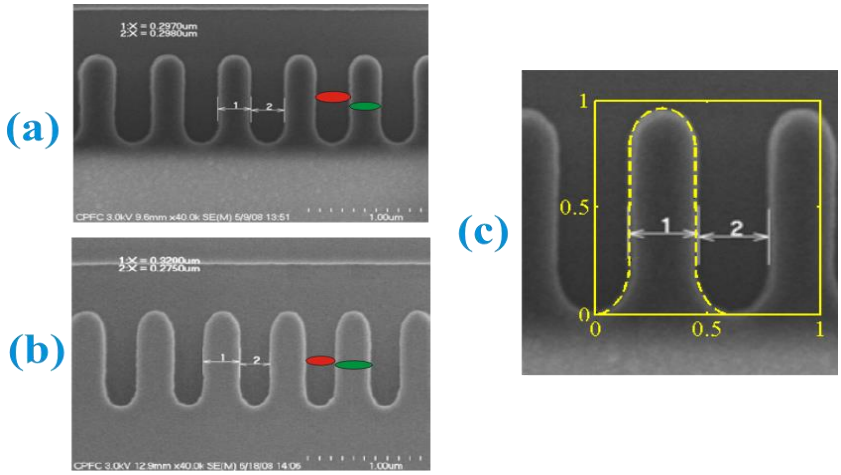

Fig.3. 15. SEM photo of the standard grating (a) the wrong model (b) the right model to choose (c) Comparison of standard third-order gratings SEM photo and rounded gratings, outlined in yellow, with h_1=0.17 µm, h_2 = 0.54 µm, h_3=0.25 µm, and γ=0.48 (Scale on axes is in microns).

3.1.4. Conclusions

We presented the fabricated and the characteristics of the third-order 1310 nm InGaAsP/InP LC-DFB laser. This laser was fabricated by simple process using stepper lithography and a conventional inductively-coupled plasma etching. Our LC-DFB laser demonstrates high SMSR values > 50 dB, better than a range of commercially available 1310 nm DFB lasers. The threshold currents are comparable to FP lasers, suggesting minimal penalty for higher order gratings. Moreover, the fabricated laser shows a small shift in wavelength with temperature of about 0.05 nm/K. This makes these lasers ideal for stable operation over a range of operating temperatures. Finally we demonstrated that the experimentally extracted coupling coefficient agrees well with calculated value for the rounded grating.

Acknowledgements

We gratefully acknowledge support from the Natural Sciences and Engineering Research Council (NSERC), the Canadian Foundation for Innovation (CFI),

CMC Microsystems, Canadian Photonics Fabrication Centre (CPFC), Ontario Centre of Excellence (OCE), OneChip Photonics, Canada Research Chairs Program, Ontario Graduate Scholarship Program, and the Communications Research Centre Canada (CRC).

3.2. Corrugated ridge waveguide DFB lasers at 1550 nm

Summary

Major revisions on both the epitaxial engineering and the numerical model have been carried out leading to the migration towards 1550 nm MQW CRW-DFB lasers. This has been done under the strategic project grant namely "Narrow line-width surface corrugated quantum well and quantum dot distributed feedback lasers". This is considered as an extension of work that has been done with 1310 nm. In this section, we demonstrated an InGaAsP/InP CRW-DFB laser at 1550 nm. The main differences in comparison to the previous 1310 nm CRW-DFB laser design are: the addition of an etch stop layer, a doubly of the ridge height, and changes to material composition and thickness to accommodate the new wavelength. Sidewall etched third-order gratings have been defined using the same I-line optical lithography at CPFC. In this work a new setup has been built using new CFI items. This allows for undertaking careful experimental work to characterize the performance, particularly the linewidth, of the fabricated lasers

Contribution

The results described in this section have been published in IEEE Photonics Technology Letters. I designed and built the experimental setups. I generated and interpreted the experimental results, and wrote the manuscript. I have also assisted with Mr. Benhsaien in the epitaxial structure design, CRW numerical modelling, and in the mask layout. Dr. Zhang contributed to the design verification and validation at CMC before sending the devices for fabrication. Dr. Hall contributed to the design of the experimental setup, interpretation of the results, and revision of the paper.

Article

The published paper follows. I have reproduced[2] the paper in the same format as the main thesis text.

Supplement

General guidelines and tips regarding some results in this paper such as the extraction of the modal gain and the linewidth measurement and determination are given in appendix A and appendix B, respectively.

Citation

K. Dridi, A. Benhsaien, J. Zhang, and T. J. Hall, "Narrow Linewidth 1550 nm Corrugated Ridge Waveguide DFB Lasers," IEEE Photonics Technology Letters, vol. 26, no. 12, pp. 1192-1195, Jun. 2014.

[2] This includes the formatting (without content changes) of: the text, figures captions, and reference citations. I deleted the references section from the paper, given that they all appear in the bibliography section of the thesis.

Narrow Linewidth 1550 nm Corrugated Ridge Waveguide DFB Lasers

Kais Dridi, Abdessamad Benhsaien, Jessica Zhang, and Trevor J. Hall, *Member, IEEE*

Abstract—We report on the design and characterization of InP-based multiple quantum well corrugated ridge waveguide distributed feedback diode lasers operating at 1550 nm. Third-order gratings have been etched along the sidewalls of the ridge waveguide using the standard I-line stepper lithography technique with an inductively-coupled reactive ion etching process. An as-cleaved 1500 μm-long laser diode shows stable continuous wave single-mode operation at 1550 nm with high side-mode suppression ratios (>50dB), a temperature-dependent wavelength shift $d\lambda/dT \sim 0.095$ nm/°C, and output powers ≥ 7mW at 25°C. Linewidth determination has been carried using the delayed self-heterodyne interferometric technique. Narrow linewidths (≤ 250 kHz) have been observed for a wide range of current injection, with a minimum of 184 kHz at 300 mA.

Index Terms—Distributed feedback (DFB) lasers, delayed self-heterodyne interferometry, InP/InGaAsP multiple quantum well (MQW), Lorentzian lineshape, stepper lithography, Voigt profile.

3.2.1 Introduction

The fast growth and deep penetration of optical fibers into access networks calls for inexpensive, low power consumption and reliable optoelectronic devices. Recently, there has been a considerable amount of interest in developing photonic integrated circuits (PICs) for advanced coherent fiber-optic communications. The development of low cost (PICs) is ultimately driven by the development of low cost photonic components amenable to integration. The development of distributed feedback (DFB) lasers that use surface rather than

buried gratings brings compatibility with low-cost production, high performance, and ease integrability. Indeed, surface-gratings DFB or laterally coupled DFB (LC-DFB) lasers (Miller *et al.*, 1991; Wong *et al.*, 1993; Konig et al., 1999; Reid *et al.*, 2003; Telkkala *et al.*, 2011) make use of gratings that are patterned and etched along the sidewalls of the ridge waveguide (*i.e.* a corrugated ridge waveguide (CRW)), as shown in our design in Fig.3. 16. This is in contrast with the conventional DFB laser, where the gratings are etched near the active region before being buried with the upper epitaxial material. This involves a process interruption which may affect the performance of the fabricated device by inducing some perturbations to the interface between the gratings and the upper cladding and cap layers. With the LC-DFB technology, we seek a great simplification in the fabrication process, while keeping high performance levels. Furthermore, the use of lithographic techniques such as stepper lithography will open the doors for low-cost mass-production of laser sources, which will be well suited to low cost PICs.

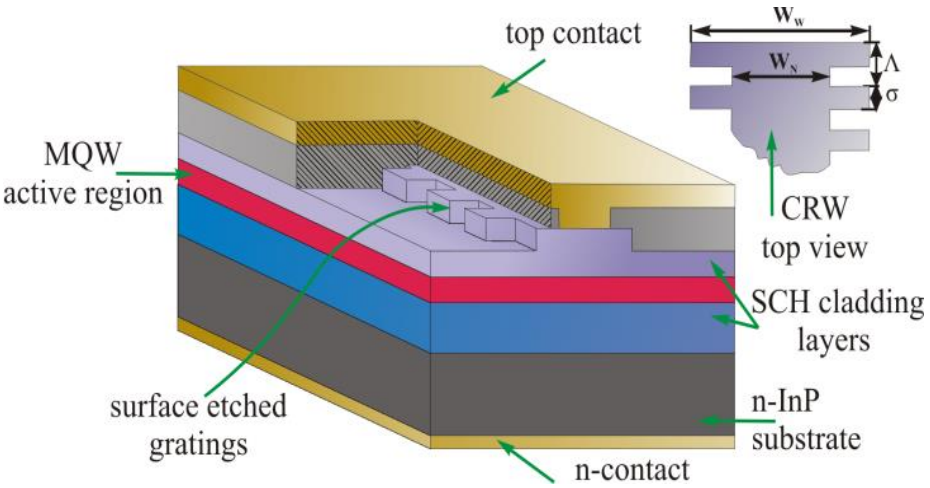

Fig.3. 16. Schematic of our designed corrugated ridge waveguide (CRW) DFB laser. In the top-right corner a top view cut-away of the CRW is given, where W_W: wide ridge width, W_N: narrow ridge width, Λ: gratings' period, and σ: the gratings' mark. (MQW: multiple quantum well; SCH: separate confinement heterostructure).

We have designed our laser structure as revealed in Fig.3. 16. The corrugated ridge waveguide has been modeled and designed with third-order gratings using the modified coupled mode (MCM) theory (Millet *et al.*, 2008a). The MCM theory,

demonstrated earlier by Streifer et *al.* (Streifer *et al.*, 1976; Streifer *et al.*, 1977), has been extended to a waveguide with two-dimensional cross-section to account for the strong dependency of the properties of high-order gratings on the transversal geometry of the device (Millet *et al.*, 2008a). It has been demonstrated also that such higher-order gratings can provide improved longitudinal mode discrimination, minimizing radiation loss through gratings' parameter optimization (Millet *et al.*, 2008b). Based on this theory, we successfully demonstrated a single mode 1310 nm LC-DFB laser (Millet *et al.*, 2011). The model has been then upgraded to accommodate the 1550 nm wavelength. The modeled devices have been fabricated at the Canadian Photonics Fabrication Centre. In this letter, we report on the experimental characterization of devices that incorporate third-order gratings, which have been written by stepper lithography and etched by inductively-coupled reactive ion etch (RIE) process enhanced with a wet chemical etch process. In particular, we demonstrate single mode and narrow linewidth InGaAsP multiple quantum well (MQW) CRW-DFB lasers at 1550 nm. Although such DFB-based structures have been fabricated using different techniques (Miller *et al.*, 1991; Wong *et al.*, 1993; Konig *et al.*, 1999; Reid *et al.*, 2003; Telkkala *et al.*, 2011), only a few publications have reported the linewidth of these lasers. Reid et *al.* (Reid *et al.*, 2003) claimed a linewidth < 1 MHz and Telkkälä et *al.* (Telkkala *et al.*, 2011) reported a linewidth of 203 kHz at a particular current. However no experimental study has shown the variations of the linewidth for wide injection current ranges.

3.2.2. Device Structure and Fabrication

The laser heterostructure was grown on an n-type InP wafer using the metal-organic chemical vapour deposition (MOCVD) technique. It consisted of two 200-nm-thick separate confinement heterostructure (SCH) cladding layers which enclose a six-fold vertically-stacked InGaAsP quantum well (MQW) layers. Each 5-nm-thick $In_{0.68}Ga_{0.32}As_{0.89}P_{0.11}$ quantum well was slightly compressively-

strained and alternately spaced by an 8-nm thick $InGaAs_{0.447}P_{0.553}$ potential barrier which was lattice-matched to the InP substrate. A 5 nm-thick etch-stop layer yielded a 0.8 μm ridge height, which is equal to the gratings' etch depth. A heavily p-doped 50-nm thick InGaAs contact layer formed an ohmic contact. The CRW was defined by 5× I-line stepper machine for photolithography allowing the transfer of the patterns to a SiO_2 hard mask layer. Third-order lateral gratings were then formed along the ridge sidewalls using an inductively-coupled reactive ion etching (RIE) process plus a wet chemical etch. The CRW-DFB laser mask has been designed to be compatible with a stepper lithography process, where a single stepper tile was repeatedly exposed across the wafer. The size of the tile used was 6 mm × 6 mm. After the etching process, the wafer was passivated with an insulating dielectric (SiO_2) layer, followed by via etching into the areas where electrical injection is provided. Finally, Ohmic contacts (n- and p-contacts) were formed above and below the device, respectively.

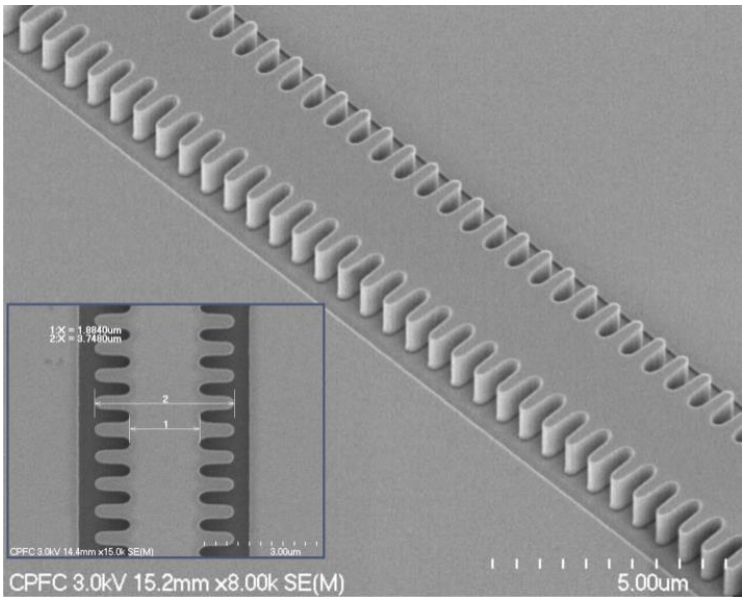

Fig.3. 17. Scanning electron micrograph showing a tilted view of the fabricated ridge waveguide with third-order gratings (a top view of the actual fabricated CRW is given in the bottom left corner)

Fig.3. 17 shows a scanning electron micrograph (SEM) of the fabricated third-order gratings. The latter look very smooth, albeit with some rounding, which is

due to the stepper machine limitations. Indeed, the available machine offers a resolution around 365 nm, which is just within the gratings' space (*i.e.* (1-γ)Λ, where γ=σ/Λ is the duty cycle). Despite this rounding a stable DFB mode oscillation has been observed as will be seen the next section. We believe that the results obtained augur well for the exploration of other lower fabrication resolutions.

3.2.3. Device Characterizations

The fabricated device features a 1500-µm-long cavity which houses a CRW with third-order gratings. The CRW has been fabricated with 0.8 µm deep gratings with a pitch of 0.7078 µm and a duty cycle of 55 %. The narrow and wide ridge widths are ~ 1.5 and 4 µm respectively. The bare laser diode chips have been mounted on a temperature-controlled stage.

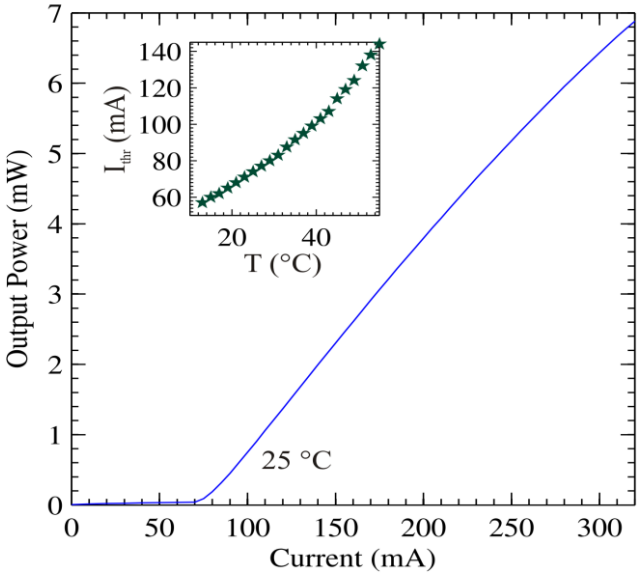

Fig.3. 18. Typical output light vs. current at 25°C for 1500 µm-long device. The inset shows the variation of the threshold current (I_{thr}) for the same device against the temperature.

Typical kink-free light-current characteristic for an uncoated 1500 µm-long laser is shown in Fig.3. 18. Under continuous wave (CW) operation at 25°C, the laser exhibited a threshold current (I_{thr}) of ~ 74 mA, a maximum slope efficiency (η) of 0.031, and an output power greater than 7 mW for injection levels greater than $4\times I_{th}$. We consider that the measured output power is a positive feature for

this laser keeping in mind that high-order gratings (3rd-order in our case) induce radiation losses, which are estimated as 19 cm^{-1}. The low slope efficiency η, which has been found to be comparable to counterpart Fabry Perot devices (η=0.053) fabricated in the same wafer, could be explained in part by the low internal quantum efficiency of 48.73 % and the external quantum efficiency of 17.9 %. Besides, from the FP device characterization, we estimate internal loss of ~ 11.6 cm^{-1} and mirror loss of 19.4 cm^{-1} suggesting a total loss of ~ 31 cm^{-1}. In addition, the effective coupling coefficient κ, extracted from sub-threshold spectra is estimated as 10 cm^{-1}, yielding κL of ~ 1.5. The inset in Fig.3. 18 shows the variations of the measured I_{thr} as a function of the temperature. This threshold is found to be higher than anticipated. We believe that some non-negligible quantity of carriers diffuse into the gratings teeth leading to a leakage current, which is spread laterally on the sides of this ridge waveguide laser (Miller *et al.*, 1991). In addition, other reasons behind this observation may find their roots in the engineering of the epitaxial structure (hence the material gain), which has been optimized using an equivalent Fabry-Perot (FP) cavity to the actual CRW-DFB structure using the LAS2D software (Las2D, 2006). This approach omits however the particularities of the gain gratings, coupled to the refractive index gratings, from the actual material gain calculations. In fact, the extraction of the gain from actual fabricated devices allows us to confirm this software capability limitation. That is, the extraction of the modal optical gain from some FP devices included in the same wafer as the CRW-DFB devices, has shown a spectral shift of about ~ 40 nm between the gain peak (λ_{gp} ~ 1590 nm) and the resonance wavelength (λ_{res} = 1550 nm) at 25°C, as can clearly be seen in Fig.3. 19. The inset of this figure shows the variations of the detuning (λ_{gp} - λ_{res}) against the temperature. This observation suggests an adjustment of the gain profile is required to minimize the observed detuning.

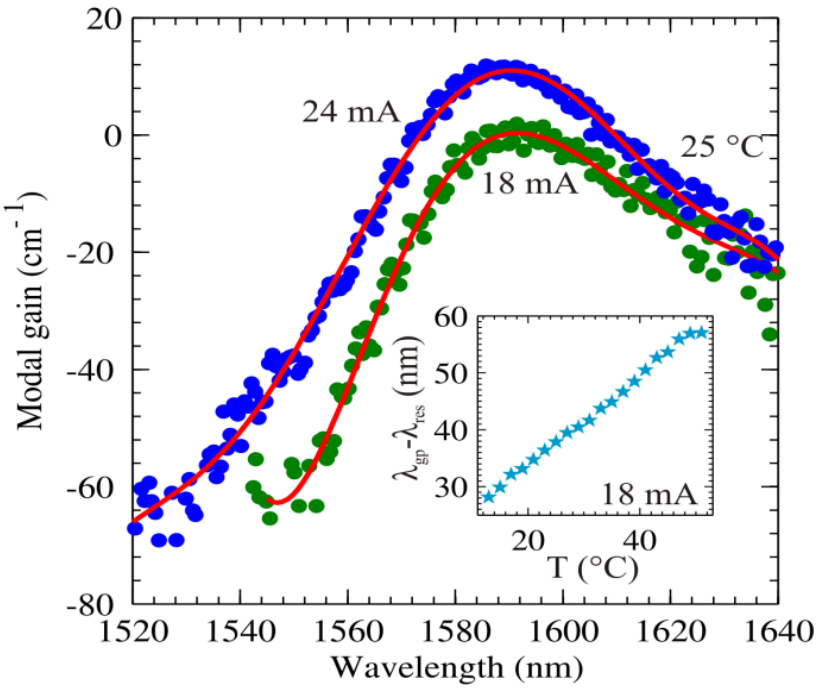

Fig.3. 19. Optical modal gain at 25°C *vs.* wavelength for 500 µm-long FP device (at different currents below threshold). The inset shows the variations of the detuning (λ_{gp} - λ_{res}) against the temperature at I = 18 mA.

The optical spectra characterization revealed a stable single mode operation for wide range of injection currents and at different temperatures. Fig.3. 20 shows the variations of the measured side mode suppression rations (SMSRs) against the lasing wavelength at 25°C. SMSRs ≥ 50 dB have been obtained at bias current of 250 mA for temperatures ≤ 41°C, as shown by the top-right inset in Fig.3. 20. Fig.3. 21 shows the current- and temperature-dependent peak wavelength variations. This device can achieve a wavelength tuning greater than 2 nm with a tuning coefficient dλ/dI of ~ 0.009 nm/mA at 25°C. It can also achieve a dλ/dT of ~ 0.095 nm/°C while driving it at ~3.4×I_{thr}, as can be seen in the top inset of Fig.3. 21.

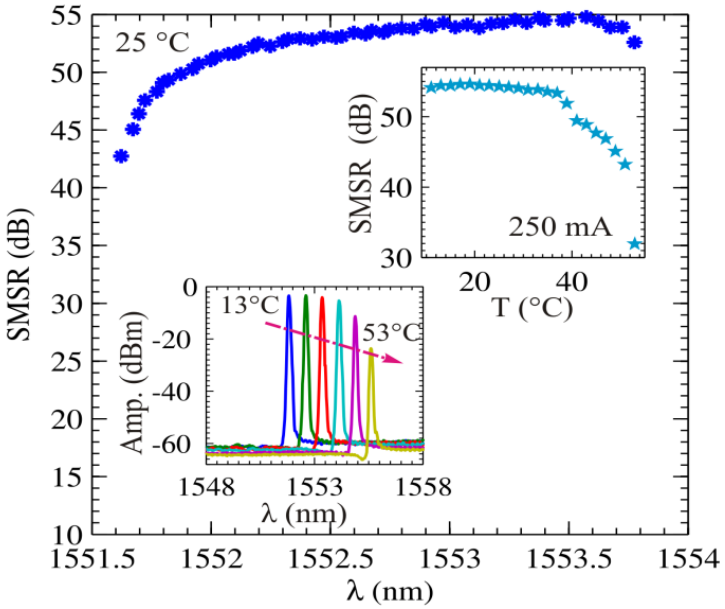

Fig.3. 20. SMSR variations against the lasing wavelength at 25°C for 1500 µm-long CRW-DFB laser. The right inset shows the variations of the SMSR as a function of the sink temperature. The left inset shows the emission optical spectra measured at 250 mA at different temperatures.

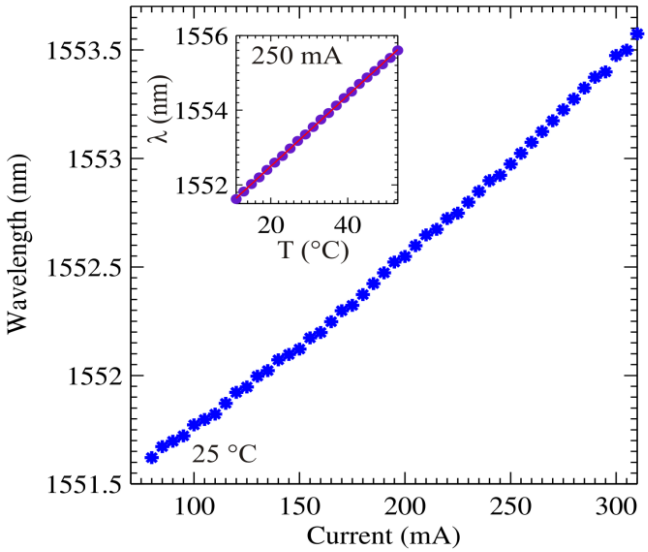

Fig.3. 21. Wavelength variations as function of the injection current for 1500 µm-long CRW-DFB laser at 25°C. The inset shows the variations of the peak wavelength against the temperature at 250 mA.

The optical spectral linewidth has been measured using the delayed self-heterodyne (DSH) interferometric technique (Okoshi *et al.*, 1980). The experimental setup consists of an interferometer where the beam is split into

two portions. One portion is delayed by a 20 km fiber delay line, and the other portion is frequency shifted by an acousto-optic modulator (AOM), which is driven by a constant frequency (110 MHz). The superimposition of the two beams through a fiber-optic coupler is then detected by a photo-detector (PD). Its photo-current power spectrum is analyzed by an electrical spectrum analyzer (ESA) in order to extract the linewidth. An isolator is used to minimize the back-reflections into the laser. A commercial battery powered, ultra-low noise current source (model LDX-3620B) is used to drive the devices under test. The use of this battery is in order to minimize the effect of current supply noise on the measured linewidth (Dougherty *et al.*, 1999).

To extract the intrinsic linewidth (Lorentzian lineshape resulted from the spontaneous emission), we have applied a Voigt profile (Mercer, 1991; Spiessberger *et al.*, 2010) – defined as a convolution between the Gaussian and Lorentzian lineshapes – to the measured RF spectrum. The selection of the Voigt fitting arises from the fact that some broadening in the RF DSH beat note lineshape is observed near the center. This broadening can mainly be attributed to 1/f frequency noise (including environmental noise sources and injection current noise) whose corresponding lineshape is Gaussian (Telkkala *et al.*, 2011; Mercer, 1991; Spiessberger *et al.*, 2010). Fig.3. 22 shows the intrinsic linewidth ($\Delta\nu$) dependence on the inverse of the output optical power for 1500 µm-long CRW-DFB laser at 25°C. The variations of $\Delta\nu$ as a function of the driving current is shown in the top left of Fig.3. 22. An example of a normalized RF beat note spectrum with the Voigt fitting is shown in the right-bottom corner of Fig.3. 22. This illustration is for a laser that has been biased at 160 mA ($1/P = 0.38\ mW^{-1}$) at 25°C. The fitted Voigt profile to the measured RF beat note spectrum gives a full width at half maximum (FWHM) of 1.58 MHz, from which the extracted Lorentzian and Gaussian FWHMs are 0.8 and 1 MHz, respectively. Given that the DSHI technique is used for the linewidth determination, the intrinsic $\Delta\nu$ is half the Lorentzian part; *i.e.* 0.4 MHz. We see from Fig.3. 22 that for injection levels $\geq \sim 2.8\times I_{thr}$ the intrinsic $\Delta\nu \leq 250$ kHz with a minimum of 184 kHz obtained

at 300 mA. We believe that eliminating further sources of environmental noise would lead to narrower linewidths (Chen, 2006).

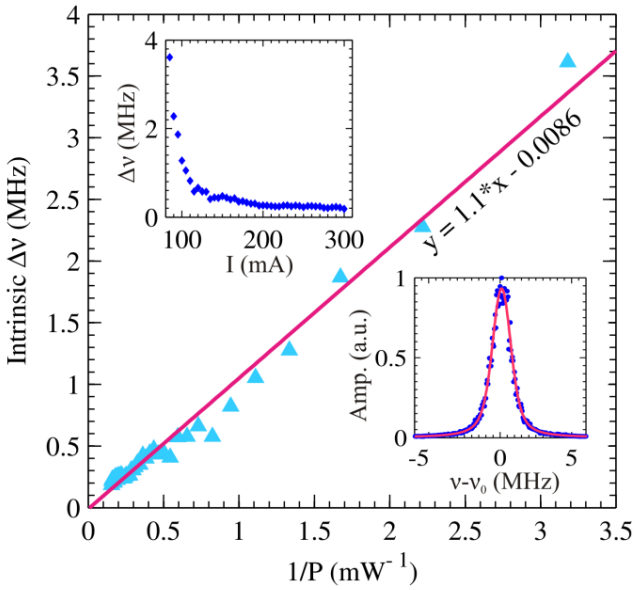

Fig.3. 22. Intrinsic linewidth variations for 1500 µm-long CRW-DFB laser as a function of the inverse of output power at 25°C. The top inset shows the variations of Δυ against the injection current. The bottom inset shows an example of normalized RF beat spectrum (at 160 mA) fitted with a Voigt profile.

Conclusion

An InGaAsP multiple quantum well 1550 nm corrugated ridge waveguide DFB laser based on third-order InP etched gratings has been demonstrated. The corrugated ridge waveguide has been defined by using the stepper lithography plus a reactive ion etching. Side mode suppression ratios ≥ 50 dB, output powers ≥ 7 mW, and a tuning coefficient of 0.095 nm/°C have been measured. Moreover, the fabricated laser showed narrow linewidths (≤ 250 kHz) for injection ≥ ~2.8×I_{thr} at 25°C. These characteristics along with the ease of fabrication and monolithic integrate-ability make our laser a distinctive source for advanced coherent optical communications, in particular for low cost photonics integrated circuits applications.

Chapter 4 |

Multi-electrode corrugated ridge waveguide DFB lasers

4.1. Motivation and novelty

A multi-electrode laser is a laser where its top contact is partitioned into at least two electrically isolated sections, as exemplified by Fig.4. 1. It is also known as a multi-section, multi-contact, or multi-segment laser. The idea behind this contact splitting is to create some sort of 'artificial' control of the carrier density distribution along the laser cavity by injection current control through each section. Changing the carrier density leads to gain peak and refractive index changes (*i.e.* non-uniformity of gain coefficient and refractive index), which in turn are responsible for assuring continuous wavelength tuning (Fang and Wang, 1984; Yoshikuni *et al.*, 1986; Yoshikuni and Motosugi, 1987).

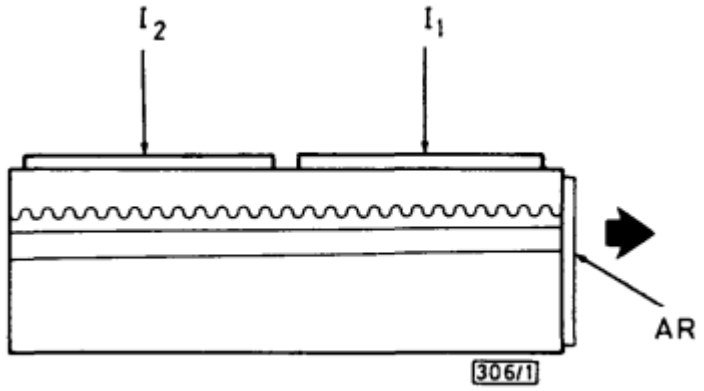

Fig.4. 1. Schematic structure of a semiconductor DFB multi-electrode lasers as proposed by (Yoshikuni *et al.*, 1986a)

Additionally, by tailoring the injected current density distribution to that of the light intensity, the net carrier density, and thus the index profile, becomes more uniform. Therefore, the longitudinal spatial-hole-burning effect can be effectively suppressed (Usami and Akiba, 1989). This entails significant enhancements to the laser performance in terms of its frequency modulation

(FM) and amplitude modulation (AM) characteristics, wavelength tunability, and spectral linewidth (Yoshikuni and Motosugi, 1987; Leclerc *et al.*, 1989; Fukuda *et al.*, 1989).

The idea of separated pumping in a semiconductor laser started by the group of S. Wang et *al.* in the 80's (Antreasyan and Wang, 1983; Fang and Wang, 1984). This concept has been then primarily applied to semiconductor DFB lasers by NTT Corporation (Yoshikuni *et al.*, 1986a; Yoshikuni and Motosugi, 1986b; Yoshikuni and Motosugi, 1987). Pure uniform (flat) FM responses have been obtained for frequencies up to a few hundred megahertz as shown in (Yoshikuni and Motosugi, 1987).

The concept of multi-electrode has been applied to semiconductor CRW-DFB lasers with different structure designs (*i.e.* using phase sections or separate waveguide sections). Besides, it has been mainly used with metal binary superimposed metal gratings, as shown in Fig.4. 2, at short wavelength (960 nm, Muller *et al.*, 2002) or at longer wavelengths (1200 nm, Naderi *et al.*, 2010), and (2800 nm, Lehnhardt *et al.*, 2010). This work is distinguishable in the facts that: (1) the cavity houses uniform and etched gratings without the recourse to the complexities of phase sections (Thought it has been difficult to achieve λ/4-phase-shift sections by the current available machine due to its resolution limitation), (2) The target emission wavelength is 1560 nm (forced by the gratings' pitch ~ 723 nm), (3) The 5× I-line optical stepper lithography technique has been used (with a minimum resolution ~ 365 nm), (4) InGaAsP separate confinement heterostructure multiple quantum well lasers have been grown using the metal-organic chemical vapor deposition (MOCVD). This is considered, to the authors' best knowledge, a novel advancement in this field.

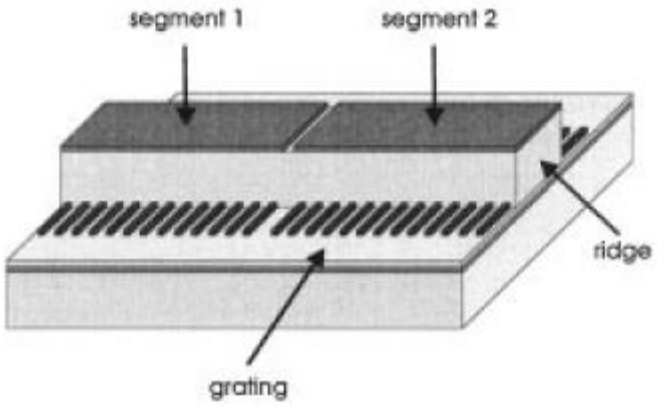

Fig.4. 2. Schematic diagram of two-section DFB laser with lateral Cr gratings (Muller *et al.*, 2002)

The current work entails the partition of the top electrode into different configurations as shown in Fig.4. 3. In section 4.2 we present the experimental results on lasers using configuration 1. In section 4.3 we present the experimental results on lasers with three electrodes (configurations 2 and 3).

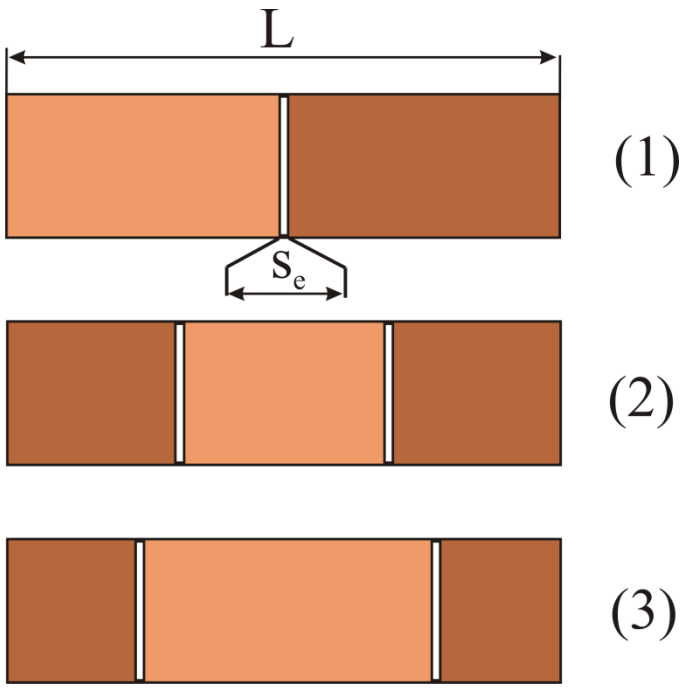

Fig.4. 3. Multi-electrode configurations (top view) for the CRW-DFB lasers as used in this work (L: cavity length; Se: inter-electrode spacing).

4.2. Two-electrode corrugated ridge waveguide DFB lasers

Summary

This section describes the design and experimental results of two electrode 1500 µm-long CRW-DFB lasers. The lasers oscillate in single-mode around 1560 nm with high side mode suppression ratios (>54 dB), a wavelength tuning (≥ 3 nm), an output power (> 6 mW), and narrow linewidth (<170 kHz) under various current injection ranges at room temperature. A minimum linewidth of 94 kHz has been recorded for 1500 µm-long two-electrode CRW-DFB laser while providing non-uniform current injection through the two electrodes.

Contribution

The results provided in this section have been accepted for publication in the Optics Express journal. I designed and built the experimental setups. I assisted and participated with Mr. Benhsaien in the active region design, waveguide modeling, and mask layout design for these devices. I generated and interpreted the experimental results, and wrote the manuscript. Dr. Zhang contributed to the design verification and validation at CMC before sending the devices for fabrication. Drs Hinzer and Hall contributed to the interpretation of the results and revision of the manuscript.

Article

The accepted paper follows. I have reproduced[3] the paper in the same format as the main thesis text (to accommodate for the overall thesis style).

[3] This includes the formatting (without content changes) of: the text, figures captions, and reference citations. I deleted the references section from the paper, given that they all appear in the bibliography section of the thesis.

Citation

K. Dridi, A. Benhsaien, J. Zhang, K. Hinzer, and T. J. Hall, “Narrow linewidth two-electrode 1560 nm laterally coupled distributed feedback lasers with third-order surface etched gratings," Optics Express, vol. 22, no. 16, pp. 19087-19097, Aug. 2014.

Narrow linewidth two-electrode 1560 nm laterally coupled distributed feedback lasers with third-order surface etched gratings

Kais Dridi,[1,*] Abdessamad Benhsaien,[1] Jessica Zhang,[2] Karin Hinzer[1,3], and Trevor J. Hall[1]

[1]Centre for Research in Photonics at the University of Ottawa, Photonics Technology Laboratory, 800 King Edward Avenue, Ottawa, Ontario, K1N 6N5, Canada

[2]CMC Microsystems, 1200 Montreal Road, M50-IPF, Ottawa, Ontario, K1A 0R6, Canada

[3]SUNLAB, Centre for Research in Photonics at the University of Ottawa, 800 King Edward Avenue, Ottawa, Ontario, K1N 6N5, Canada

[*]kais.dridi@uottawa.ca

Abstract: We report on the design and characterization of a re-growth free InGaAsP/InP multiple quantum well two-electrode laterally coupled distributed feedback (LC-DFB) lasers. Third-order surface etched gratings have been defined on the ridge sidewalls along the laser cavity by means of stepper lithography. The lasers oscillate in single-mode around 1560 nm with high side mode suppression ratios (>52 dB), a wavelength tuning (≥3 nm), an output power (≥6 mW), and narrow linewidth (<170 kHz) under various current injection ranges at room temperature. A minimum linewidth of 94 kHz has been recorded for 1500 μm-long two-electrode LC-DFB laser while providing non-uniform current injection through the two electrodes. The effect of the width of the inter-electrode gap on these different performance measures is also studied.

OCIS codes: (250.5960) Semiconductor lasers; (140.3490) Lasers, distributed-feedback.

4.2.1. Introduction

Although semiconductor distributed feedback (DFB) lasers have gained widespread applications (Funabashi *et al.*, 2004; Fish *et al.*, 2011; Briggs *et al.*, 2013; Nasim and Jamil, 2014), the formation of well-defined periodic gratings structure is the main challenge of DFB fabrication. Indeed, to ensure high single-mode yield with a high level of wavelength accuracy, it is of great importance to have a process that can simultaneously achieve low damage, uniform and reproducible gratings.

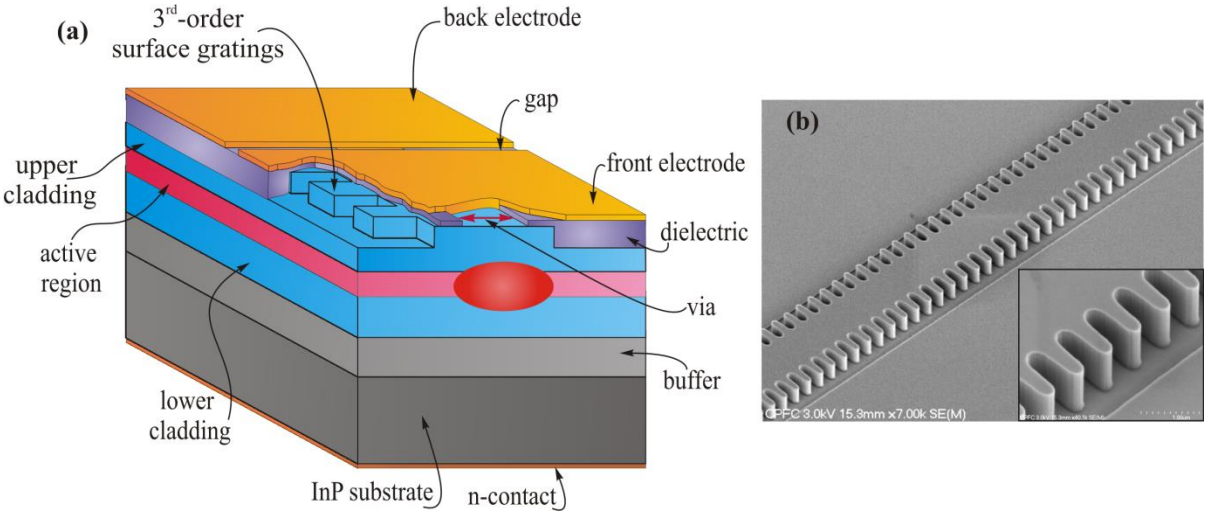

Fig.4. 4. 3D cutaway drawing for our two-electrode LC-DFB laser, (b) Scanning electron micrograph with different views for the actual fabricated ridge waveguide with third-order gratings.

If we look at the DFB fabrication, we find out that the gratings will be defined during an interruption in the growth process, or through an etch and regrowth process. These multiple growth techniques require additional processing steps that make them more complex and difficult to implement; they are used routinely, in particular for high-performance InGaAsP/InP based lasers for telecommunications, but are a source of yield and reliability problems. Laterally-coupled distributed feedback (LC-DFB) lasers (Miller *et al.*, 1991) combine the advantages of Fabry-Perots (single growth) with the wavelength performance of DFB lasers. In these lasers, the periodic gratings structure is

etched out of the upper growth layers that are used to form the ridge waveguide, as shown in Fig.4. 4. This process can be performed once all the epitaxy is done. In other words, there is no need for epitaxial regrowth or growth on corrugated layers as in DFB lasers fabrication, hence eliminating all the aforementioned shortcomings. Although an early demonstration of regrowth free DFB laser used gratings that have been etched on the ridge (Liau *et al.*, 1985), lateral gratings can be exclusively etched in the ridge sidewalls (*i.e.* corrugated ride waveguide lasers) (Miller *et al.*, 1991), exclusively beside the ridge (Martin *et al.*, 1995) or over both regions (Chen *et al.*, 1991). LC-DFB lasers that use metallic rather than etched semiconductor gratings on the cladding beside the ridge have also been investigated (Kamp *et al.*, 1999; Muller *et al.*, 2001).

Multi-electrode semiconductors lasers has been originally introduced by S. Wang's group (Antreasyan and Wang, 1983; Fang and Wang, 1984), and primarily applied to DFB lasers by Yoshikuni *et al.* (Yoshikuni *et al.*, 1986). The partition of the top electrode into two or more segments results in a laser cavity with electrically isolated sections. Accordingly, the control of current distribution through these sections allows an 'artificial' control of the carrier density distribution along the laser cavity. Changing the carrier density leads to gain peak and refractive index changes (*i.e.* non-uniformity of gain coefficient and refractive index). Indeed, these mechanisms are believed to be responsible for assuring both continuous tuning and frequency switching (Fang and Wang, 1984; Yoshikuni *et al.*, 1986; Yoshikuni and Motosugi, 1987). Additionally, by tailoring the injected current density distribution to that of the light intensity, the net carrier density, and thus the index profile, becomes more uniform. Therefore, the longitudinal spatial-hole-burning effect can be effectively suppressed (Usami and Akiba, 1989). This brings significant enhancements to the laser performance in terms of its frequency modulation (FM) and amplitude modulation (AM) characteristics, wavelength tunability, and spectral linewidth (Yoshikuni and Motosugi, 1987; Leclerc *et al.*, 1989; Fukuda *et al.*, 1989).

The concept of multi-electrode current injection has been applied to laterally coupled DFB lasers designs of different structures than the laser described herein. It has been mainly used with metal binary superimposed metal gratings at short wavelength (960 nm, Muller *et al.*, 2002) or at longer wavelengths (1200 nm, Naderi *et al.*, 2010), and (2800 nm, Lehnhardt *et al.*, 2010). In this work, we demonstrate a two-electrode multiple quantum well InGaAsP/InP LC-DFB laser operating at a wavelength of 1560 nm. The laser cavity has been defined by a ridge waveguide supporting uniform third-order etched InP gratings, as can be clearly recognized in Fig.4. 4(a). No λ/4-phase-shift or any other sections have been integrated. To the authors' best knowledge, this structure is novel and contributes to the advancement of the field by suggesting rooms for design and performance improvements for the LC-DFB lasers. In this paper, we report on the design, fabrication, and experimental characterizations of two-electrode LC-DFB lasers. Preliminary optical characteristics, such as light output and lasing wavelength, as well as linewidth determination have been carried out for different lasers with different inter-electrode spacing. In addition to the easy monolithic integrability that these devices offer, the experimental characterization reveals that this laser would be a strong candidate for applications such as photonics integrated circuits and advanced optical coherent communications.

The device design including the epitaxial layer structure and the fabrication technique have been described in (Dridi *et al.*, 2014a). It should be noted that, in this work, the active region has been designed to have a maximum gain at 1550 nm (Dridi *et al.*, 2014a) and the corrugated ridge waveguide has been defined with a gratings' pitch allowing an emission at 1560 nm.

4.2.2. Device characterizations

In this work, we consider two 1500 μm-long LC-DFB devices whose top electrode has been divided into two equal-length electrically isolated sections. The first device, L_1, has two 747-μm-long sections separated by an inter-electrode spacing

(E_S) of 6 µm. The second device, L_2, has an E_S of 10 µm separating two 745-µm-long sections. They have the same dynamic resistance of ~ 5 Ω, but with slightly different isolation resistances: 1300 Ω and 1500 Ω for L_1 and L_2, respectively. Both devices were fabricated with a corrugated ridge waveguide defined with third-order gratings uniformly etched along the whole cavity. The gratings are defined with a period of ~ 723 nm (*i.e.* emission wavelength of 1560 nm), a duty cycle of 0.55, a wide ridge width of 3 µm, a narrow ridge width of 1.5 µm, and an etch depth of 0.8 µm. A scanning electron micrograph of fabricated third-order gratings is provided in Fig. 4.4 (b).

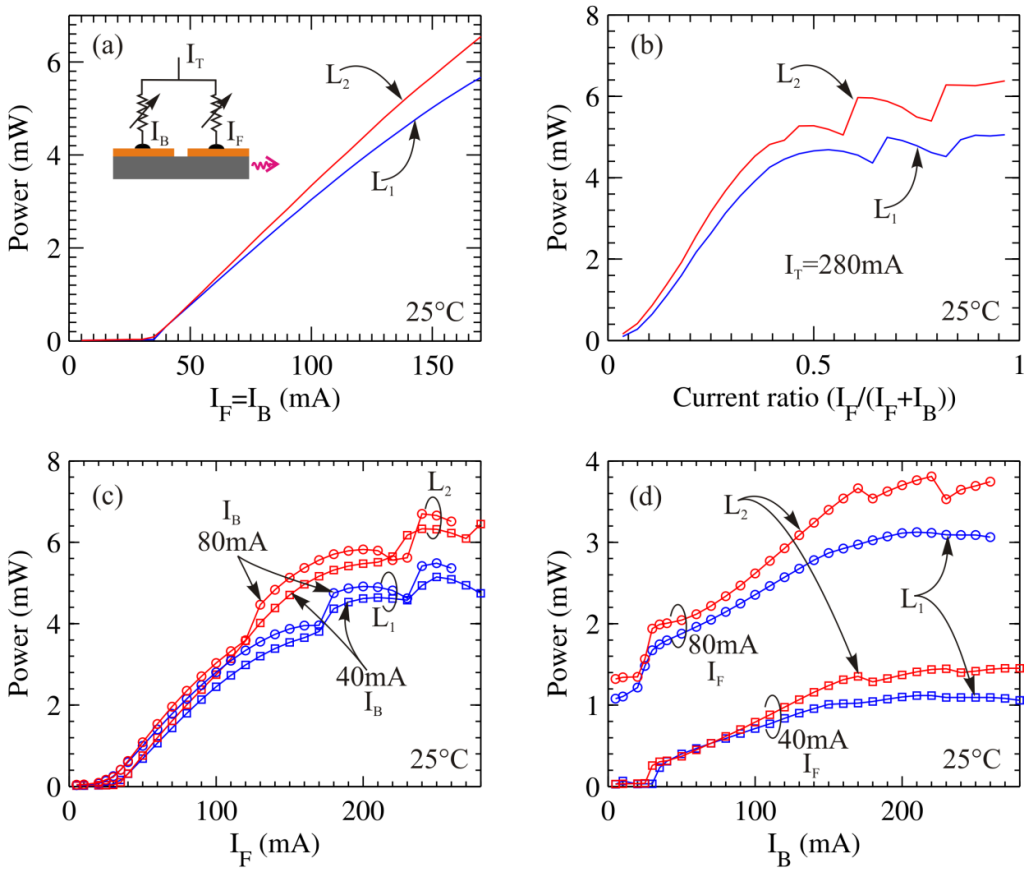

Fig.4. 5. Light output/front section characteristics for 1500 µm-long as-cleaved devices L_1 (E_S=6µm) and L_2 (E_S=10µm) at 25°C versus biasing current (E_S: inter-electrode spacing): (a) in the case of uniform injection (I_F=I_B), (b) at a constant total current I_T=280mA, (c) when varying I_F while keeping I_B at 40 mA and 80 mA, and (d) when varying I_B while keeping I_F at 40 mA and 80 mA.

The optical output power has been measured from the front facet of as-cleaved devices that have been mounted p-up on a temperature controlled copper plate. Typical continuous wave (CW) light-current (L-I) characteristics are reported in Fig.4. 5 under different biasing conditions. First we consider the case of uniform injection (*i.e.* both electrodes are equally pumped (I_F=I_B)), with I_F and I_B are respectively the front- and back-electrode currents, as depicted in the inset of Fig.4. 5(a), both lasers exhibited kink-free L-I characteristic and almost the same threshold current (I_{th}) of ~ 2×35 mA at 25°C, as shown in Fig.4. 5(a). The maximum differential quantum efficiency is slightly higher when considering larger spacing E_S: 0.04 and 0.05 for 6 µm (L_1) and 10 µm (L_2), respectively. Reasons behind this low efficiency have been discussed in (Dridi *et al.*, 2014a). Both devices can emit more than 6 mW CW power under single-mode operation up to a total biasing of ~ 4.85×I_{th}.

Considerable changes occur when we consider the case of non-uniform injection (*i.e.* both electrodes are not equally pumped). Indeed, Fig.4. 5(b) shows the variation of the optical output power against the current ratio I_F/I_T (at a constant total current I_T=(I_F+I_B)=280mA) at 25°C. In this case both devices showed almost the same characteristics, except with a higher power for the device with a larger inter-electrode spacing. Near the uniform injection (I_F/I_T=0.5), devices L_1 and L_2 exhibit a maximum power of ~ 4.6 mW and ~ 5.3 mW, correspondingly. After small variations, the power starts to stabilize at 5 mW and 6.3 mW towards a current ratio of ~ 0.85 for both L_1 and L_2, respectively. Fig.4. 5(c) shows the light output measured as a function of the current I_F while keeping I_B constant at different levels (40 mA and 80 mA). From this plot we can define a lasing threshold for the front electrode ($I_{F,th}$~ 22 mA) after which the output power increases rapidly with a better efficiency for the device L_2. Fig.4. 5(d) shows the case where the output power is plotted against the current through the back section I_B while keeping the front electrode current I_F biased at 40 mA and 80 mA. When I_F is fixed at 40 mA, both devices light output increase the moment the threshold for the back section ($I_{B,th}$~30mA) is reached.

This is an indication of the presence of gain and stimulated emission in this section (Kuo and Dutta, 1988). When I_F is above 40 mA, both devices start to lase in single mode at null back current. Overall, we notice that in all cases exemplified by Fig.4. 5, device L_2 shows slightly higher power than that of device L_1.

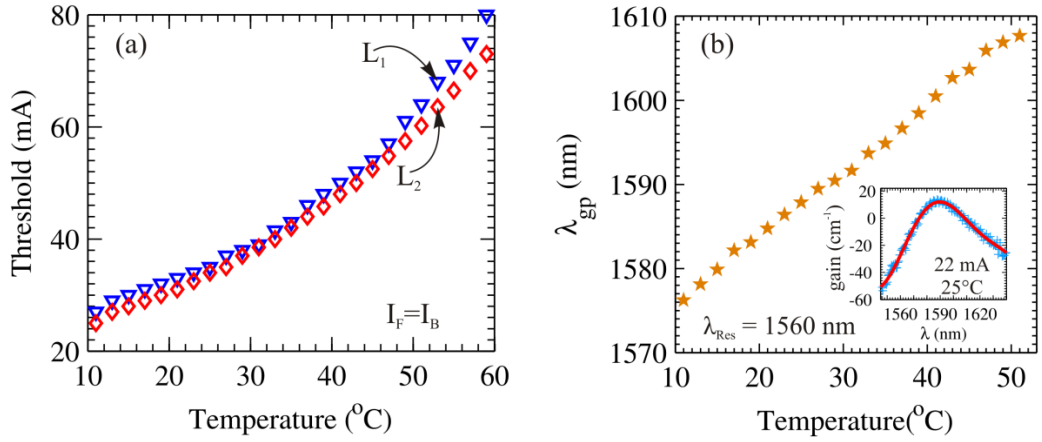

Fig.4. 6. (a) Threshold per electrode variations against temperature at uniform injection (I_F=I_B) for both devices (L_1 and L_2); (b) gain-peak wavelength (λ_{gp}) variations as a function of temperature (The inset shows the extracted modal gain from a 500 µm-long Fabry-Perot device fabricated on the same wafer as the LC-DFB lasers. The gain has been extracted using the Hakki-Paoli technique while the FP device has been biased at 22 mA under 25°C). (λ_{Res}: cavity resonance wavelength)

Fig.4. 6(a) discloses the threshold current variation as a function of the stage temperature for both devices while uniformly biased. Although, the threshold is slightly better for the device L_2, the overall measured threshold is considered as higher than anticipated. This can be mainly attributed to the spectral detuning between the gain peak and the cavity resonance wavelengths λ_{gp} and λ_{Res} (= 1560 nm), respectively, as can be seen in Fig.4. 6(b). The modal optical gain, as shown in the inset of Fig.4. 6(b), has been extracted from a typical uncoated 500 µm-long Fabry-Perot (FP) device (with a threshold of ~ 30 mA at 25°C) cleaved from the same wafer as the fabricated LC-DFB lasers. Indeed, this extraction epitomizes a spectral shift of ~ 30 nm between λ_{gp} (~1590 nm) and λ_{Res} at 25°C. The reasons behind this observation could be the inherent limitations of the

simulation software (LAS2D (Las2D, 2006)) used for the epitaxial structure design. In fact, the Inherent Las2D software limitations reside in the fact that Las2D does not support lattice-matched barriers to the InP substrate. Alone, the latter limitation affects the electronic structure of the active material. It shifts the conduction and valence eigenenergy levels in opposite directions in such a way that the effective (engineered) bandgap energy shoots up by an order of a meV. In addition, Las2D is optimized for an F-P cavity structure and the results of simulation have adapted to the actual LC-DFB structure. This approach disregards the particularities of the gain gratings, coupled to the refractive index gratings, from the actual material gain calculations. In addition, some current leaking may occur as in any ridge waveguide laser (Miller *et al.*, 1991), which could be another reason behind the large threshold values.

The single mode emission at 1560 nm is assured through a corrugated ridge waveguide defined with third-order gratings. In Fig.4. 7, we show the variations of the lasing wavelength and the side mode suppression ratios (SMSRs) under different injection conditions at 25°C. In the uniform injection case, devices L_1 and L_2 showed stable single-mode operation with an electronic tuning of 2.3 nm and 1.8 nm, respectively as can be seen in Fig.4. 7(a). The tuning rate ($d\lambda/dI$) is 0.019 nm/mA and 0.015 nm/mA for L_1 and L_2, respectively. The SMSR, the variations of which are shown in Fig.4. 7(b), is greater than 45 dB for wide biasing range for both devices with larger values for L_1. When considering non-uniform injection some interesting behaviours have been observed either in the lasing wavelength or in the SMSRs. Fig.4. 7(c) shows the lasing wavelength variations as a function of I_F at constant I_B values.

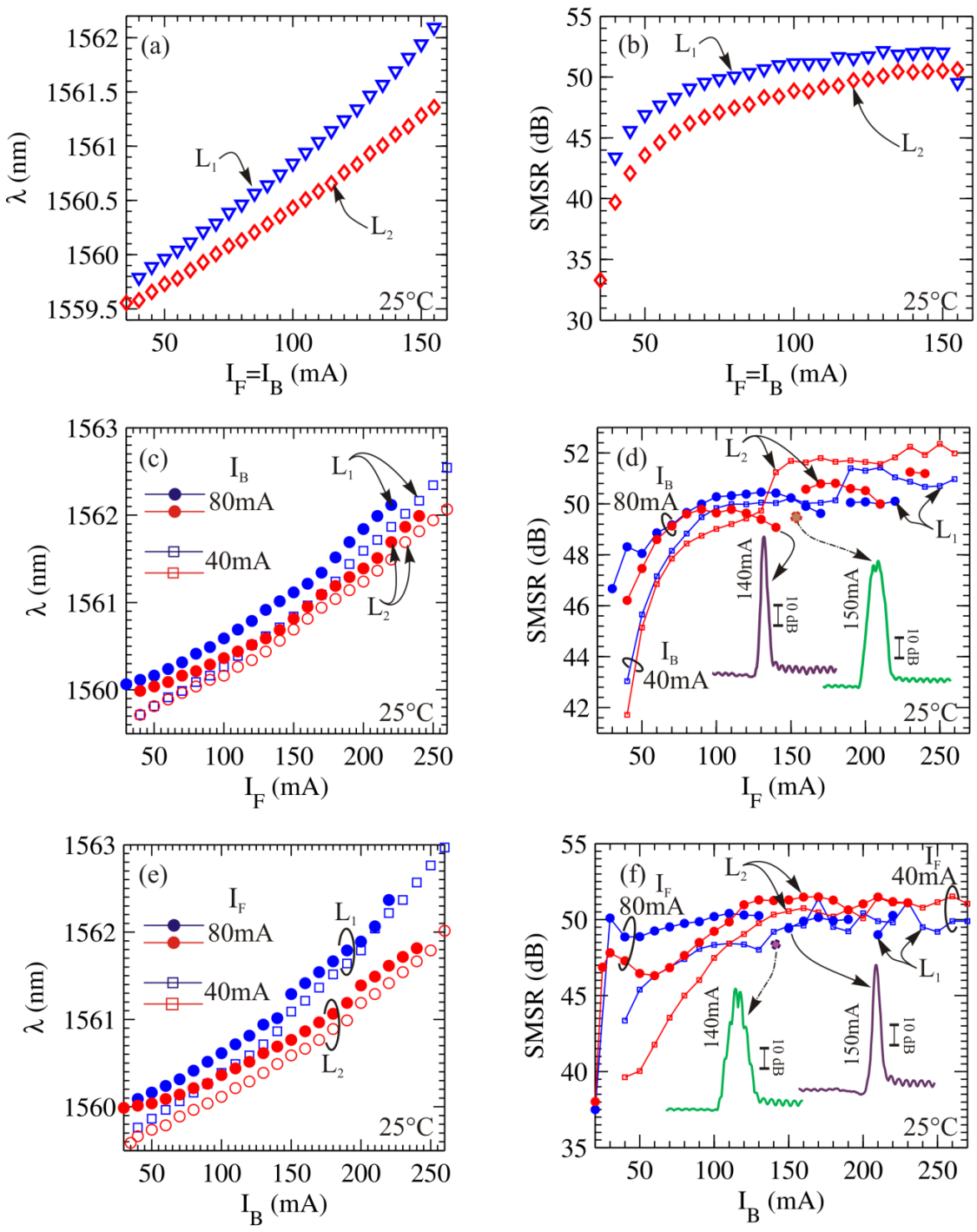

Fig.4. 7. Optical spectra characteristics for 1500 µm-long devices L_1 (E_S=6µm) and L_2 (E_S=10µm) at 25°C: Wavelength variations against (a) uniform injection, (c) front electrode current I_F while I_B fixed at 40 and 80 mA, and (e) back electrode current while I_F is fixed at 40 and 80 mA. SMSR variations at 25°C as a function of: (b) I_F=I_B; (d) I_F at I_B=40 and 80 mA, and (f) I_B at I_F=40 and 80 mA.

As can be seen in the summary Table 4.1 both devices show almost the same average tuning rate (~0.013 nm/mA). Device L_2 shows a slightly better tuning range. In the case where I_B is varied while I_F is fixed, device L_1 shows better results for both the average rate and tuning range, as can be seen in Fig.4. 7(e) and Table 4.1.

From these results, we see that the tuning range and rate depend not only on the inter-spacing between the electrodes (*i.e.* separating electrical resistance) but also on the biasing conditions. The observed tunability can be explained as the consequence of the artificial control of the carrier density distribution achieved through the injection current control via the electrodes (Yoshikuni *et al.*, 1986-a; Kuznetsov, 1988). Fig.4. 7(d) shows the SMSR variations as a function of I_F while maintaining I_B at constant levels. Once I_F reaches 90 mA and I_B is 40 mA, we recorded SMSR $\geq$ 50 dB whilst the second device L_2 shows better side mode discrimination than device L_1. When I_B is increased to 80 mA device L_1 shows better discrimination while I_F< 120 mA. Above this level device L_2 performs better. In this range (I_F>120mA and I_B=80mA) some side mode suppression degradation occurs for both devices: at I_F= 180 mA for L_1 and at I_F=150 and 220 mA for L_2. The inset of Fig 4.7(d) shows the optical spectra at I_F=140 and 150 mA for L_2, where in the latter case a multi-peak spectrum appears causing the SMSR degradation. Fig.4. 7(f) shows the SMSR variations against I_B while leaving the front electrode current fixed. When I_F is fixed at 40 and 80 mA, device L_2 performs better as I_B exceeds 110 mA. A degradation of side mode suppression is observed for L_1 around I_B = 140 and 200 mA while I_F = 80mA. The optical spectrum for L_1 at I_B = 140 mA is shown in the inset of Fig.4.7 (f). In these two cases, the optical spectra shown at the SMSR degradation points indicate that small mode hopping instability occurs at these particular section currents.

Table4. 1. Summary results regarding the rate of increase with bias current (dλ/dI) and tuning range (Δλ) for devices L_1 and L_2 in the non-uniform case at 25°C (in connection with Figs 4(c)and (e))

Device	I_B (mA)	dλ/dI (nm/mA)	Δλ (nm)	I_F(mA)	dλ/dI (nm/mA)	Δλ (nm)
L_1	40	0.013	2.83	40	0.015	3.37
	80	0.011	2.05	80	0.012	2.58
L_2	40	0.012	2.85	40	0.011	2.48
	80	0.011	2.18	80	0.009	1.9

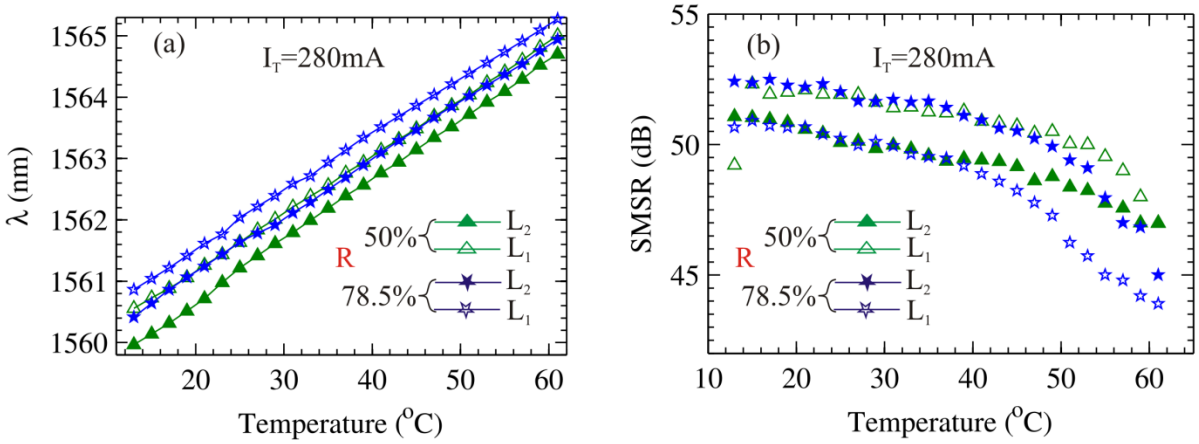

Fig.4. 8. Variations of: (a) the lasing wavelength and (b) the SMSR against the temperature for devices L_1 (E_S=6μm) and L_2 (E_S=10μm). Two injection current distributions have been used according to the current ratio R = $I_F/(I_F+I_B)$ = (50 and 78.5%).

Fig.4. 8 shows the variations of the lasing wavelength and SMSR against the stage temperature. Two different injection current schemes have been used while maintaining the total current I_T (≡I_F+I_B) fixed at 280 mA. In the first case the total current is evenly injected among the two electrodes (*i.e.* current ratio (R) = 50 %). In the second case, 78.5 % of the total current is injected into the front electrode. In the former case, devices L_1 and L_2 show respectively a tuning range of 4.45 and 4.74 nm and a red-shift temperature rate (dλ/dT) of 0.093 and 0.099 nm/°C as can be inferred from Fig.4. 8(a). The latter case shows that devices L_1 and L_2 demonstrate respectively a tuning of 4.41 and 4.53 nm and a rate of 0.092 and 0.093 nm/°C. Measurements of side mode discrimination are shown in Fig.4. 8(b); device L_1 performs well if the case of uniform injection is

considered, whereas device L_2 performs better if the non-uniform injection is considered. In the uniform injection L_1 shows better results than L_2. In contrast L_2 shows better results in the non-uniform injection case.

In order to determine the optical linewidth of these devices, we have used the delayed self-heterodyne interferometric (DSHI) technique (Okoshi *et al.*, 1980). The experimental setup consists of an interferometer where the beam is split into two paths. In one path the optical field is delayed by a 20 km fiber-optic spool, and in the other path it is frequency shifted by an acousto-optic modulator (AOM), which is driven by a constant frequency (110 MHz). The fiber delay line used in this work allows a measurement resolution of 10 kHz. At the output of the DSH setup, the mixing of the two beams is detected by a photo-detector (PD). The resulted photo-current power spectrum is then analyzed by an electrical spectrum analyzer (ESA) in order to extract the linewidth. In addition, an optical isolator has been used to minimize the back-reflections towards the laser under test. Besides, a commercial battery powered, ultra-low noise current source (model LDX-3620B) with a low noise filter (ILX LNF–320) have been used to drive the devices under test (in order to minimize the effect of source noise on the measured linewidth). In this section, due to the time-consuming nature of these measurements, we report only on the measurements that have been performed at 25°C.

Fig.4. 9(a) shows the detected RF beat note spectrum for 1500 μm-long laser L_2 while uniformly pumped. The broadening observed in the lineshape near the center of the beat note is a non-Lorentzian. It is rather a Gaussian broadening, which is due to extrinsic (technically avoidable) noise introduced by the immediate environment (Mercer, 1991; Spiessberger *et al.*, 2010). In such situations it is important to know the intrinsic or the real linewidth of the laser under testing. The Voigt profile – a convolution between Gaussian and Lorentzian profiles – allows simultaneous quantification of extrinsic noise (mapped by the Gaussian part) and the intrinsic linewidth (mapped by the Lorentzian part).

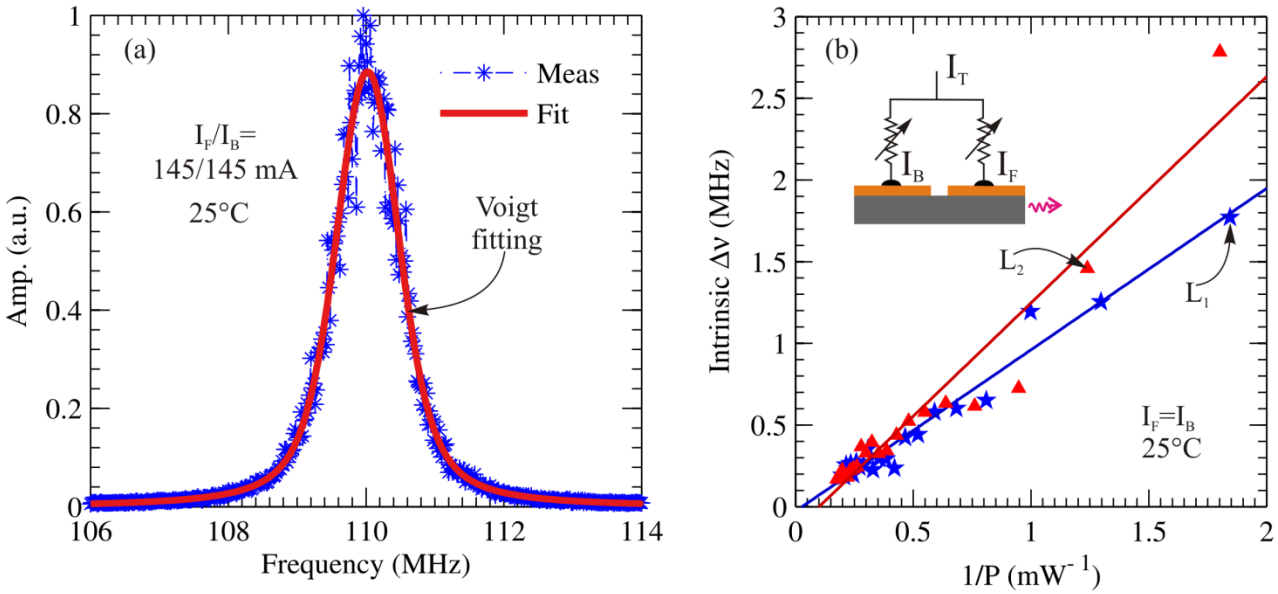

Fig.4. 9. (a) Measured RF beat note spectrum for device L_2 at 145/145 mA and 25°C (The experimental data has been fitted with a Voigt profile); (b) The variations of the intrinsic linewidth as a function of the inverse of output power for both devices in the uniform case (I_F=I_B) at 25°C. The inset shows the driving current scheme.

We therefore apply a Voigt fitting procedure (Spiessberger *et al.*, 2010; Telkkala *et al.*, 2011) to the measured RF beat spectrum as illustrated by Fig.4. 9(a). In this figure, the spectrum has been recorded at the output of the DSH setup for the laser L_2 pumped under the uniform injection case (at 145/145 mA). The Voigt fitting gives a full width at half maximum (FWHM) of 1.068 MHz, from which the extracted Lorentzian and Gaussian FWHMs are 0.339 MHz and 0.873 MHz, respectively. In the case of DSH method the intrinsic linewidth (δυ) is being the half of the Lorentzian part, hence the final linewidth is 169.5 kHz. Applying this procedure we have determined the linewidth δv for devices L_1 and L_2 in the uniform case (I_F=I_B). Fig.4. 9(b) shows the variations of the linewidth δυ for both devices as a function of the inverse power. For output powers ≥ 3 mW, both devices show linewidths ≤ 0.4 MHz. For instance, at a total injection level of 260 mA (*i.e.* I_F=I_B=130mA), device L_1 ($1/P_1$ = 0.234 mW^{-1}) show a δv_1 of 0.264 MHz whereas device L_2 ($1/P_2$ = 0.208 mW^{-1}) show a δv_2 of 0.19 MHz. The

minimum recorded linewidth δν is 184 kHz for device L_1 at I_T=290mA and 164 kHz for device L_2 at I_T=285 mA.

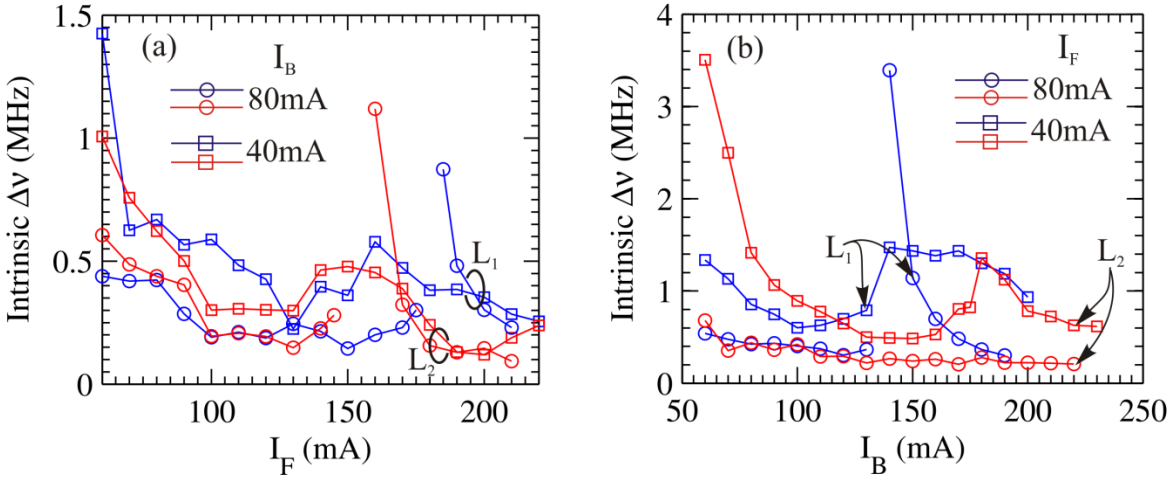

Fig.4. 10. Linewidth variations at non-uniform injection at 25°C for both devices L_1 and L_2: (a) variations of Δν against I_F at fixed I_B, and (b) variations of Δν against I_B at fixed I_F.

Additionally, following the above fitting procedure we have studied the variations of the intrinsic linewidth in the case of non-uniform injection, the results of which are summarized in Fig.4. 10. When varying the front current I_F while fixing the back current I_B, the linewidth decreases for both devices when I_B increases from 40 to 80 mA at 25°C, as depicted in Fig.4. 10(a). At I_B=40mA, device L_2 shows lower linewidths than device L_1 for most of the I_F injection range. When I_B=80mA both devices are alternately better from each other with a minimum δν of 144.5 kHz at I_F=150 mA for L_1 and 93.5 kHz at I_F=210 mA for L_2. In this latter case, an interesting phenomenon has been observed: two jumps occur in the linewidth variations at I_F = 180 and 150 mA for device L_1 and L_2, respectively. These jumps can be due to the degradation of the side mode suppression as depicted in Fig.4. 7(d). This is confirmed by the experimental observation made by Kuo and Dutta while they were characterizing standard semiconductor two-electrode DFB lasers (Kuo and Dutta, 1988). It is likely that a small mode jump occurs at these particular section currents (see for example Figs. 4. 7(e) and (f) when I_B=150 mA and I_F = 80 mA for device L_1) that can be

behind the linewidth rise (Murata *et al.*, 1987). In Fig.4. 10(b) we show the variations of δv against the back current I_B while maintaining I_F at constant levels. In this case the linewidth decreases for both devices when I_F increases from 40 to 80 mA at 25°C. At I_F=40mA, device L_1 shows lower linewidths than L_2 for $I_B \leq 125$ mA whereas the linewidth of L_2 becomes lower once $I_B > 125$ mA. When I_F=80mA both devices show almost similar linewidths up to I_B=130mA, after which L_2 shows narrower and more stable linewidths with a minimum $\delta\upsilon$ of 0.302 MHZ at I_B = 190 mA for L_1 and 0.22 MHz at I_B = 150 mA for L_2. In this case, a jump occurs for L1 at I_B=140mA while I_F is fixed at 80mA.

Table4. 2. Comparison of the linewidth δv (in MHz) for both devices L_1 and L_2 at uniform and non-uniform injection at different constant total current I_T at 25°C

I_T (mA)	Uniform injection		Non-uniform injection			
	L_1	L_2	L_1		L_2	
170	85/85	85/85	130/40	40/130	130/40	40/130
	0.236	0.343	0.283	0.757	0.341	0.581
210	105/105	105/105	130/80	80/130	130/80	80/130
	0.353	0.368	0.245	0.366	0.148	0.219
290	145/145	145/145	210/80	80/210	210/80	80/210
	0.184	0.169	0.230	-	0.0935	0.216

In general, the measured linewidths in the non-uniform case were narrower (≤ 150 kHz) than in the case of uniform injection for both devices. Table4. 2 shows a comparison between the linewidths obtained for devices L_1 and L_2 at different injection conditions. Depending on the biasing scheme, a narrow linewidth may be obtained. The narrow linewidth measured in this study could be attributed to the large detuning between the lasing wavelength and the gain peak wavelength. In this case an important reduction in the linewidth would be expected (Ogita *et al.*, 1987). In addition, it is well known that the linewidth is inversely proportional to the laser output power, which has been found to be relatively low in this study. However, the low measured linewidth enhancement factor (α) (≤1.79) around the lasing wavelength (1560 nm) compensates for the

low output powers. This low α-factor is in reasonable agreement with the observed linewidth given the large detuning of ~ -30 nm (*i.e.* the LC-DFB lasing wavelength is at the shorter side of the gain peak) (Ogita *et al.*, 1987; Liou *et al.*, 1987).

4.2.3. Conclusion

We have demonstrated narrow linewidth and single-mode two-electrode InGaAsP/InP LC-DFB lasers at 1560 nm. The ridge waveguide has been defined with uniform third-order InP etched gratings, which have been written by using I-line stepper lithography. The structure is very simple avoiding hence the recourse to the complexities of integrating other sections (such as λ/4 phase-shift) within the cavity. The top electrode has been partitioned into two equally and electrically isolated sections. We have studied the effect of the inter-spacing between the electrodes on some device performances under uniform and non-uniform injection. We have demonstrated narrow linewidth (<170 kHz) for wide injection range and under different biasing conditions. The lasers exhibited stable single mode operation with side mode suppression ratio in excess of 52 dB, a wavelength tuning range over 3 nm, and an output power over 6 mW. In addition to these preliminary features, the ease of fabrication and monolithic integrate-ability potential make our laser a distinctive source for advanced coherent optical communications as well as in other photonic-based applications where narrow linewidth is required. Further characterization such as the relative intensity noise and frequency modulation response measurements needs to be performed as a forward work in order to further assess the capability of these devices.

Acknowledgments

The authors would like to thank Joe Seregelyi for his helpful discussions and for providing both the isolator and the ultra-low noise source. The authors are very

thankful to Michel Poulin of Teraxion for fruitful discussions and his suggestions. The authors are also grateful to the Natural Sciences and Engineering Research Council (NSERC) for its support of this research; CMC Microsystems for its support of the device fabrication. Dr. Trevor Hall is a Canada Research Chair Tier I.

4.3. Three-electrode corrugated ridge waveguide DFB lasers

Summary

The experimental results of three electrode 1500 µm-long CRW-DFB lasers are presented in this section. These lasers have also been designed to oscillate in a single-mode around 1560 nm. At room temperature, we measured high side mode suppression ratios (>54 dB), a wavelength tuning (≥2.3 nm), an output power (≥7 mW), and narrow linewidth (≤120 kHz) under various current injection ranges and for different electrode partition. The effect of partitioning the top electrode is also studied through two different configurations. A minimum linewidth of 70 kHz has been recorded for 1500 µm-long two-electrode CRW-DFB laser while providing non-uniform current injection through the two electrodes.

Contribution

The results provided in this section have been accepted for publication in Optics Letters. I designed and built the experimental setups. I assisted and participated with Mr. Benhsaien in the active region design, waveguide modeling, and mask layout design for these devices. I generated and interpreted the experimental results, and wrote the manuscript. Dr. Zhang contributed to the design verification and validation at CMC before sending the devices for fabrication. Dr. Hall contributed to the interpretation of the results and revision of the manuscript.

Article

The submitted paper follows. I have reproduced[4] the paper in the same format as the main thesis text (to accommodate for the overall thesis style).

[4] This includes the formatting (without content changes) of: the text, figures captions, and reference citations. I deleted the references section from the paper, given that they all appear in the bibliography section of the thesis.

Citation

Kais Dridi, Abdessamad Benhsaien, Jessica Zhang, and Trevor J. Hall, "Narrow linewidth 1560 nm InGaAsP split-contact corrugated ridge waveguide DFB lasers," Optics Letters, vol. 39, no. 21, pp. 6197-6200, Nov. 2014.

Narrow linewidth 1560 nm InGaAsP split-contact corrugated ridge waveguide DFB lasers

Kais Dridi,[1*] Abdessamad Benhsaien,[1] Jessica Zhang[2], and Trevor J. Hall[1]

[1]Photonics Technology Laboratory, Centre for Research in Photonics, School of Electrical Engineering and Computer Science, University of Ottawa, 800 King Edward Avenue, Ottawa, Ontario K1N6N5, Canada

[2]CMC Microsystems, 1200 Montreal Road, M50-IPF, Ottawa, Ontario, K1A 0R6, Canada

*****Corresponding author: kais.dridi@uottawa.ca*

Received August 11, 2014; revised September 28, 2014; accepted September 28, 2014; posted September 29, 2014 (Doc. ID 220751); published October 22, 2014

We demonstrate a new split-contact corrugated ridge waveguide distributed feedback laser at 1560 nm. The laser cavity has been defined with uniform third-order gratings etched along the sidewalls of the ridge waveguide. The gratings were fabricated the standard I-line stepper lithography technique and etched with an inductively-coupled reactive ion etching process. Stable single mode operation has been achieved with side mode suppression rations ≥ 50 dB, output powers ≥ 7 mW, and a wavelength tuning range ≥ 2.3 nm, narrow linewidths (≤ 120 kHz) with a minimum of 70 kHz. The effect of p-contact partition on device performance is also studied.

OCIS codes: (250.5960) Semiconductor lasers; (140.3490) Lasers, distributed-feedback.

4.3.1. Introduction

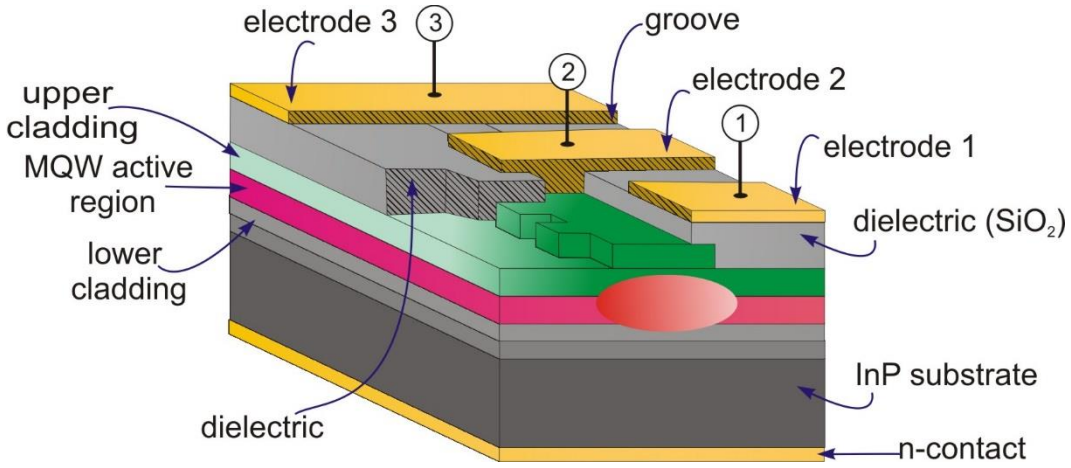

Fig.4. 11. 3D cutview of a split-contact electrode CRW DFB laser with three electrodes.

Semiconductor split-contact (or multi-electrode) distributed feedback (DFB) lasers have received considerable attention since their inception by Yoshikuni and Motosugi (Yoshikuni and Motosugi, 1986b). Indeed, it has been demonstrated that partitioning the top electrode into multiple electrically separated sections would result in pure frequency modulation and chirping suppressed amplitude modulation, in wide tuning range, and in narrow linewidths (Yoshikuni and Motosugi, 1986b; Yoshikuni and Motosugi, 1987; Kotaki *et al.*, 1989; Fukuda *et al.*, 1989; Eddolls *et al.*, 1992). Additionally, it is strongly believed that the injection current control through the different electrodes has a great impact on reducing the adverse spatial hole burning (SHB) to which single contact DFB lasers are prone (Kotaki *et al.*, 1989; Pan *et al.*, 1990). Although this solution would add significant enhancements to DFB lasers, they are still subject to fabrication limitation particularly when it comes to the gratings definition. In fact, it is all known that in standard semiconductor DFB lasers the gratings are being buried through epitaxial re-growth. This has been found to be challenging especially when it comes to the interface between the gratings and upper cladding layers (Miller *et al.*, 1991; Dridi *et al.*, 2014-a). To overcome the problem of regrowth, the gratings can rather be defined on the

ridge sidewalls, as exemplified in Fig.4. 11, once all the epitaxial layers have been grown. This describes what is known as laterally-coupled or corrugated ridge-waveguide (CRW) DFB lasers. It is hence obvious that this solution does not demand an overgrowth process, ultimately leading to a simplified fabrication process (Dridi *et al.*, 2014-a, and b). In addition, the use of low cost fabrication techniques, such as the stepper optical lithography, opens the doors for high-yield and low-cost manufacturing of CRW-DFB lasers making them ideal for commercial mass production. Moreover, CRW-DFB lasers offer an outstanding monolithic integrate-ability, which is a target key for affordable photonic integrated circuits, for example.

4.3.2. Experimental characterization

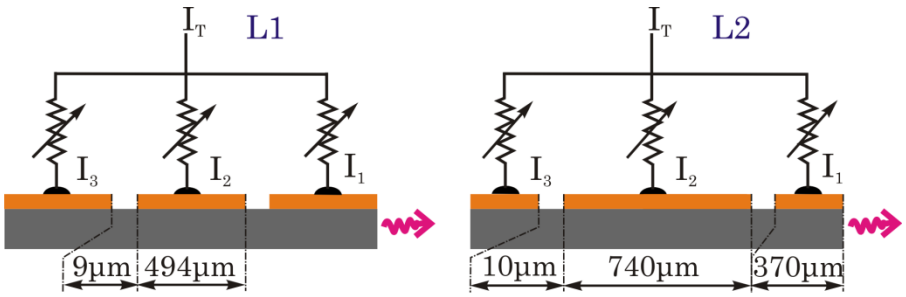

Injection scheme	L1	L2
Uniform	$I_1=I_2=I_3$	$I_1=I_3$ & $I_2/I_T=0.5$
Non-uniform	(1) vary I_T such that I_2/I_T~0.42 (2) vary I_2 such that $I_1=I_3=60$mA	

Fig.4. 12. Side view of the three-electrode CRW-DFB lasers (L_1 and L_2) used in this work. Injection current schemes and cases are also given.

We recently demonstrated a symmetrical split-contact CRW-DFB laser at 1560 nm (Dridi *et al.*, 2014-b). In this letter we zero in on the optical characterization of CRW-DFB lasers with three electrodes. Stable single-mode operation with wavelength tuning range ≥ 2.3 nm and narrow linewidths ≤ 140 kHz have been recorded. The effect of the p-contact partition on the device performance has also

been studied by considering two different 1500 µm-long devices as exemplified by Fig.4. 12. The first device, L_1, has three equal 494 µm-long electrodes separated by 9 µm-wide grooves. The second device, L_2, has a 740 µm long center section and two equal-side electrodes 370 µm each, with 10 µm-wide separation grooves. The measured isolation resistances between adjacent electrodes are 1630 Ω and 1800 Ω for devices L_1 and L_2, respectively. The devices have been fabricated with a ridge waveguide that has the same dimensions as in (Dridi *et al.*, 2014-b). The fabricated third-order gratings showed a normalized coupling coefficient of 1.5. The tested devices were as-cleaved and have been mounted on an accurate temperature-controlled stage.

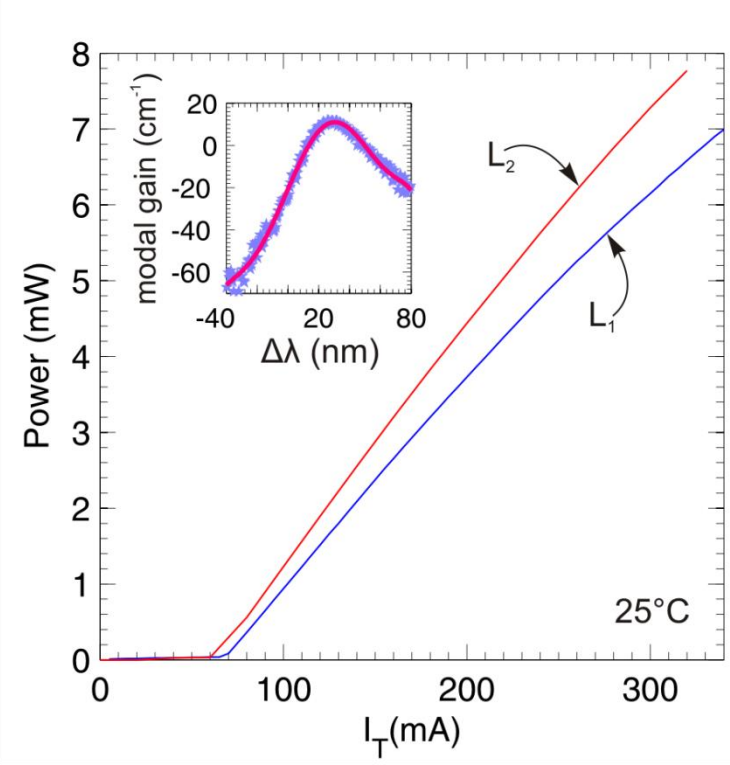

Fig.4. 13. Light-power characteristics for L_1 and L_2 at 25°C under uniform injection. The inset shows the modal gain extracted from a FP device.

Fig.4. 13 shows the light/current characteristic of both devices, L_1 and L_2, under uniform current injection at 25°C. The continuous wave (CW) threshold currents are 68 mA and 60 mA for L_1 and L_2, respectively. The maximum slope efficiencies η are 0.03 and 0.036 for L_1 and L_2, respectively. Both devices can

emit output powers ≥ 7 mW. These values are comparable to the ones obtained with one electrode devices and reasons behind the low efficiency and power values have been discussed in (Dridi *et al.*, 2014-a and b). Nevertheless, we have noticed that the threshold values are lower than the ones obtained either for one-electrode (Dridi *et al.*, 2014-a) or two-electrode (Dridi *et al.*, 2014-b) CRW-DFB lasers. This is a significant sign that the SHB effect has been reduced by considering the three-electrode configuration, as has been demonstrated (Usami and Akiba, 1989). Figure 4.14 (a) shows the variations of the output power at 25°C in the nonuniform injection case (2), whereas Figure 4.14 (b) shows the variations of the output power against the ratio I_2/I_T while I_T =280mA at 25°C.

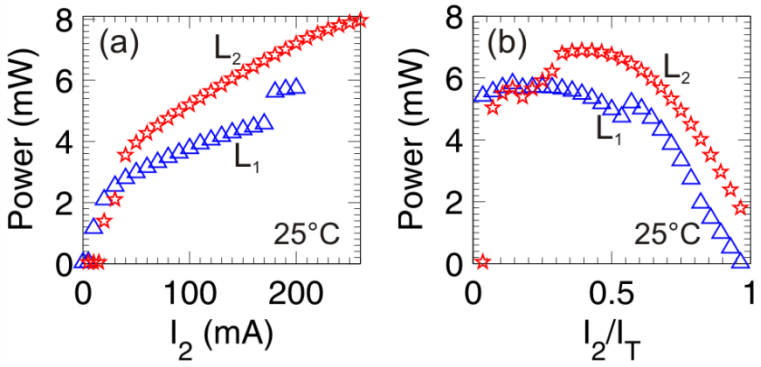

Fig.4. 14. Variations of the output power: (a) in the non-uniform injection case (2), and (b) as a function of I_2/I_T at 25°C (I_T =280mA).

Moreover, stable single mode operation and high side mode suppression ratios (SMSRs) for a wide range of injection currents and at different temperatures have been obtained. Indeed the measured SMSRs exceed 50 dB under different biasing schemes: in the uniform injection case as shown in Fig.4. 15 (a), and the non-uniform injection cases (1) and (2) as shown in Figs.4. 15 (b) and (c). In these three cases, device L_2 shows better results in terms side mode discrimination in comparison to device L_1. In terms of temperature dependence, device L_2 shows better SMSR performance than L_1 in either injection schemes, as can be seen Fig.4. 15(d). In Fig.4. 15(d), the total current I_T was kept at 280 mA: In the uniform case, device L_1 has been driven by considering $I_1=I_2=I_3=I_T/3$ whereas device L_2 has been driven at $I_1=I_3=70$ mA and $I_2=140$ mA; In the non-uniform

case, a biasing at I_1=I_3=60 mA and I_2=160 mA has been applied for both L_1 and L_2. Stable single-mode operation with SMSR > 40 dB has been observed for L_2 at temperature ≥ 80°C.

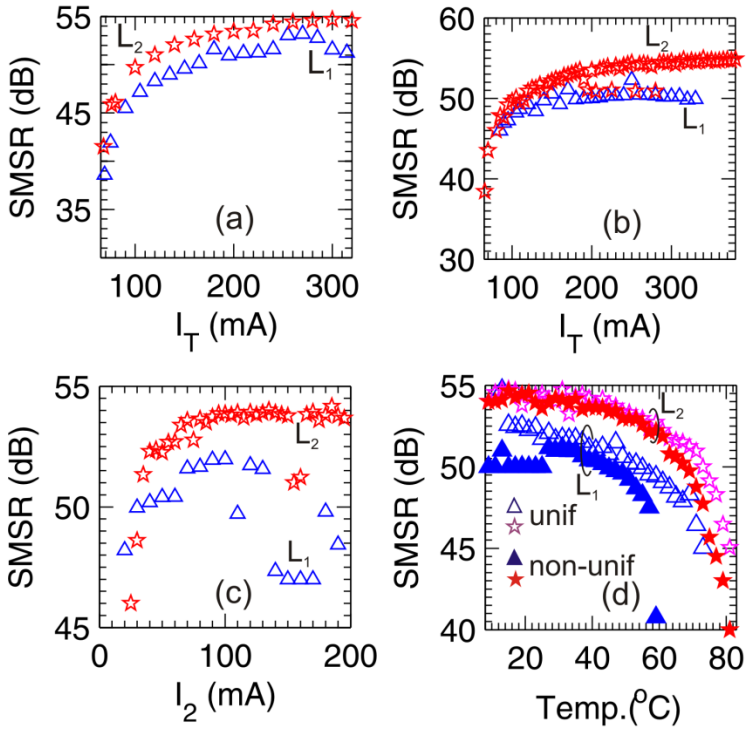

Fig.4. 15. SMSR variations: (a) in the uniform injection case; (b) and (c) in the non-uniform injection cases (1) and (2), respectively; (d) as a function of temperature.

Additionally, continuous wavelength tunability without mode hopping has been obtained depending on the p-contact partition and current injection scheme. In fact, under uniform injection and at 25°C, both devices, L_1 and L_2, show a tuning range of ~ 1.7 nm as can be seen in Fig.4. 16(a). When considering the non-uniform case (1) the tuning range has increased to ~ 1.8 and 2.3 nm at 25°C for L_1 and L_2 respectively as shown in Fig.4. 16(b). In the non-uniform injection case (2) a tuning range of ~ 1.45 nm has been measured for both L_1 and L_2 at 25°C as shown in Fig.4. 16(c). This shows that by tailoring the biasing injected current through the three electrodes wide frequency tunability may be obtained. As for the temperature dependency, it is clear as in Fig.4. 16(d), that L_2 can still be tuned at high temperatures when compared to L_1 while both

devices were being biased at 60/160/60 mA. The increase in temperature showed a red-shift lasing wavelength at a rate dλ/dT of 0.0927 and 0.0946 nm/°C for L_1 and L_2, respectively.

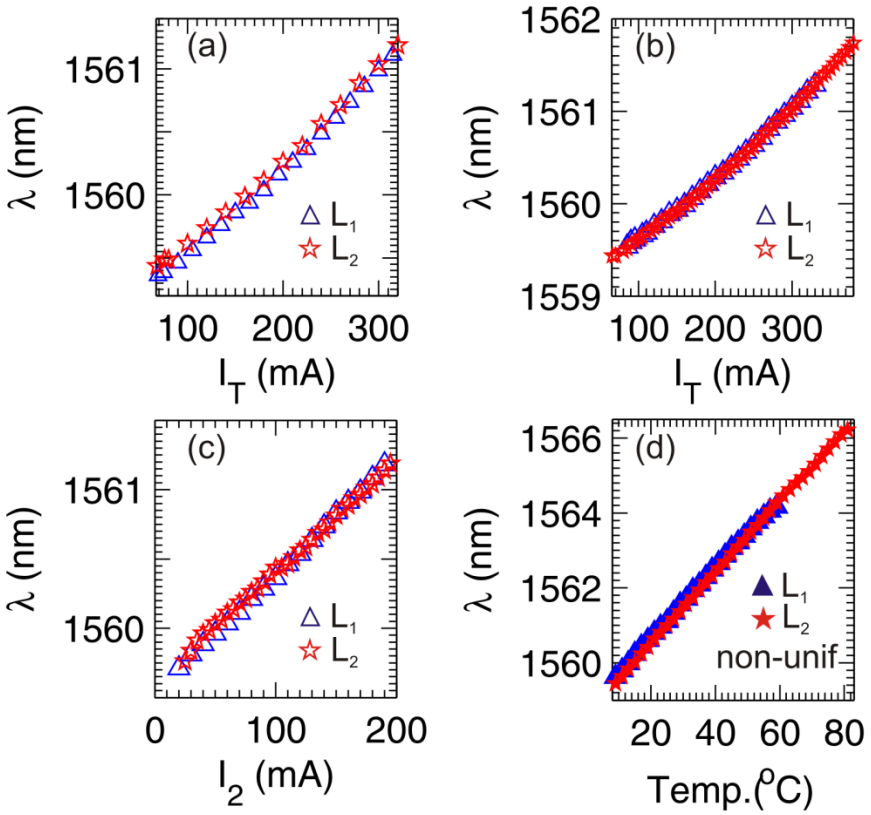

Fig.4. 16. Lasing emission wavelengths variations: (a) in the uniform injection case; (b) and (c) in the non-uniform injection cases (1) and (2), respectively; (d) as a function of temperature.

The optical spectral linewidth has been carried out using the common delayed self-heterodyne (DSH) interferometric technique (Okoshi *et al.*, 1980). The experimental setup as well as the procedure of the extraction of the intrinsic linewidth has been described in (Dridi *et al.*, 2014-a, and b). Figure 4.17(a) shows an example of a beat note for laser L_2 biased at 180 mA in the non-uniform case (2), defined in Fig.4. 12. The fitted Voigt profile gives a full width at half maximum (FWHM) of 0.969 MHz, from which the extracted Lorentzian and Gaussian FWHMs are 0.522 and 0.645 MHz, respectively. Keeping in mind that the DSHI technique assumes that the intrinsic linewidth is the half of the Lorentzian part, the final linewidth is 0.261 MHz.

Following this procedure (Dridi *et al.*, 2014-a, and b) we have studied the dependence of the linewidth on various injection conditions. Figure 4. 17(b) shows the intrinsic linewidth (δν) dependence on the total current I_T for L_1 and L_2 while being uniformly biased. Both devices showed almost the same linewidths with lower values for L_2 at total injection exceeding 260 mA. The minimum recorded δυ is 0.1805 and 0.162 MHz for respectively L_1 at 260 mA and L_2 at 280 mA. When considering the non-uniform injection, L_2 shows lower linewidths than L_1. Indeed, Fig.4. 17(c) shows the variations of δυ against I_T in the non-uniform injection case (1). In this case the minimum δυ is 0.1 MHz for L_1 and 0.070 MHz for L_2 both at 290 mA.

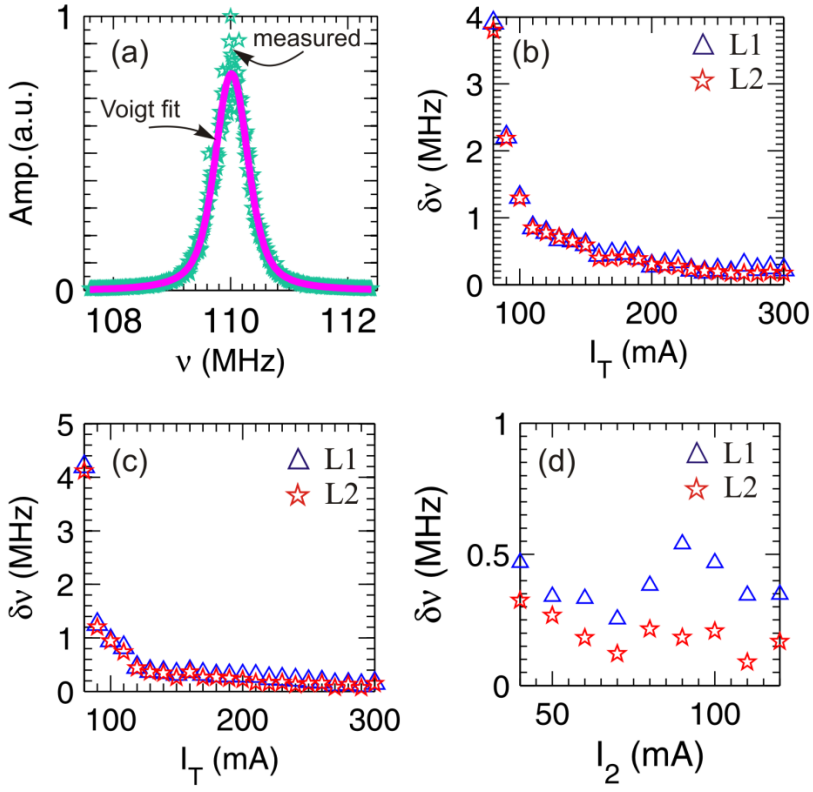

Fig.4. 17. (a) RF beat note with the Voigt fitting for the laser L2 biased at 180 mA (non-uniform injection case (2)) at 25°C; linewidth variations (b) in the uniform case; (c) and (d) in the non-uniform cases (1) and (2), respectively.

Figure 4.17(d) shows the δυ variations in the non-uniform injection case (2). In this case, L_2 shows lower δυ than L_1 for all the I_2 injection range, with a

recorded minimum of 0.250 MHz and 0.090 MHz for L_1 at 60/70/60 mA and L_2 at 60/110/60 mA, respectively. These results demonstrate how useful the consideration of CRW-DFB lasers with multi-electrode could be in terms of narrow linewidths, as was demonstrated earlier with standard DFB lasers (Kotaki *et al.*, 1989; Fukuda *et al.*, 1989; Eddolls *et al.*, 1992).

Although the output power for these devices was relatively low for the observed linewidth, the large detuning between the lasing wavelength and the gain peak wavelength (See inset of Figure 4.13) could be an important factor behind the narrow linewidth measured in this study as has been found in (Ogita *et al.*, 1987). Moreover, the low measured linewidth enhancement factor ($\alpha \leq 1.8$) around the lasing wavelength (1560 nm) compensates for the low output powers. This low α-factor is in reasonable agreement with the observed linewidth, given the large detuning of ~ -30 nm (*i.e.* the lasing wavelength is at the shorter side of the gain peak) (Ogita *et al.*, 1987; Liou *et al.*, 1987). Moreover, in comparison to the results obtained for two-electrode CRW-DFB lasers (Dridi *et al.*, 2014-b), we have noticed that the devices in this study show: (*i*) more stable linewidth variations (i.e. in other words, no linewidth jumps have been observed under different current injection conditions); (*ii*) in general narrower linewidth values depending on the biasing conditions and the electrode partition. These low values could also be attributed to the fact that the current injection through the three electrodes creates some sort of symmetric distribution for the optical field profile inside the laser cavity. This distribution would effectively reduce the SHB effect, which in turn gives rise to reduced spectral linewidths (Pan *et al.*, 1990; Usami *et al.*, 1989). Equally important, we have to mention that the observed low linewidths were possible thanks to the use of the ultralow noise source LDX-3620, which have shown small drive-current noise impact on the measured linewidth (Duan and Gallion, 1991).

4.3.3. Conclusion

We have demonstrated InGaAsP/InP split-contact corrugated ridge waveguide distributed feedback lasers at 1560 nm. Third-order gratings have been defined

and etched uniformly along the cavity using the I-line optical stepper lithography plus a reactive ion etching. The experimental characterization revealed that stable single mode operation has been achieved with side mode suppression rations ≥ 50 dB, output powers ≥ 7 mW, and a tuning coefficient of 0.095 nm/°C, depending on the electrode partition. Moreover, under different biasing conditions, narrow linewidths (≤ 140 kHz) with minimum of 70 kHz have been recorded. In addition to these features, these sources offer any easy monolithic integrability with other devices, which make them distinctive sources for the recent advanced coherent optical communication systems.

Acknowledgments

The authors would like to thank Joe Seregelyi for his helpful discussions and for providing both the isolator and the ultra-low noise source. The authors are also grateful to the Ontario Graduate Scholarship program. They are also thankful to the Natural Sciences and Engineering Research Council (NSERC) for its support of this research; CMC Microsystems for its support of the fabrication process. Dr. Trevor Hall is grateful to the Canada Research Chair (CRC) program for their support of his CRC-I in Photonic Network Technology.

Chapter 5 |

Towards time-domain modelling for corrugated ridge waveguide DFB lasers

Summary

This work was driven by the need to develop software that can handle the modeling of corrugated ridge waveguide DFB laser structures. Such a model does not exist in the literature nor has been made commercially available. Basically the numerical model aims at capturing the dynamical behaviour of these lasers. The initial goals for this model are to help predicting the laser performances given particular design parameters. In this chapter, a time domain model based on the traveling-wave approach for CRW-DFB lasers is described. The model allows studying the effect of geometrical parameters on the effect of longitudinal spatial hole burning and on the prediction of steady-state optical spectra.

Contribution

I have been very closely working with Dr. Akrout in this paper: establishing the literature review, deriving the theoretical equations, implementing the numerical code using Matlab, writing the manuscript and interpreting the results. Dr. Hall contributed to the interpretation of the results and the revision of the manuscript.

Article

The published paper follows. I have reproduced[5]the paper in the same format as the main thesis text.

[5] This includes the formatting (without content changes) of: the text, figures captions, and reference citations. I deleted the references section from the paper, given that they all appear in the bibliography section of the thesis.

Citation

A. Akrout, K. Dridi, and T. J. Hall, "Dynamic Analysis of High-Order Laterally Coupled DFB Lasers Using Time-Domain Traveling-Wave Model," IEEE Journal of Quantum Electronics, vol. 48, no. 10, pp. 1252-1258, Oct. 2012.

Dynamic Analysis of High-Order Laterally Coupled DFB lasers using time domain traveling wave model

A. Akrout, K. Dridi and T.J. Hall, *Member, IEEE*

Abstract— This paper describes the application of a time-domain modeling approach for laterally-coupled distributed feedback (LC-DFB) semiconductor laser for the first time. We numerically studied the effect of the radiation modes on LC-DFB laser properties. We have integrated the Streifer's coefficients, which represent the effects of radiation and evanescent modes, into the time-domain coupled wave equations. High-order corrugated gratings with λ/4 phase-shit are analyzed, where the degree of longitudinal spatial hole burning (LSHB) can be effectively reduced by means of fine tuning of the grating duty cycle. Additionally, we show a remarkably enhanced side-mode suppression ratio (SMSR).For example for the 3rd-order gratings with 50 % duty cycle a SMSR as high as 45 dB can be predicted.

Index Terms— High-order gratings, laterally-coupled distributed feedback (DFB) lasers, longitudinal spatial hole burning, time-domain coupled-wave equations.

5.1. Introduction

Semiconductor distributed feedback (DFB) lasers use buried Bragg gratings to achieve selective optical feedback and, hence, to ensure single mode operation. Such structures usually require two or more epitaxial-growth steps (Sakai *et al.*, 1982). Regrowth leads to difficulties associated with complicate fabrication, and ultimately increases the device cost. In laterally-coupled ridge waveguide DFB (LC-DFB) lasers, the gratings are lithographically patterned out of the ridge

waveguide sidewalls on the top cladding layer (Schreiner *et al.*, 2001; Das *et al.*, 2004) - as shown in our designed laser cavity in Fig.5. 1. The corrugated ridge waveguide induces index modulation, which interacts with the lateral optical fields (*i.e.* evanescent fields) to provide the optical feedback. Such design allows LC-DFB laser fabrication without any epitaxial regrowth as demanded in conventional DFB lasers and, hence, simplifies the fabrication process, increases the yield and, ultimately, reduces manufacturing cost (Tolstikhin *et al.*, 2009b; Choi *et al.*, 1996). Moreover, the surface-gratings structure lends itself to monolithic integration with other optoelectronic devices (Tolstikhin *et al.*, 2009a).

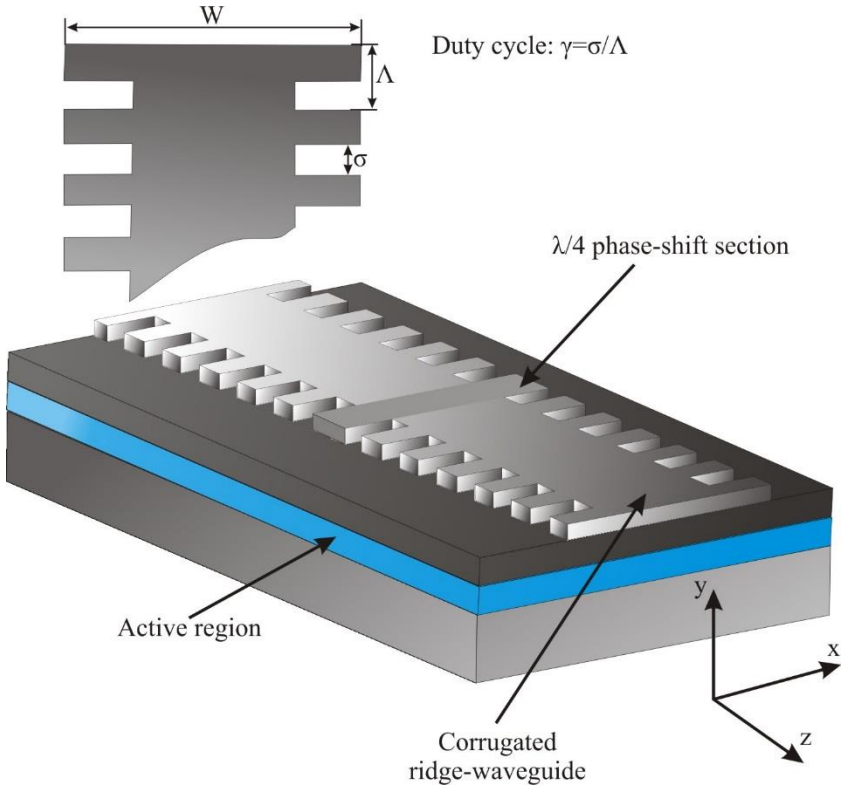

Fig.5. 1. 3D schematic of the gratings structure for our LC-DFB laser cavity design. W: wide ridge width, Λ: gratings period, and σ: wide ridge length.

Using high order-gratings is more suitable from the manufacturing viewpoints. It results in relative ease of mass production with longer pitches, when compared to the first order devices, which offers more relaxed fabrication

tolerances (Millet *et al.*, 2011). As one of the key design parameters in LC-DFB lasers is the coupling coefficient (Laasko *et al.*, 2009; Millet *et al.*, 2010), these devices require deep and finely-etched gratings to maintain acceptable performance whereas with higher orders a better degree of precision is achieved with standard lithographic techniques (Chen *et al.*, 2000; Muller *et al.*, 2002; Reid *et al.*, 2003; Millet *et al.*, 2008c).

The frequency chirp and mode stability are considered to be the major parameters that reduce the performance of conventional DFB lasers. Considerable development work has been done on standard DFB lasers (Vankwikelberge *et al.*, 1990; Li *et al.*, 1998; Champagne *et al.*, 1999) and several models have shown - especially when high-order gratings are considered - that the longitudinal spatial hole burning (LSHB) have significant influence on the mode stability as well as the modulation response of devices (Kazarinov *et al.*, 1985; Wiinshe *et al.*, 1993; Zhang *et al.*, 1994). However, for higher orders LC-DFB (Zhong *et al.*, 2004a-b) comparatively little design work exists; especially when considering the transient response of the laser.

LC-DFB lasers with high-order gratings have been previously analyzed using the modified coupled-mode (MCM) theory (Millet *et al.*, 2008a). The MCM theory of Streifer (Streifer *el al.*, 1977) has been extended into two dimensions, taking into account the effect of both radiating partial waves and grating variation in the 2D transverse section (Millet *et al.*, 2008a). However, this time-independent model did not take into consideration important key parameters such as the LSHB and the side-mode suppression ratio (SMSR). To the best of our knowledge, no time-domain modelling has been yet advanced for DFB lasers with laterally-corrugated gratings. The purpose of this paper is to study the effect of considering high-order gratings on the transient performance of LC-DFB lasers.

This paper is organized as follows: in section 5.2, we present a relatively simple self-consistent dynamic model based on a direct solution of the time-dependent MCM equations. The model takes into account the spontaneous emission, the longitudinal variations of carrier density, photon distribution, the refractive index and radiating partial waves. In section 5.3, we present the effect of high order gratings in LSHB versus the gratings duty cycles. The steady state spectra for high order gratings versus duty cycle will be also discussed. Finally, conclusions are given in section 5.4.

5.2. Theory and numerical technique

Time-domain model

The LC-DFB laser studied in this paper has uniform rectangular-shaped gratings including a λ/4 phase-shift section in the middle, as shown in Fig.5. 1. The time-domain (TD) large-signal travelling-wave model (Zhang *et al.*, 1992; Marcenac, 1994) has been used to model this surface-gratings DFB laser. The laser cavity is divided into M cascaded small sections. The section length (or the sampling spatial interval) is $\Delta z=L/M$, and the sampling time interval is defined through the speed of the light in the waveguide by $\Delta t=\Delta z/v_g$. The TD model is basically built to solve the time-dependent modified coupled-wave equations at discrete points (defined by the number of sections).

Quasi-TE mode (Millet *et al.*, 2008a) is considered in this paper. The electrical field in the waveguide can be written as a combination of forward $F(z,t)$ and backward $B(z,t)$ travelling waves:

$$E(z,t)=\left\{F(z,t)e^{-i\beta_0 z}+B(z,t)e^{+i\beta_0 z}\right\}\times e^{-i\omega_0 t} \tag{5.1}$$

where β_0 is the propagation constant at the Bragg frequency ω_0 (or reference frequency). The traveling optical fields $F(z,t)$ and $B(z,t)$ satisfy – under the slow varying envelope approximation – the following time-dependent coupled-wave equations (Zhang *et al.*, 1994):

$$\frac{1}{v_g}\frac{\partial F(z,t)}{\partial t}+\frac{\partial F(z,t)}{\partial z} = (g-\alpha_s-i\delta-i\varsigma_1)F(z,t)+i(\kappa_p{}^*+\varsigma_2)B(z,t)+Spn_f \quad (5.2a)$$

$$\frac{1}{v_g}\frac{\partial B(z,t)}{\partial t}-\frac{\partial B(z,t)}{\partial z} = (g-\alpha_s-i\delta-i\varsigma_3)B(z,t)+i(\kappa_p+\varsigma_4)F(z,t)+Spn_r \quad (5.2b)$$

where v_g is the group velocity in the waveguide; g is the field gain; α_s accounts for the waveguide scattering and absorption loss; δ is the detuning factor; and κ_p denotes the coupling coefficient between the contra-directionally propagating waves due to the gratings in the waveguide. We have introduced the Streifer terms $\varsigma_{i\ (i=1..4)}$ (Millet *et al.*, 2008a; Streifer *et al.*, 1977), which describe the effects of other partial waves, including evanescent fields and radiation, to study the operational impact of higher-order laterally-coupled gratings on LC-DFB laser performance.

The material gain and the detuning are given as follows:

$$g(z,t)=\frac{\Gamma a_N(N(z,t)-N_0)}{1+\varepsilon P_d} \quad (5.3)$$

$$\delta(z,t)=-\left(\frac{\lambda}{2\pi}\right)\alpha_H a_N(N(z,t)-N_0) \quad (5.4)$$

where Γ is the active layer confinement factor, a_N is the differential field gain, N is the carrier density, N_0 is the carrier density at transparency, ε is the nonlinear gain suppression coefficient, λ is the lasing wavelength, α_H is the linewidth enhancement factor, and P_d is the photon density given by the normalized power ($|F(z,t)|^2+|B(z,t)|^2$). The following carrier rate equation has been used to model the carrier density space and time dynamics along the laser cavity.

$$\frac{dN(z,t)}{dt}=\frac{J(z,t)}{ed}-\frac{N(z,t)}{\tau}-v_g g(z,t)P_d(z,t) \quad (5.5)$$

where $J(z,t)$ is the injected current density, d is the active layer thickness, e is the electronic charge, and τ is the carrier life time, which is given by:

$$\tau = \left\{A_r + B_r N(z,t) + C_r N(z,t)^2\right\}^{-1} \tag{5.6}$$

where A_r is the non-radiative recombination rate, B_r is the bimolecular carrier recombination coefficient, and C_r is the Auger carrier recombination coefficient.

Equations (5.2)-(5.6) are solved in self-consisting manner. The coupled-wave equations (5.2) can be written based on the traveling-wave approach (Li *et al.*, 2000) as follows[6]:

$$\begin{aligned}\begin{bmatrix} F(z+\Delta z, t+\Delta t) \\ B(z-\Delta z, t+\Delta t) \end{bmatrix} = \\ \exp\left[\Delta z(g - i\delta - \alpha_s)\right] \times \begin{bmatrix} e^{-i\Delta z\varsigma_1} F(z,t) \\ e^{-i\Delta z\varsigma_3} B(z,t) \end{bmatrix} + i\kappa p \Delta z \begin{bmatrix} B(z,t) \\ F(z,t) \end{bmatrix} \\ + i\Delta z \begin{bmatrix} \varsigma_2 B(z,t) \\ \varsigma_4 F(z,t) \end{bmatrix} + \Delta z \begin{bmatrix} Spn_f \\ Spn_r \end{bmatrix}\end{aligned} \tag{5.7}$$

The terms Spn_f and Spn_r describe the spontaneous noises associated with the forward and backward traveling fields, respectively. The spontaneous noise terms used in our numerical simulations are assumed to be generated from a Gaussian distributed random number generator satisfying the following correlation (Marcenac and Carroll, 1993):

$$\begin{cases} \left\langle Spn(z,t) Spn^*(z',t) = \beta_s K T_{sp} \delta(t-t') \delta(z-z')/v_g \right\rangle, \\ \left\langle Spn(z,t) Spn(z',t) \right\rangle = 0 \end{cases} \tag{5.8}$$

where $Spn(z,t) = Spn_f(z,t) = Spn_r(z,t)$ (Petermann *et al.*, 1979), β_s is the spontaneous coupling factor, K is the transverse Peterman factor, and $T_{sp} = B_r N^2/L$ (L cavity length) is the bimolecular recombination per unit length that contributes to the spontaneous emission.

Coupling Considerations

The coupling coefficient, which is related to the overlap integral of the two contra-propagating wave fields and Fourier coefficient of the gratings (Streifer

[6] The reader can get more details about the traveling-wave approach by consulting these two references: (Li, 2009) and (Li *et al.*, 2014).

et al., 1977), can be calculated by:

$$\kappa_p = \frac{k_0^2}{2\beta_0 P}\iint_G A_p(x,y)\Psi_0^2(x,y)dxdy \tag{5.9}$$

where k_0 is the free-space wavenumber, P is the fundamental mode optical power and Ψ_0 is the fundamental quasi-TE mode. A_p (x, y) defines the gratings Fourier coefficients, which are dependent of the grating shape. In this study, we only consider rectangular gratings whose Fourier coefficient can be defined for p = -N (N is the order gratings) as (Streifer *et al.*, 1976):

$$A_m = \begin{cases} -\dfrac{{n_2}^2 - {n_1}^2}{m}\sin(\pi m\gamma), & (x,y) \in G \\ 0, & elsewhere \end{cases} \tag{5.10}$$

We define G as the two-dimensional gratings region with respect to the transverse cross-section. The longitudinally alternating refractive indices are defined by n_1 (for the dielectric) and n_2 (considered as an average refractive index for the grating region layers). γ is the duty cycle for the laterally-coupled gratings defined as (σ/Λ) - as shown in Fig.5. 1 - the ratio of the wide ridge length (σ) over the grating period (Λ).

The coupling coefficient κ_p is modified when considering higher-order gratings through the Streifer terms (introduced earlier in (5.2)), which induces an effective coupling coefficient defined as:

$$\kappa_{\text{eff}} = \left\{(\kappa^*_p + \varsigma_2)(\kappa_p + \varsigma_4)\right\}^{1/2} \tag{5.11}$$

The coefficients ς_2 and ς_4 act as correction terms to the actual coupling coefficient. They arise from the coupling of partial waves generated by the forward to the backward propagating mode. As seen from (5.9) and (5.10), κ_{eff} strongly depends on the duty cycle and the Streifer coefficients.

In order to calculate κ_{eff}, the fundamental quasi-TE mode of the waveguide cross-section is solved. The fundamental mode solution Ψ_0(x,y) is used to calculate the partial wave solutions, which in turn are used to determine the

Streifer coefficients (Millet *et al.*, 2008a). We used Comsol Multiphysics (Comsol, 2007) – a commercial finite-element analysis software package – to assess and calculate the fundamental mode and partial wave fields.

5.3. Numerical results

The designs we have studied in this paper are $\lambda/4$-phase-shift LC-DFB lasers with first-, second-, third- and fourth-order gratings; assuming that both facets are perfectly antireflection-coated (AR). The parameters used in our model are listed in Table5. 1. In the following simulations, the laser cavity length is fixed at 400 μm. The cavity is split into 40 sections of equal lengths where the material and structure parameters are taken as constants. We have chosen this number of sections given that it allows a good compromise between accuracy and calculation CPU time. Additional sections do not really provide a significant improvement with respect to accuracy.

Table5. 1. Parameters used in our model

Symbol	Parameters	Values
	Bragg order	1- 4
W	Active region width (μm)	3.5
d	Active layer thickness (μm)	0.5
Γ	Confinement factor	0.3
n_{eff}	Effective phase refractive index	3.3
n_{g}	Effective group refractive index	3.7
α_{s}	Waveguide scattering and absorption loss (cm^{-1})	40
g_{N}	Differential gain ($10^{16} cm^{-2}$)	3
N_0	Transparent carrier density (10^{18} cm^{-3})	1.5
ε	Non-linear gain saturation coefficient (10^{-17} cm^3)	3
α_{H}	Linewidth enhancement factor	4.86
β_{s}	Spontaneous coupling factor (10^{-4})	1
A_r	Non-radiative recombination rate (10^{-9} s^{-1})	1
B_{r}	Bimolecular radiation coefficient (10^{-10} $cm^2 s^{-1}$)	1
C_{r}	Auger radiation coefficient (10^{-29} $cm^6 s^{-1}$)	3
λ	Wavelength (nm)	1550
K	Petermann factor (K)	1

The longitudinal carrier diffusion is ignored since the separation between sections is much longer than the diffusion length. All LC-DFB lasers considered

are used under the same driving condition. And we let all models run for a sufficiently long time under the same bias current to reach their respective steady states. The $\lambda/4$ phase-shift is placed at the center of the gratings and it can be introduced along the longitudinal direction of the waveguide through the phase adjustment region (Sode *et al.*, 1987; Kinoshita *et al.*, 1991).

Duty cycles considered here are extracted from simulations described above. For each gratings-order, the corresponding duty cycles chosen leads to maximum magnitudes of the coupling coefficient. For LC-DFB laser, a stable value of the effective coupling coefficient occurs at such peak points, producing a stable threshold gain and thus a stable wavelength operation. An effective coupling coefficient that is tolerant to small variations in grating geometry will not only produce a more reliable laser, but will also be tolerant to processing variations, producing a superior manufacturing yield.

First-order gratings

We start by investigating the standard case in which first-order gratings $\lambda/4$ phase-shift LC-DFB laser is considered. As explained in section 5.2, the coupling coefficient depends on grating duty cycle. We consider $\lambda/4$ phase-shift gratings with $\kappa_p L$= 1.6, 2.4, and 4.4, which correspond to duty cycles of 0.2, 0.3, and 0.78 respectively. The maximum magnitude for the coupling coefficients for the first order-gratings has a single peak at a duty cycle of 0.78. Duty cycles values greater than 0.3 will provide the same behaviour as 0.78, with the only noticeable difference being observed within the SMSR amount. Fig.5. 2 shows the longitudinal carrier distribution for first-order LC-DFB laser. For $\kappa_p L$ = 4.4, the LSHB is strong around the phase-shift region; however, for $\kappa_p L$=1.6, the longitudinal carrier distribution displays less non-uniformity and in particular it seems tending towards the same amount for both phase-shift and near the facets region.

The severe LSHB at the phase-shift region, as noticed in Fig.5. 2, favours the onset of longitudinal side modes, particularly at large $\kappa_p L$ values (>2). As shown

in Fig.5. 3, the excitation of the longitudinal side mode is caused by the non-uniform distribution of carrier density. It is difficult to give an analytical analysis that explains the above phenomenon. However, by analogy with standard DFB laser, the physics can be understood by studying numerically the interference between the forward (*F*) and backward (*B*) waves in the grating structure as explained by previous authors (Henry *et al.*, 1985). For AR-coated $\lambda/4$ phase-shift LC-DFB lasers, the interference between the *F* and *B* waves at the ends of the cavity is expected to be small; whereas, strong interference is expected around the phase shift region where both *F* and *B* have their maxima.

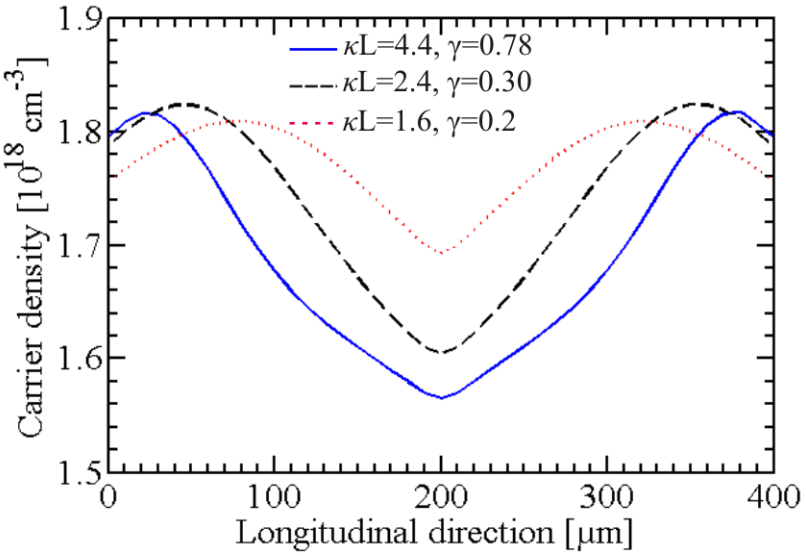

Fig.5. 2. Steady state longitudinal average carrier concentration profile for 1st-order gratings LC-DFB laser with $\kappa_p L$=1.6 (dotted line), $\kappa_p L$ =2.4 (dashed line), and $\kappa_p L$=4.4 (solid line) after 3.5 ns.

Fig.5. 3 shows the steady-state optical spectra corresponding to LC-DFB lasers with first-order gratings. For a normalized coupling coefficient $\kappa_p L$=4.4, dual-mode operation is observed, as shown in Fig.5. 3. Mode beating observed in Fig.5. 3 is induced by the excitation of longitudinal side mode which is confirmed by the strong LSHB observed along the active region as shown in Fig.5. 2. The occurrence of this side mode results in a poor SMSR. Severe hole-burning, when high $\kappa_p L$ devices are used, is believed to be the cause of this poor SMSR (Streifer *et al.*, 1976). However, this beating can be removed and single mode operation is

observed when $\kappa_p L$ is decreased ($\kappa_p L$ =1.6 and 2.4). For devices with $\kappa_p L$> 2.4, the steady state responses are similar to the case of $\kappa_p L$= 2.4 except the mode beating which will be enhanced with increasing $\kappa_p L$ values.

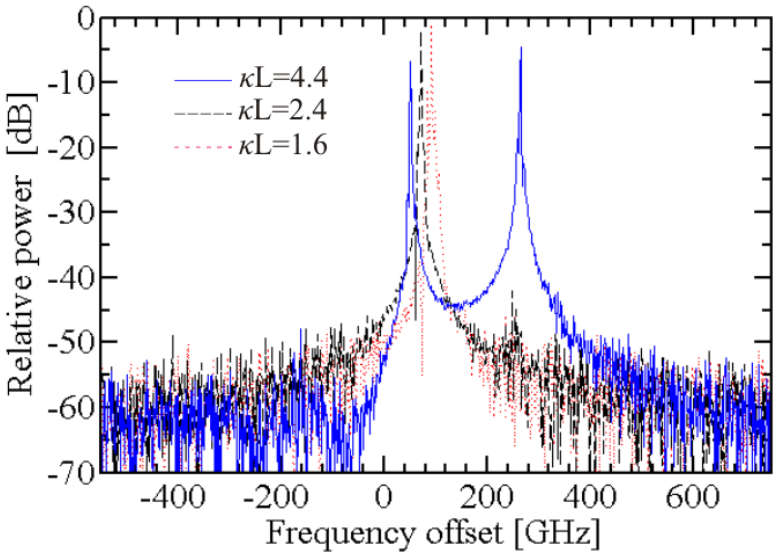

Fig.5. 3. Steady-state spectra after 3.5 ns for 1st-order gratings LC-DFB laser with $\kappa_p L$= 1.6, γ=0.2 (dotted line), $\kappa_p L$=2.4, γ=0.3 (dashed line), and $\kappa_p L$=4.4, γ=0.78 (solid line).

High-order gratings

Second-, third- and fourth-order gratings have also been numerically investigated. For these grating-structures, the effective coupling coefficient κ_{eff} becomes complex as a result of the introduction of Streifer coefficients. As mentioned earlier, κ_{eff} strongly depends on the duty cycle (Millet *et al.*, 2010). In our analysis, we select the duty cycles that provide the local maximum magnitude of the effective coupling coefficient (Millet *et al.*, 2008a).

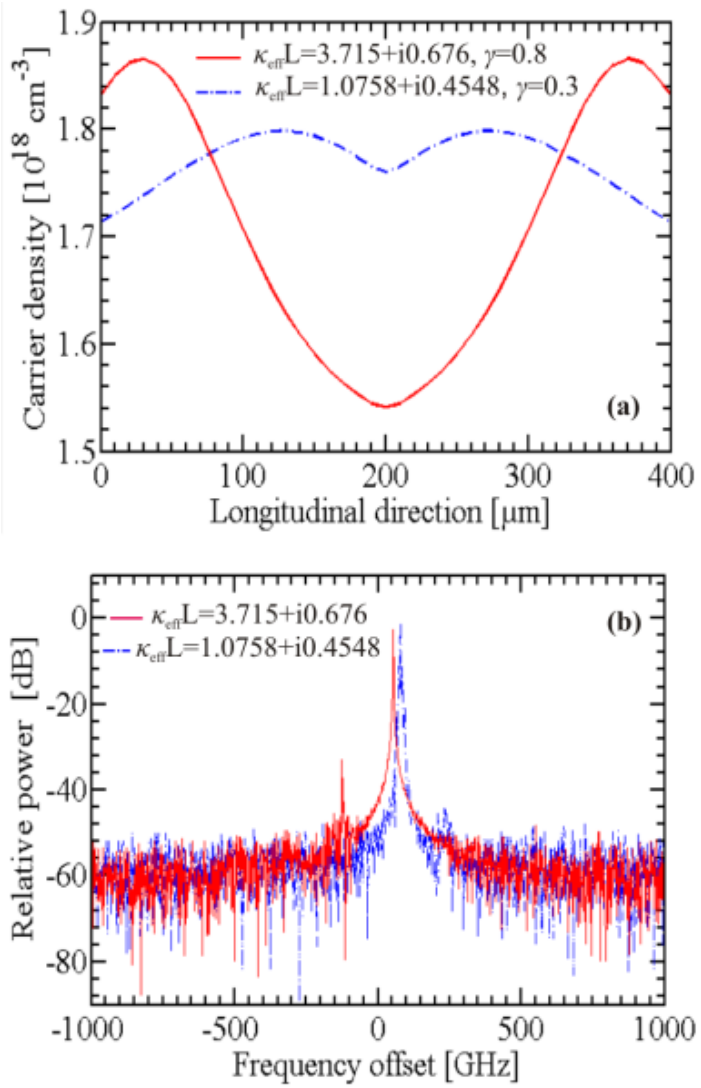

Fig.5. 4. (a) Longitudinal carrier distribution profile for 2nd-order LC-DFB laser with $\kappa_{eff}L$=1.0758 - 0.4548i, γ=0.3 (dashed-dot line) and $\kappa_{eff}L$=3.7150 + 0.6760i, γ=0.8 (solid line). (b) The corresponding steady-state spectra.

Fig.5. 4(a) shows the longitudinal carrier distribution for second-order gratings for $\kappa_{eff}L$ = 1.0758 - 0.4548i and 3.7150 + 0.6760i, corresponding to 30% and 80 % duty cycles, respectively. The longitudinal carrier distribution is relatively uniform for the former case; whereas, severe LSHB is exhibited in the phase-shift region for the latter case. This carrier distribution non-uniformity is believed to be the origin of the side mode occurrence and will result in poor SMSR as shown in Fig.5. 4(b) (where we show the steady state spectra for second-order gratings for duty cycles of 0.3 and 0.8). For a duty cycle ~ 0.8, the side mode is

much lower when using second-order gratings. This is in complete agreement with previous theoretical studies (Kazarinov et al., 1985) where mode discrimination has been achieved using DFB lasers with second-order gratings taking into account the effect of radiation losses.

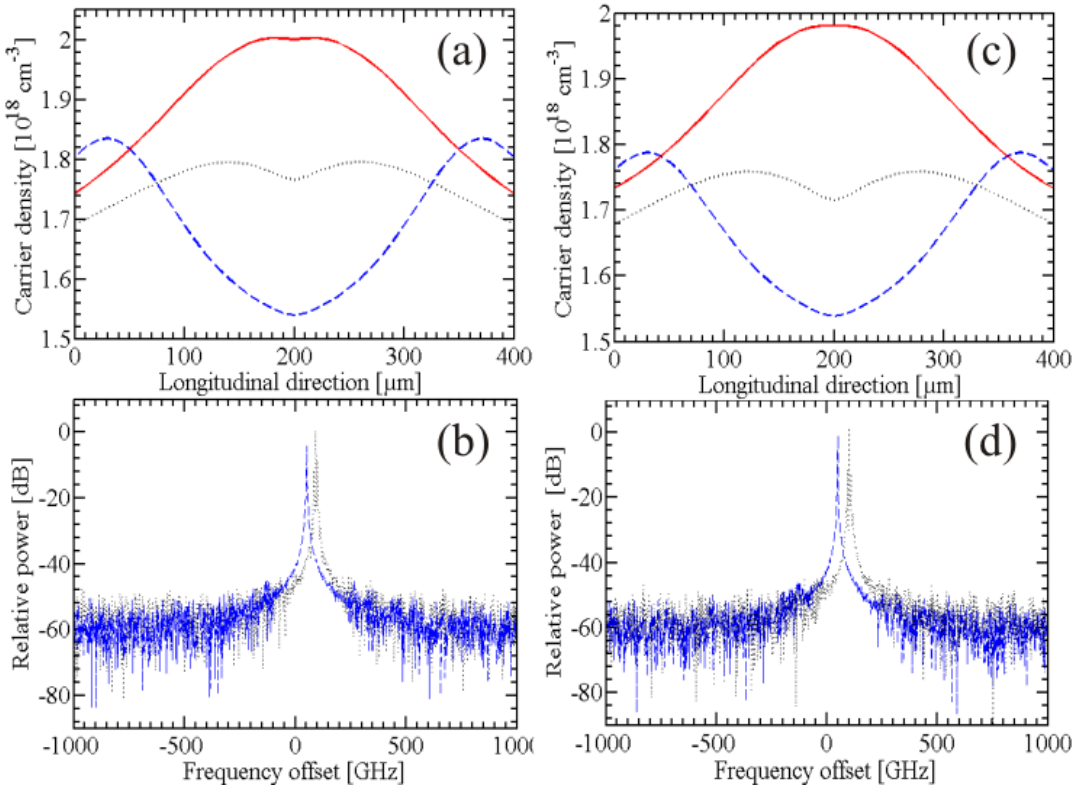

Fig.5. 5. (a) Longitudinal carrier distribution for 3rd-order LC-DFB laser with (*i*) $\kappa_{eff}L$=0.5752 + 0.1970i, γ=0.15 (solid line), (*ii*) $\kappa_{eff}L$=1.0325 - 0.1245i, γ=0.5 (dotted line), and (*iii*) $\kappa_{eff}L$=3.6059 + 0.4348i, γ=0.85 (dashed line). (b) The corresponding steady state spectra for the cases (*ii*) and (*iii*) after 3.5 ns. (c)Longitudinal carrier distribution for 4th-order LC-DFB laser with (*i*) $\kappa_{eff}L$=0.3262 - 0.6103i, γ=0.15 (solid line), (*ii*) $\kappa_{eff}L$=1.14865+0.2328i, γ=0.6 (dotted line), and (*iii*) $\kappa_{eff}L$=3.3566 + 0.5417i, γ=0.9 (dashed line). (d) The corresponding steady state spectra for the cases (*ii*) and (*iii*) after 3.5 ns.

We have similarly investigated on the third- and fourth-order gratings. Fig.5. 5 shows the longitudinal carrier distribution for third-order LC-DFB laser with three different coupling coefficients. As we can see the steady-state longitudinal spatial hole burning is less severe than the case for LC-DFB lasers with high-order grating, especially when the duty cycle is tailored to optimal value as

shown in Fig.5. 5 (a) and (c). For the sake of clarity, we only report steady-state spectra corresponding to optimal and maximum coupling coefficients for both third- and fourth- order gratings. As we increase the grating-order, the LSHB becomes weaker especially in the phase-shift region. However, the duty cycle must be carefully chosen. Radiation loss beneficial effect of high order-grating is advanced here since both steady state optical spectra display stable single mode-operation.

Longitudinal spatial hole burning

The mechanism of LSHB has been described in some detail in the literature (Whiteaway *et al.*, 1989; Morthier *et al.*, 1990; Rabinovich *et al.*, 1989) for standards DFB lasers. Stimulated recombination is believed to be the main origin of LSHB, and creation of non-uniformities in the carriers and photon densities along the cavity propagation direction. In the same manner, it can be described for LC-DFB lasers to be nonlinearity in devices performance that depends on the stimulated emission rate in the active region. The effects of spatial hole-burning in DFB lasers, in general, and LC-DFB lasers, in particular, are more important than those in Fabry-Perot lasers. Variations in the carrier density and, hence, variations in the real refractive index and gain give rise to changes in the magnitude and phase of the feedback from each section of the grating. If the longitudinal mode intensity distribution is nonuniform, then, as the photon density rises, the injected carrier density hole burns and an associated longitudinal non-uniformity, in the effective refractive index and gain of the mode, develops. All this changes the longitudinal-mode intensity distribution and also alters the gain suppression of side modes relative to the lasing mode. Then, the resulting lasing mode will exhibit, under static conditions, a nonlinear light-current characteristic and electronic wavelength chirp with increasing output power. The chirp has two contributions: first, is the associated change in the effective magnitude of the phase shift and, second, is the allied change in the mean carrier density perceived by the mode. In addition,

the side mode suppression ratio can decrease with output power, leading eventually to multiple mode operation. In general, avoiding LSHB leads to more uniform carrier distribution and uniform complex refractive index, giving more effective utilisation of the gain and a narrower linewidth.

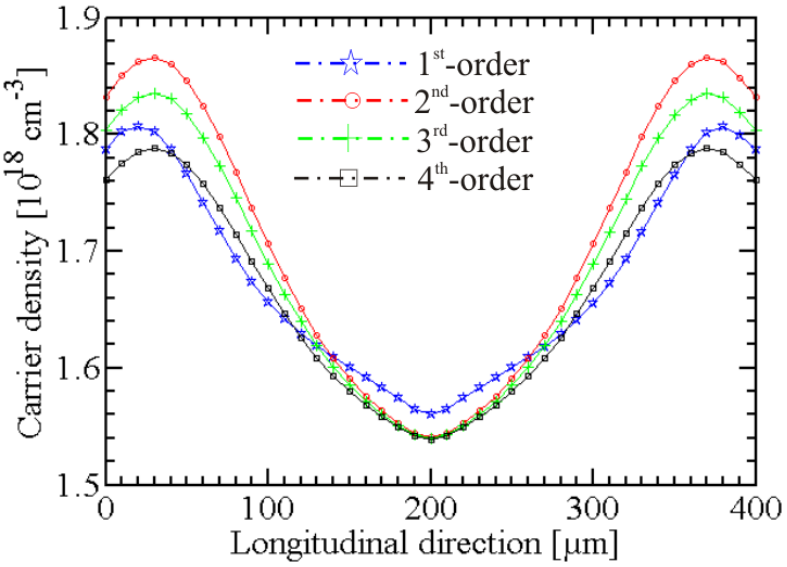

Fig.5. 6. The steady state carrier concentration distribution for 1st- to 4th-order gratings for duty cycles of 0.78, 0.8, 0.85, and 0.9 respectively.

Fig.5. 6 shows a strong non-uniformity of the carrier density distribution for first-, second-, third-, and fourth-order gratings. However, the high order structures display a much more uniform longitudinal mode carrier distribution than the standard one if the duty cycle is very well tailored as shown in Fig.5. 7.

The above simulation suggests that the duty cycle is a key parameter in the design of a LC- DFB laser. It has a significant impact on the longitudinal carrier distribution. For this reason, it is optimal that the duty cycle be chosen to tailor coupling coefficients to optimal values. For a rectangular grating shape, as illustrated in Fig.5. 1, if one designs the first-order grating structure such that $\gamma=\sigma/\Lambda\leq 0.3$, then a single mode operation with high SMSR (>40 dB) will be achieved according to the simulation. This very small value of duty cycle will result in very thin grating teeth, which will complicate fabrication process. For second-order grating cases, LSHB is less severe. However, the side mode can be

clearly seen. Our simulations show that this side mode can be removed when using a duty cycle less than 0.3 and, hence, a high SMSR ratio of 46 dB would be achieved. Third- and fourth-gratings orders exhibit a single-mode operation but carrier distribution will be more uniform if respective duty cycles are carefully chosen. This will result in a lasing mode with less frequency shift or chirp.

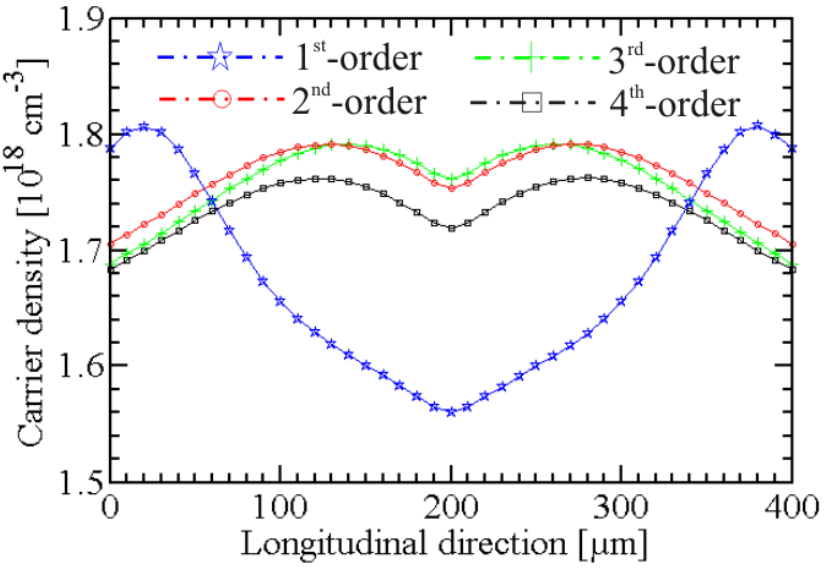

Fig.5. 7. The steady state carrier concentration distribution for 1st- to 4th-order gratings for duty cycles of 0.78, 0.3, 0.5, and 0.6 respectively

Moreover, a remarkably enhanced SMSR, as high as 45 dB, can be predicted for third-order gratings according to our simulations. This result is in quasi agreement with recent published experimental work for third-order LC-DFB (Telkkala *et al.*, 2011). Corresponding duty cycle is found to be around 0.5 which provides more ease for fabrication of those structures, as compared to first- and second-order grating with duty cycle less than 0.3. LSHB seems to be similar for third- and fourth-order LC-DFB. However, taking into account that radiation loss will be more important when increasing the grating order, third-order LC-DFB lasers will be preferred to the fourth-order based structure.

5.4. Conclusion

We have numerically studied the effect of high-order grating on the transient response performance of LC-DFB lasers. A time-domain modified coupled mode

approach has been applied to LC-DFB, with the coupled-mode coefficients calculated for the two-dimensional waveguide cross-section using the finite-element method. This approach advances the impact of radiating partial waves on our higher-order gratings. It is found that the duty cycle is of critical importance since the LSHB and SMSR vary significantly depending on the duty cycle chosen and the grating-order. Duty cycle values for rectangular gratings that yield lasers with stable wavelengths and high SMSR were calculated for first-, second-, third-, and fourth-order gratings. Our results indicate that, while the radiating partial waves of higher order gratings will, in general, result in higher threshold gains, as compared to first-order gratings; higher order gratings exhibit improved LSHB and SMSR. Threshold gain, which in general will be more important for high order-grating, is another important optical parameter to be considered in our future investigations.

Chapter 6 | Conclusions

Summary and Conclusions

The major subjects of this thesis were: First, to experimentally characterize semiconductor corrugated ridge waveguide DFB lasers at different wavelength windows; Second, to propose a dynamical time-domain model capable of simulating these laser structures.

A dedicated, flexible, and automated experimental test bench has been built to facilitate the test and measurement of CRW-DFB lasers with high-order gratings. First we started by characterizing 1310 nm CRW-DFB lasers as a local oscillator for optical coherent receivers. We presented the design and experimental results for these devices, which have been fabricated successfully using stepper lithography despite some fabrication variations. Indeed, stable single-mode operation with high side mode suppression ratios (SMSRs) ≥ 50 dB, a temperature-dependent wavelength shift $d\lambda/dT$ ~ 0.06 nm/C, an average output power ≥ 9 mW, an average threshold of 86 mA have been obtained at 25°C, an average slope efficiency of 0.096 mW/mA, an average series resistance ≤ 10 Ω, and an estimated coupling $|\kappa_{eff}|$=12.5 cm^{-1} (normalized coupling $|\kappa_{eff}|L$=1.25), for 1000 µm-long devices with 0.5 duty cycle 3rd-order gratings.

We then presented the experimental results of the previous model that has been developed to migrate towards 1550 nm CRW-DFB lasers. Stable single-mode operation with SMSRs exceeding 50 dB, a temperature-dependent wavelength shift $d\lambda/dT$ ~ 0.09 nm/°C, a wavelength tuning of ~ 2 nm, average output powers ≥ 7mW, average threshold currents of 74 mA at 25°C, an average slope efficiency of 0.03, an average series resistance ≤ 6 Ω, and an estimated coupling $|\kappa_{eff}|$=10 cm^{-1} (normalized coupling $|\kappa_{eff}|L$=1.5), for 1500 µm-long devices with 0.55 duty cycle 3rd-order gratings have been recorded. In addition,

linewidth determination has been carried using the delayed self-heterodyne interferometric technique. Narrow linewidths (≤ 250 kHz) have been observed for a wide range of current injection. This makes this kind of laser a potential candidate for new advanced coherent communications.

We next investigated and compared CRW-DFB lasers with different multi-electrode configurations. The concept of multi-electrode current injection allows an artificial control of the carrier density along the laser cavity by tailoring the current injection via different electrically isolated sections. We showed how this concept has been applied to CRW-DFB lasers designs of different structures than the laser described herein. To the authors' best knowledge, this structure is novel and contributes to the advancement of the field by offering other rooms for design and performance improvements for CRW-DFB lasers. In particular we presented results on two-electrode CRW-DFB lasers, which oscillate in single-mode around 1560 nm with high side mode suppression ratios (> 54 dB), a wavelength tuning (≥ 3nm), an output power > 6 mW, average threshold currents of 70 mA at 25°C, and narrow linewidth < 170 kHz under various current injection ranges at room temperature. A minimum linewidth of 94 kHz has been recorded for 1500 μm-long two-electrode CRW-DFB laser while providing non-uniform current injection through the two electrodes. We have also studied the effect of the width of the inter-electrode gap on these different performance measures. This allows the selection of optimum inter-electrode gaps. We afterwards studied three-electrode CRW-DFB lasers, which also oscillated at 1560 nm with stable single mode operation (SMSR ≥ 50 dB), output powers ≥ 7 mW, and wavelength tuning range ≥ 2.3 nm, average threshold currents of 66 mA at 25°C, and narrow linewidths (≤ 140 kHz) with minimum of 70 kHz. The effect of electrode partition on device performances has been also studied.

We then presented an application of a time-domain traveling wave model for the simulation of CRW-DFB lasers. The model is based on time-dependent

modified coupled-wave equations that consider among many parameters the radiation modes, which are particularly experienced in CRW-DFB lasers with high-order gratings. We showed by means of numerical analysis how the degree of longitudinal spatial hole burning (LSHB) can be effectively reduced through optimum duty cycle and gratings orders selection. The model also allows for side mode suppression ratios (SMSR). In general, we demonstrated how we can get benefits in terms of reducing the LSHB and improving SMSR by considering high-order gratings for CRW-DFB lasers.

The experimental investigation in this thesis has shown that semiconductor CRW-DFB laser can be considered as a potential candidate for many applications. In particular, the narrow linewidth feature makes these lasers very attractive as transmitters or local oscillators for advanced optical coherent communications using high-order modulation formats (Seimetz, 2008; Seimetz, 2009; Pfau *et al.*, 2009). Moreover, the re-growth free approach in this device fabrication allows a monolithic integration with other opto-electronics devices. It can actually extremely valuable for photonics chip-scale integration applications. For instance, Tolstikhin *et al.* has shown an attractive application of CRW-DFB lasers that can be integrated into transceivers for fiber-optics communications (Tolstikhin *et al.*, 2009a-b). Other applications could involve the integration of multiple CRW-DFB laser sources with semiconductor optical amplifiers, MMI couplers, and electro-absorption modulators to produce a coarse wavelength division multiplexing (CWDM) sources (Hou *et al.*, 2011; Hongliang *et al.*, 2013; Liu *et al.*, 2014). These applications show that – in addition to the integrability feature of CRW-DFB lasers – the use of photolithography techniques such as stepper lithography will open the doors for low-cost mass-production laser sources, which pave the way toward affordable photonics integrated circuits (Nagarajan *et al.*, 2005). Recently, there have an attractive demonstration on how these structures allow new hybrid integration of III-V materials on silicon to make hybrid III-V/silicon lasers (Cao *et al.*, 2015). Other

recent work showed also that these devices can be applied into other areas such as atmospheric gas detection (Briggs *et al.*, 2013). The author believes that with a further design optimization, with particular regard to the epitaxy engineering, the devices characterized in this thesis could potentially lead to a wide deployment in photonics integrated circuits.

Prospective work

From the material presented in this thesis, several research directions and suggestions could be derived. We propose some directions for future research investigations, which are indispensable for not only further advanced device characterization but also for design improvement.

An important key parameter in laser performance is the threshold current, which has a direct impact on the power consumption. The measured threshold in this thesis for different CRW-DFB lasers was higher than anticipated. Although, preliminary reasons that could be potentially behind this observation were discussed in Chapters 3 and 4, the observed spectral mismatch between the resonance wavelength and the gain peak wavelength could perhaps be the most attractive argument behind the high threshold values. We should also emphasize that the observed mismatch between the gain peak and the gratings' operating wavelength is non-intentional, since the aim of this work was to design a 1550 nm CRW-DFB laser. We believe that such spectral offset could be ascribed to two main causes:

- Inherent Las2D software limitations: we want to emphasize on the fact that Las2D does not support lattice-matched barriers to the InP substrate. Alone, the latter limitation affects the electronic structure of the active material. It shifts the conduction and valence eigenenergy levels in opposite directions in such a way that the effective (engineered) bandgap energy shoots up by an order of a meV.

- Molar composition calibrations carried out by the epitaxial growers: the epitaxial layer requisition submitted for growth prescribes the required strain levels in each layer. Unfortunately, the growth mechanism does not allow for strain as a degree of freedom. Rather, the growers carry out several calibrations to the molar compositions as a figure of merit to induce the sought after emission wavelength. The latter process is spectral-error prone.

It is therefore important that a major revision must be undertaken for the epitaxial engineering with another advanced tool while taking into account these experimental results.

The measured maximum slope efficiency for our 1500 µm-long CRW-DFB lasers was 0.031 per facet, whereas counterpart FP devices that have fabricated in the same wafer as for the DFB lasers, the maximum slope efficiency was 0.053. The low slope efficiency could be explained in part by the low internal quantum efficiency of 48.73 % and the external differential quantum efficiency of 17.9 %. Besides, the estimated internal loss is ~ 11.6 cm^{-1} and the mirror loss is ~ 19.4 cm^{-1} suggesting a total optical loss of ~ 31 cm^{-1}. Compared to the simulation results (slope efficiencies ≥ 0.32 mW/mA and optical loss of ~ 9 cm^{-1} were expected), we see that there is large discrepancy, which suggests that a major source of optical loss or carrier recombination is not properly accounted for in the Las2D model. In one hand, it should be stated that this model used many parameters that were empirical and not calibrated by experimental data. On the other hand, in this model the losses due to metal contacts (Au/Pt/Ti in our case) are not calculated and are treated as ohmic contact boundaries in the electrical model. The 0.8 µm ridge height causes the fundamental mode to lift up near the lossy metal layers further requiring a higher threshold current. The limited resolution of stepper lithography requires the use of at least a third order grating which is conducive to the onset of radiation modes further exacerbating the loss in the cavity. Finally the fine features of the gratings' teeth display some

rounding (as can be seen by the SEM photos) therefore an additional scattering loss is to be accounted for. All of these observations suggest that major revision for the epitaxial design should be undertaken. This requires the use of other software plus a close collaboration with the grower. The rounding in the gratings may be overridden by seeking other low resolution lithography techniques, such as nanoimprint lithography.

As potential future advanced measurements, one should undertake frequency modulation (FM) response measurements. The frequency modulation (FM) response is a measure of the modulation efficiency and is obtained by directly modulating a CRW-DFB laser diode by superimposing a signal wave on the injected current. It is actually defined as the ratio of frequency deviation to injected current (Hz/mA) and it is modulation frequency dependent. These measurements should be done for single and multi-electrode CRW-DFB lasers. Although different approaches either based on Fabry-Perot interferometers, self-homodyning, or fiber dispersion (Morthier and Vankwikelberge, 1997) can be used for the FM response measurements, a special attention should be given to the mounting of the lasers particularly that high-frequency probes will be needed in these measurements. A flat response is expected for the latter devices as has been observed with the multi-electrode conventional DFB lasers. A flat response is highly desirable because it gives an idea on the modulation bandwidth of these lasers. In fact, it is known that in digital systems the modulation bandwidth should be large enough to accommodate for the bit rate to be transmitted. The higher the bit rate the larger should be the modulation bandwidth. For example, in order to transmit data at 10 Gbit/s at least 5 GHz of bandwidth is required if the non-return-to-zero (NRZ) binary format is considered. If the return-to-zero (RZ) format is considered then at least 10 GHz is required a modulation bandwidth. Subsequently, other measurements such as the bit error rate are also very desirable, where the lasers can be tested in real optical fiber-based transmission link.

To improve the time-domain model that was developed based on the travelling-wave approach, one can try to extend the current model to a quasi-three-dimensional model. In such model the longitudinal and lateral variation of the optical mode and carrier density profiles can be included. In addition, the built-in refractive index along the lateral direction, the change in refractive index induced by the carrier concentration, the lateral geometric parameters (such as the wide and narrow ridge widths in CRW-DFB lasers), the width of metal contact stripe, and the diffusion factor are all other parameters that can be included to enhance the model for better performance prediction. It is expected that such a quasi-three-dimensional model would allow analyzing both the lateral and longitudinal spatial hole burning effects on the dynamic responses of CRW-DFB lasers. It will also allow studying ridge waveguide design variations (such as phase-shift sections, tapered waveguide…) and their impact on the device performances.

Bibliography

Agrawal and Dutta, 1968: G. P. Agrawal, and N. K. Dutta, Long-Wavelength Semiconductor Lasers, New York: Van Nostrand, 1968.

Antreasyan and Wang, 1983: A. Antreasyan, and S. Wang, "Electronic wavelength tuning with semiconductor integrated etalon interference lasers," Applied Physics Letters, vol. 43, no. 6, pp. 530-532, Jun. 1983.

Briggs et al. 2012: R. M. Briggs, C. Frez, A. Ksendzov, K. J. Franz, M. Bagheri, and S. Forouhar, "Laterally coupled distributed-feedback GaSb-based diode lasers for atmospheric gas detection at 2 µm," in proceedings of Conference on Lasers and Electro-Optics (CLEO), San Jose, California, paper JTh1L, May 2012.

Briggs et al. 2013: R. Briggs, C. Frez, M. Bagheri, C. Borgentun, J. Gupta, M. Witinski, J. Anderson, and S. Forouhar, "Single-mode 2.65 µm InGaAsSb/AlInGaAsSb laterally coupled distributed-feedback diode lasers for atmospheric gas detection," Optics Express, vol. 2, no. 1, pp. 1317-1323, Jan. 2013.

Carroll et al., 1998: J. Carroll, J. Whiteaway, and D. Plumb, Distributed feedback semiconductor lasers, Institution of Electrical Engineers, 1998.

Casey and Panish, 1978: H. Casey and M. Panish, "Heterostructure Lasers", Academic Press, New York, 1978.

Cao et al., 2015: Y. Cao, X. Hu, X. Luo, J. Song, Y. Cheng, C. Li, C. Liu, H. Wang, L. Tsung-Yang, G. Lo, and Q. Wang, "Hybrid III-V/silicon laser with laterally coupled Bragg grating," Optics Express, vol. 23, no. 7, pp. 8800-8808, Mar. 2015.

Champagne et al., 1999: A. Champagne, R. Maciejko, D. Adams, G. Pakulski, B. Takasaki, and T. Makino, "Global and local effects in gain-coupled multiple quantum- well DFB lasers," IEEE Journal of Quantum Electronics, vol. 35, no. 10, pp. 1390–1401, Oct. 1999.

Chen, 2006: X. Chen, "Ultra-Narrow Laser Linewidth Measurement", PhD. dissertation, Dept. Elect. Eng., Virginia Polyt Inst. and State Univ., Blacksburg, Virginia, United States, 2006.

Chen et al., 2000: N. Chen, Y. Watanabe, K. Takei, and K. Chikuma, "InGaAsP/InP laterally coupled distributed feedback laser," Japanese Journal of Applied Physics, vol. 39, part. 1, no. 3B, pp. 1508-1511, Mar. 2000.

Choi et al., 1996: W.-Y. Choi, J.C. Chen, and C.G. Fonstad, "Evaluation of coupling coefficients for laterally-coupled distributed feedback lasers", Japanese Journal of Applied Physics, vol. 35, no. 9A, pp. 4654-4659, Sep. 1996.

Comsol, 2007: COMSOL Multiphysics 3.4 COMSOL Corporation, Burlington, MA, Oct. 2007

Das et al., 2004: P. K. Das, M. Uemukai, and T. Suhara, "InGaAs/AlGaAs quantum well laterally-coupled distributed feedback laser," Japanese Journal of Applied Physics, vol. 43, no. 5A, pp. 2549–2550, May 2004.

Dougherty et al., 1999: D. J. Dougherty, R. C. Guttierrez, S. Dubovitsky, and S. Forouhar, "Semiconductor Laser Linewidth measurements for space interferometry applications", Proc. SPIE 3626, Testing, Packaging, Reliability, and Applications of Semiconductor Lasers IV, pp. 115-122, Apr. 1999.

Dridi et al., 2014a: K. Dridi, A. Benhsaien, J. Zhang, and T. J. Hall, "Narrow Linewidth 1550 nm Corrugated Ridge Waveguide DFB Lasers," IEEE Photonics Technology Letters, vol. 26, no. 12, pp. 1192-1195, Jun. 2014.

Dridi et al., 2014b: K. Dridi, A. Benhsaien, J. Zhang, K. Hinzer, and T. J. Hall, "Narrow linewidth two-electrode 1560 nm laterally coupled distributed feedback lasers with third-order surface etched gratings," Optics Express, vol. 22, no. 16, pp. 19087-19097, Aug. 2014.

Dridi et al., 2010: Kais Dridi, Henry Schriemer, Karin Hinzer, and Trevor Hall, "On the performance of fabricated third order laterally coupling distributed feedback 1310nm lasers", Proc. SPIE 7750 775013 (2010).

Duan and Gallion: G. H. Duan, and P. Gallion, "Drive current noise induced linewidth in tunable multielectrode lasers", IEEE Photonics Technology Letters, vol. 3, no. 4, pp. 302-304, Apr. 1991.

Dumitrescu et al., 2011: M. Dumitrescu, J. Telkkälä, J. Karinen, J. Viheriälä, A. Laakso, S. Afzal, J. –P. Reithmaier, M. Kamp, P. Melanen, P. Uusimaa, P. Bardella, M. Vallone, I. Montrosset, O. Parillaud, M. Krakowski, D. Gready, G. Eisenstein, and G. Sek, "Development of high-speed directly modulated DFB and DBR lasers with surface gratings", Proc. SPIE 7953, Novel In-Plane Semiconductor Lasers X, 79530D (2011).

Eddolls et al., 1992: D. V. Eddolls, S. J. Vass, R. M. Ash, and C. A. Park, "Two-segment multiquantum well lasers with 7 nm tuning range and narrow linewidth," Electronics Letters , vol. 28, no. 11, pp. 1057-1058, May 1992.

Fang and Wang, 1984: Z. -J. Fang, and S. Wang, "Longitudinal mode behavior and tunability of separately pumped (GaAl)As lasers," Applied Physics Letters, vol. 44, no. 1, pp. 13-15, Jan. 1984.

Fish et al., 2011: F. A. Fish, D. Welch, R. Nagarajan, J. L. Pleumeekers, V. Lal, M. Ziari, A. Nilsson, M. Kato, S. Murthy, P. Evans, S. W. Corzine, M. Mitchell, P. Samra, M. Missey, S. DeMars, R. P. Schneider, M. S. Reffle, T. Butrie, J. T. Rahn, M. V. Leeuwen, J. W. Stewart, D. J. H. Lambert, R. C. Muthiah, H-S. Tsai, J. S. Bostak, A. Dentai, K-T. Wu, H. Sun, D. J. Pavinski, J. Zhang, J. Tang, J. McNicol, M. Kuntz, V. Dominic, B. D. Taylor, R. A. Salvatore, M. Fisher, A. Spannagel, E. Strzelecka, P. Studenkov, M. Raburn, W. Williams, D. Christini, K. J. Thomson, S. S. Agashe, R. Malendevich, G. Goldfarb, S. Melle, C. Joyner, M. Kaufman, and S. G. Grubb, "Current Status of Large-Scale InP Photonic Integrated Circuits," IEEE Journal of Selected Topics in Quantum Electronics, vol. 17, no. 6, pp. 1470-1489, Nov.-Dec. 2011.

Forouhar et al., 2012: S. Forouhar, R. M. Briggs, C. Frez, K. J. Franz, and A. Ksendzov, "High-power laterally coupled distributed-feedback GaSb-based diode lasers at 2 μm wavelength," Applied Physics Letters, vol. 100, no. 3, pp. 031107-1-031107-4, Jan. 2012.

Fukuda et al., 1989: M. Fukuda, K. Sato, Y. Kondo, and M. Nakao, "Continuously tunable thin active layer and multisession DFB laser with narrow linewidth and high power," Journal of Lightwave Technology, vol. 7, no. 10, pp. 1504-1509, Oct.1989.

Funabashi et al., 2004: M. Funabashi, H. Nasu, T. Mukaihara, T. Kimoto, T. Shinagawa, T. Kise, K. Takaki, T. Takagi, M. Oike, T. Nomura, and A. Kasukawa, "Recent advances in DFB lasers for ultradense WDM applications," IEEE Journal of Selected Topics in Quantum Electronics, vol. 10, no. 2, pp. 312-320, Mar-Apr. 2004.

Golka et al., 2005: S. Golka, C. Pflugl, W. Schrenk, and G. Strasser, "Quantum cascade lasers with lateral double-sided distributed feedback grating," Applied Physics Letters, vol. 86, no. 11, pp. 111103-1-111103-3, Mar. 2005

Hakki and Paoli, 1975: Hakki, B.W., and Paoli, T., "Gain spectra in GaAs double heterostructure injection lasers," Journal of Applied Physics, vol. 46, no. 3, pp. 1299-1306, Mar. 1975.

Haring et al., 2010: K. Haring, J. Viheriala, M. –R. Viljanen, J. Paajaste, R. Koskinen, S. Suomalainen, A. Laakso, K. Leinonen, T. Niemi, and M. Guina, "Laterally-coupled

distributed feedback InGaSb/GaSb diode lasers fabricated by nanoimprint lithography," Electronics Letters, vol. 46, no. 16, pp. 1146-1147, Aug. 2010.

Henry et al., 1985: C. H. Henry, R. F. Kazarinov, R. A. Logan, and R. Yen, "Observation of destructive interference in the radiation loss of second-order distributed feedback lasers," IEEEJ. Quantum Electronics, vol. 21, no. 2, pp. 151-154, Feb. 1985.

Hou et al. 2012: L. Hou, M. Haji, J. Akbar, and J. Marsh, "Narrow linewidth laterally coupled 1.55 μm AlGaInAs/InP distributed feedback lasers integrated with a curved tapered semiconductor optical amplifier," Optics Letters, vol. 37, no. 21, pp. 4525-4527, Nov. 2012.

Hou et al., 2011: L. Hou, M. Haji, J. Akbar, J. Marsh, and A. Bryce, "CWDM source based on AlGaInAs/InP monolithically integrated DFB laser array," Optics Letters, vol. 36, no. 21, pp. 4188-4190, Nov. 2011.

Hongliang et al., 2013: Z. HongLiang; M. Li; L. Song; Z. Can; W. BaoJun; Z. LingJuan, and W. Wei, "InP based DFB laser array integrated with MMI coupler," Science China Technological Sciences, vol. 56, no. 3, pp. 573-578, Mar. 2013.

Kaiser et al., 2005a: W. Kaiser, K. Mathwig, S. Deubert, J. –P. Reithmaier, A. Forchel, O. Parillaud, M. Krakowski, D. Hadass, V. Mikhelashvili, and G. Eisenstein, "Static and dynamic properties of laterally coupled DFB lasers based on InAs/InP QDash structures," Electronics Letters , vol. 41, no. 14, pp. 808-810, Jul. 2005.

Kaiser et al., 2005b: W. Kaiser, K. Mathwig, S. Deubert, A. Somers, A. Forchel, J. –P. Reithmaier, O. Parillaud, M. Krakowski, D. Hadass, V. Mikhelashvili, G. Eisenstein, and M. Legge, "Laterally coupled DFB lasers based on InAs/InP-Qdash structures for broadband applications," in proceedings of the 31st European Conference on Optical Communication, (ECOC), paper We4.P.029, Glasgow, UK, Sep. 2005.

Kamp et al., 1999: M. Kamp, J. Hofmann, A. Forchel, F. Schafer, and J. -P Reithmaier, "Low-threshold high-quantum-efficiency laterally gain-coupled InGaAs/AlGaAs distributed feedback lasers," Applied Physics Letters, vol. 74, no. 4, pp. 483-485, Jan. 1999.

Kamp et al., 1998: M. Kamp, J. Hofmann, A. Forchel, F. Schafer, and J. –P. Reithmaier, "High performance laterally gain coupled InGaAs/AlGaAs DFB lasers," in proceedings of the International Conference on Indium Phosphide and Related Materials, paper FA3-3, Tsukuba, Japan, May 1998.

Kazarinov et al., 1985: R. Kazarinov and C. Henry, "Second-order distributed feedback lasers with mode selection provided by first-order radiation losses," IEEE Journal of Quantum Electronics, vol. 21, no. 2, pp. 144–150, Feb. 1985.

Kinoshita et al., 1991: J. Kinoshita, K. Ohtsuka, H. Agatsuma, A. Tanaka, T. Matsuyama, A. Makuta, and H. Kobayashi, "Performance of 1.5 pm DFB lasers with a narrow stripe region," IEEE Journal of Quantum Electronics, vol. 27, no. 6, pp.1759-1765, Jun. 1991

Konig et al., 1999: H. Konig, S. Rennon, J. –P. Reithmaier, A. Forchel, J. –L. Gentner, and L. Goldstein, "1.55 μm single mode lasers with complex coupled distributed feedback gratings fabricated by focused ion beam implantation," Applied Physics Letters, vol. 75, no. 11, pp. 1491-1493, Sep. 1999.

Kotaki et al., 1989: Y. Kotaki, S. Ogita, M. Matsude, Y. Kuwahara, and H. Ishikawa, "Tunable, narrow-linewidth and high-power λ/4-shifted DFB laser," Electronics Letters, vol.25, no. 15, pp. 990-992, Jul. 1989.

Kuo and Dutta, 1988: C. Y. Kuo, and N. K. Dutta, "Characteristics of two-electrode DFB lasers," Electronics Letters, vol. 24, no. 15, pp. 947-949, Jul. 1988.

Kuznetsove, 1988: M. Kuznetsov, "Theory of wavelength tuning in two-segment distributed feedback lasers," IEEE Journal of Quantum Electronics, vol. 24, no. 9, pp. 1837–1844, Sep. 1988.

Laakso et al., 2009: A. Laakso, M. Dumitrescu, J. Viheriälä, J. Karinen., M. Suominen, and M. Pessa, "Optical modeling of laterally-corrugated ridge-waveguide gratings," Optical and Quantum Electronics, vol. 40, no. 11-12, pp. 907-920, Apr. 2009.

Las2D, 2006: LAS2D software, Laboratoire d'Optoélectronique, École Polytechnique de Montréal, Montréal, QC, Canada.

Leclerc et al., 1989: D. Leclerc, J. Jacquet, D. Sigogne, C. Labourie, Y. Louis, C. Artigue, and J. Benoit, "Three-electrode DFB wavelength tunable FSK transmitter at 1.53 μm," Electronics Letters, vol. 25, no. 1, pp. 45-47, Jan. 1989.

Lehnhardt et al., 2010: T. Lehnhardt, S. Hofling, M. Kamp, L. Worschech, and A. Forchel, "Tunable Long Wavelength (~2.8 μm) GaInAsSb–GaSb Quantum-Well Binary Superimposed Grating Lasers," IEEE Photonics Technology Letters, vol. 22, no. 22, pp. 1662-1664, Nov. 2010.

Li et al., 2014: W. Li, X. Li, and W.-P. Huang, "A traveling-wave model of laser diodes with consideration for thermal effects", Optical and Quantum Electronics, vol. 39, pp. 709-724, Apr. 2004.

Li, 2009: X. Li, Optoelectronic Devices - Design, Modeling, and Simulation. Cambridge University Press (2009).

Li et al., 2000: W. Li, W.P. Huang, X. Li, and J. Hong, "Multiwavelength gain-coupled DFB laser cascade: design modeling and simulation," IEEE Journal of Quantum Electronics, vol. 36, no. 10, pp. 1110-1116, Oct. 2000.

Li et al., 1998: X. Li, A. D. Sadovnikov, W.-P. Huang, and T. Makino, "A physics-based three-dimensional model for distributed feedback laser diodes," IEEE Journal of Quantum Electronics, vol. 34, no. 9, pp. 1545-1553, Sep. 1998.

Liau et al., 1985: Z. L Liau, D. C. Flanders, J. N. Walpole, and N. DeMeo, "A novel GaInAsP/InP distributed feedback laser," Applied Physics Letters, vol. 46, no. 3, pp. 221-223, Feb. 1985.

Liou et al., 1987: K. Y. Liou, N. K. Dutta, and C. A. Burrus, "Linewidth narrowed distributed feedback injection lasers with long cavity length and detuned Bragg wavelength," Applied Physics Letters, vol. 50, no. 9, pp. 489-491, Mar. 1987.

Liu et al., 2014: B. Liu, L. Zhang, X. Xin, and L. Liu, "Flexible generation of optical nonuniform bit-mapping signal based on InP transmitter module," Optics Letters, vol. 39, no. 2, pp. 220-223, Jan. 2014.

Marcenac, 1994: D. D. Marcenac, Fundamentals of laser modelling, PhD Dissertation, University of Cambridge, UK, 1994.

Marcenac and Carroll, 1993: D. D. Marcenac, and J. E. Carroll, "Quantum-mechanical model for realistic Fabry-Perot lasers," IEE Proceedings J Optoelectronics, vol. 140, no. 3, pp. 157-171, Jun. 1993.

Martin et al., 1994: R. D. Martin, S. Forouhar, S. Keo, R. J. Lang, R. G. Hunsperger, R. Tiberio, and P. F Chapman, "InGaAs-GaAs-AlGaAs laterally-coupled distributed feedback (LC-DFB) ridge laser diode," Electronics Letters, vol. 30, no. 13, pp. 1058-1060, Jun. 1994.

Martin et al., 1995: R. D. Martin, S. Forouhar, S. Keo, R. J. Lang, R. G. Hunsperger, R. C Tiberio, and P. F. Chapman, "CW performance of an InGaAs-GaAs-AlGaAs laterally-coupled distributed feedback (LC-DFB) ridge laser diode," IEEE Photonics Technology Letters, vol. 7, no. 3, pp. 244-246, Mar. 1995.

Mercer, 1991: L. B. Mercer, "1/f frequency noise effects on self-heterodyne linewidth measurements," Journal of Lightwave Technology, vol. 9, no. 4, pp. 485-493, Apr. 1991.

Miller et al., 1991: L. M. Miller, J. T. Verdeyen, J. J. Coleman, R. P. Bryan, J. J. Alwan, K. J. Beernink, J. S. Hughes, and T. M. Cockerill, "A distributed feedback ridge waveguide quantum well heterostructure laser," IEEE Photonics Technology Letters, vol. 3, no. 1, pp. 6-8, Jan. 1991.

Millet et al., 2011: R. Millett, K. Dridi, A. Benhsaien, H. Schriemer, K. Hinzer, and T. Hall, "Fabrication-tolerant 1310 nm laterally coupled distributed feedback lasers with high side mode suppression ratios," Photonics and Nanostructures – Fundamentals and Applications, vol. 9, no. 2, pp. 111-118, Apr. 2011.

Millet et al., 2010: R. Millet, K. Hinzer, A. Benhsaien, T. J. Hall, and H. Schriemer, "The impact of laterally coupled grating microstructure on effective coupling coefficients", Nanotechnology, vol. 21, no. 13, pp. 13401-13405, Apr. 2010.

Millet et al., 2008a: R. R. Millett, K. Hinzer, T. J. Hall, and H. Schriemer, "Simulation Analysis of Higher Order Laterally-Coupled Distributed Feedback Lasers," IEEE Journal of Quantum Electronics, vol. 44, no. 12, pp. 1145-1151, Dec. 2008.

Millet et al., 2008b: R. Millett, K. Hinzer, T. Hall, and H. Schriemer, "Fabrication-tolerant higher order laterally coupled distributed feedback lasers," Proc. SPIE 7099, Photonics North 2008, 70991P

Millet et al., 2008c: R. Millett, H. Awad, M. Poirier, V. I. Tolstikhin, T. Hall, K. Hinzer, and H. Schriemer, "Design and fabrication of a λ/4 phase-shifted 1310 nm laterally-coupled distributed-feedback laser," in proceedings of Lasers and Electro-Optics and Quantum Electronics and Laser Science (CLEO/QELS) conference, San Jose, California, paper JThA20, May 2008.

Mobarhan, 1999: K.S. Mobarhan, Test and characterization of laser diodes: determination of principal parameters, Newport Photonics Instrumentation and Measurement Application Note No. 1, http://www.newport.com/servicesupport/PDF_Files/APPNOTE1.pdf.

Morthier and Vankwikelberge, 1997: G. Morthier and P. Vankwikelberge, Handbook of Distributed Feedback Laser Diodes (Artech House, Inc., 1997),

Morthier et al., 1990: G. Morthier, K. David, P. Vankwikelberge and R. Baets, "A new DFB-laser diode with reduced spatial hole-burning," IEEE Photonics Technology Letters, vol. 2, no. 6, pp. 388-390, Jun. 1990.

Muller et al., 2002: M. Muller, F. Klopf, M. Kamp, J. –P. Reithmaier, and A. Forchel, "Wide range tunable laterally coupled distributed-feedback lasers based on InGaAs-GaAs quantum dots," IEEE Photonics Technology Letters, vol. 14, no. 9, pp. 1246-1248, Sep. 2002.

Muller et al., 2001: M. Muller, M. Kamp, A. Forchel, and J. -L Gentner, "Wide-range-tunable laterally coupled distributed feedback lasers based on InGaAsP–InP," Applied Physics Letters, vol. 79, no. 17, pp. 2684-2686, Oct. 2001.

Murata et al., 1987: S. Murata, I. Mito, and K. Kobayashi, "Spectral characteristics for 1.5 μm DBR laser with frequency-tuning region," IEEE Journal of Quantum Electronics, vol. 23, no. 6, pp. 835-838, Jun. 1987.

Naderi et al., 2010: N. A. Naderi, F. Grillot, K. Yang, J. B. Wright, A. Gin, and L. F. Lester, "Two-color multi-section quantum dot distributed feedback laser," Optics Express, vol. 18, no. 26, pp. 27028-27035, Dec. 2010.

Nagarajan et al., 2005: Nagarajan, R.; Joyner, C.H.; Schneider, R.P.; Bostak, J.S.; Butrie, T.; Dentai, A.G.; Dominic, V.G.; Evans, P.W.; Kato, M.; Kauffman, M.; Lambert, D. J H;

Mathis, S.K.; Mathur, A.; Miles, R.H.; Mitchell, M.L.; Missey, M.J.; Murthy, S.; Nilsson, A.C.; Peters, F.H.; Pennypacker, S.C.; Pleumeekers, J.L.; Salvatore, R.A.; Schlenker, R.K.; Taylor, R.B.; Huan-Shang Tsai; Van Leeuwen, M.F.; Webjorn, J.; Ziari, M.; Perkins, D.; Singh, J.; Grubb, S.G.; Reffle, M.S.; Mehuys, D.G.; Kish, F.A.; Welch, D.F., "Large-scale photonic integrated circuits," IEEE Journal of Selected Topics in Quantum Electronics, vol. 11, no. 1, pp. 50-65, Jan.-Feb. 2005.

Nasim and Jamil, 2014: H. Nasim, and Y. Jamil, "Diode lasers: From laboratory to industry," Optics and Laser Technology, vol. 56, pp. 211-222, Mar. 2014.

Ogita et al., 1987: S. Ogita, M. Yano, H. Ishikawa, and H. Imai, "Linewidth reduction in DFB laser by detuning effect," Electronics Letters, vol. 23, no. 8, pp. 393-394, Apr. 1987.

Okoshi et al., 1980: T. Okoshi, K. Kikuchi, and A. Nakayama, "Novel method for high resolution measurement of laser output spectrum," Electronics Letters, vol. 16, no. 16, pp. 630-631, Jul. 1980.

Pan et al., 1990: X. Pan, H. Olesen, and B. Tromborg, "Spectral linewidth of DFB lasers including the effects of spatial holeburning and nonuniform current injection," IEEE Photonics Technology Letters, vol. 2, no. 5, pp. 312-315, May 1990.

Petermann et al., 1979: K. Petermann, "Calculated spontaneous emission factor for double-heterostructure injection lasers with gain-induced waveguiding," IEEE Journal of Quantum Electronics, vol.15, no.7, pp. 566- 570, Jul. 1979.

Pfau et al., 2009: T. Pfau, S. Hoffmann, R. Noe, "Hardware-Efficient Coherent Digital Receiver Concept With Feedforward Carrier Recovery for M -QAM Constellations," Journal of Lightwave Technology, vol. 27, no. 8, pp. 989-999, Apr. 2009.

Pozzi et al., 2006: F. Pozzi, R. M. De La Rue, and M. Sorel, "Dual-Wavelength InAlGaAs–InP Laterally Coupled Distributed Feedback Laser," IEEE Photonics Technology Letters, vol. 18, no. 24, pp. 2563-2565, Dec. 2006.

Rabinovich et al., 1989: W. S. Rabinovich and B. J. Felfdman, "Spatial Hole Burning Effects in Distributed Feedback lasers," IEEE Journal of Quantum Electronics, vol. 25, no. 1, pp. 20-30, Jan. 1989.

Reid et al., 2003: B. Reid, M. Poirier, S. R. Das, D. Ducharme, R. Dowlatshahi, S. Langstaff, N. S. Kim, R. Kuchibhatia, and S. D. Tabriz, "Narrow linewidth and high power distributed feedback lasers fabricated without a regrowth step," in proceedings of the European Conference on Optical Communication (ECOC), paper Th1.6, Rimini, Italy, Sep. 2003.

Sakai et al., 1982: K. Sakai, K. Utaka, S. Akiba, and Y. Matsushima, "1.5 μm range InGaAsP/InP distributed feedback lasers," IEEE Journal of Quantum Electronics, vol. 18, no. 8, pp. 1272-1278, Aug. 1982.

Salhi et al., 2006: A. Salhi, D. Barat, D. Romanini, Y. Rouillard, A. Ouvrard, R. Werner, J. Seufert, J. Koeth, A. Vicet, and A. Garnache, "Single-frequency Sb-based distributed-feedback lasers emitting at 2.3 μm above room temperature for application in tunable diode laser absorption spectroscopy," Applied Optics, vol. 45, no. 20, pp. 4957-4965, Jul. 2006.

Schreiner et al., 2001: R. Schreiner, P. Nagele, M. Korbl, A. Groning, J. L. Gentner, and H. Schweizer, "Monolithically integrated tunable laterally coupled distributed-feedback lasers," IEEE Photonics Technology Letters, vol. 13, no. 12, pp. 1277-1279, Dec. 2001.

Seimetz, 2009: Seimetz, Matthias, "High-Order Modulation for Optical Fiber Transmission", Springer Berlin Heidelberg, 2009

Seimetz, 2008: M. Seimetz, "Laser Linewidth Limitations for Optical Systems with High-Order Modulation Employing Feed Forward Digital Carrier Phase Estimation," in proceedings

of Optical Fiber Communications (OFC/NFOEC) conference, paper OTuM2, San Diego, California, Feb. 2008.

Shams-Zadeh-Amiri et al., 2000: A. M. Shams-Zadeh-Amiri, J. Hong; X. Li; and W-P. Huang, "Second- and higher order resonant gratings with gain or loss-Part II: designing complex-coupled DFB lasers with second-order gratings," IEEE Journal of Quantum Electronics, vol. 36, no. 12, pp. 1431-1437, Dec. 2000.

Sode et al., 1987: H. Sode, Y. Kotaki, H. Sudo, H. Ishikawa, S. Yamakoshi, and H. Imai, "Stability in single longitudinal mode operation in GaInAsPflnP phaseadjusted DFB lasers," IEEE Journal of Quantum Electronics, vol. 23, no. 6, pp. 804-814, Jun. 1987

Soldo et al., 2009: M. Soldo, N. Gibbons, and G. Giuliani, "Generation of a narrow linewidth mm-wave signal from two phase-locked DFB lasers that are mutually coupled via four wave mixing," in Proceedings of Lasers and Electro-Optics and European Quantum Electronics Conference, paper JThE32, May-Jun. 2009.

Spiessberger et al., 2010: S. Spiessberger, M. Schiemangk, A. Wicht, H. Wenzel, O. Brox, and G. Erbert, "Narrow Linewidth DFB Lasers Emitting Near a Wavelength of 1064 nm," Journal of Lightwave Technology, vol. 28, no.17, pp. 2611-2616, Sep. 2010.

Streifer et al., 1976: W. Streifer, D. R. Scifres, and R. Burnham, "Analysis of grating-coupled radiation in GaAs:GaAlAs lasers and waveguides - I," IEEE Journal of Quantum Electronics, vol.12, no.7, pp. 422-428, Jul. 1976.

Streifer et al. 1977: W. Streifer, D. R. Scifres, and R. Burnham, "Coupled wave analysis of DFB and DBR lasers," IEEE Journal of Quantum Electronics, vol. 13, no. 4, pp. 134-141, Apr. 1977.

Telkkala et al., 2011: J. Telkkala, J. Viheriala, A. Aho, P. Melanen, J. Karinen, M. Dumitrescu, and M. Guina, "Narrow linewidth laterally-coupled 1.55 µm DFB lasers fabricated using nanoimprint lithography," Electronics Letters, vol. 47, no. 6, pp. 400-401, Mar. 2011.

Tolstikhin et al., 2009a: V. I. Tolstikhin, R. Moore, K. Pimenov, Y. Logvin, F, Wu, and C. D. Watson, "One-step growth optical transceiver PIC in InP," in proceedings of 35th European Conference on Optical Communication (ECOC), Vienna, Austria, Sept. 2009.

Tolstikhin et al., 2009b: V. I. Tolstikhin, C. D. Watson, K. Pimenov, R. Moore, Y. Logvin, and F. Wu, "Laterally Coupled DFB Lasers for One-Step Growth Photonic Integrated Circuits in InP," IEEE Photonics Technology Letters, vol. 21, no. 10, pp. 621-623, May 2009.

Usami and Akiba, 1989: M. Usami, and S. Akiba, "Suppression of longitudinal spatial hole-burning effect in λ/4-shifted DFB lasers by nonuniform current distribution," IEEE Journal of Quantum Electronics, vol. 25, no. 6, pp. 1245-1253, Jun. 1989.

Vankwikelberge et al., 1990: P. Vankwikelberge, G. Morthier, and R. Baets, "CLADISS—A longitudinal multimode model for the analysis of the static, dynamic and stochastic behavior of diode lasers with distributed feedback," IEEE Journal of Quantum Electron., vol. 26, no. 10, pp. 1728–1741, Oct. 1990.

Walpole et al., 1976: J. N. Walpole, A. R. Calawa, S. R. Chinn, S. H. Groves, and T. C. Harman, "Distributed feedback Pb1-x SnxTe double-heterostructure lasers," Applied Physics Letters, vol. 29, no. 5, pp. 307-309, Sep. 1976.

Wang et al., 2005: J. Wang, J. –B. Tian, P. –F. Cai, B. Xiong, C. –Z. Sun, and Y. Luo,"1.55-µm AlGaInAs-InP laterally coupled distributed feedback laser," IEEE Photonics Technology Letters, vol. 17, no. 7, pp. 1372-1374, Jul. 2005.

Watanabe et al., 1998: Y. Watanabe, N. Chen, K. Takei, K. Chijuma, N. Futakuchi, and Y. Nakano, "Laterally coupled strained MQW ridge waveguide distributed-feedback laser

diode fabricated by wet-dry hybrid etching process," IEEE Photonics Technology Letters, vol. 10, no. 12, pp. 1688-1690, Dec. 1998.

Wenzel, 2003: H. Wenzel, "Green's function based simulation of the optical spectrum of multisection lasers," IEEE Journal of Selected Topics in Quantum Electronics, vol. 9, no. 3, pp. 865-871, May-Jun. 2003.

Whiteaway et al., 1989: J. E. A. Whiteaway, G. H. B. Thompson, A. J. Collar, and C. J. Armistead, "The design assessment of λ/4 phase-shifted DFB laser structures," IEEE Journal of Quantum Electronics, vol.25, no.6, pp. 1261-1279, Jun. 1989.

Wunshe et al., 1993: H. J. Wunshe, U. Bandelow, and H. Wenzel, "Calculation of combined lateral and longitudinal spatial hole burning in λ/4 shifted DFB lasers," IEEE Journal of Quantum Electronics, vol. 29, no. 6, pp. 1751-1760, Jun. 1993.

Wong et al., 1993: V. V. Wong, W. -Y. Choi, J. M. Carter, C. G. Fonstad, H. I. Smith, Y. Chung, and N. Dagli, "Ridge-waveguide sidewall-grating distributed feedback structures fabricated by x-ray lithography," Journal of Vacuum Science & Technology B: Microelectronics and Nanometer Structures, vol. 11, no. 6, pp. 2621-2624, Nov. 1993.

Yeo et al., 2010: C. I. Yeo S. J. Jang, J. S. Yu, and T. T. Lee, "1.3 μm Laterally Tapered Ridge Waveguide DFB Lasers With Second-Order Cr Surface Gratings," IEEE Photonics Technology Letters, vol. 22, no. 22, pp. 1668-1670, Nov. 2010.

Yoshikuni and Motosugi, 1987: Y. Yoshikuni, and G. Motosugi, "Multielectrode distributed feedback laser for pure frequency modulation and chirping suppressed amplitude modulation," Journal of Lightwave Technology, vol. 5, no. 4, pp. 516-522, Apr. 1987.

Yoshikuni et al., 1986a: Y. Yoshikuni, K. Oe, G. Motosugi, and T. Matsuoka, "Broad wavelength tuning under single-mode oscillation with a multi-electrode distributed feedback laser," Electronics Letters, vol. 22, no. 22, pp. 1153-1154, Oct. 1986.

Yoshikuni and Motosugi, 1986b: Y. Yoshikuni and G. Motosugi, "Independent modulation in amplitude and frequency regimes by a multielectrode distributed feedback laser," in Proceeding of the 9th conference of Optical Fiber Communications, Atlanta, GA, paper TuF1, Feb. 1986.

Zanola et al., 2013: M. Zanola, M. J. Strain, G. Giuliani, and M. Sorel, "Monolithically Integrated DFB Lasers for Tunable and Narrow Linewidth Millimeter-Wave Generation," IEEE Journal of Selected Topics in Quantum Electronics, vol. 19, no. 4, pp. 1500406-1500406, Jul.-Aug. 2013.

Zhang et al., 1994: L. M. Zhang, S.F. Yu, M.C. Nowell, D. D. Marcenac, J. E. Carroll, and R.G.S. Plumb, "Dynamic analysis of radiation and side-mode suppression in a second-order DFB laser using time-domain large-signal traveling wave model," IEEE Journal of Quantum Electronics, vol. 30, no. 6, pp. 1389-1395, Jun. 1994.

Zhang et al., 1992: L. M. Zhang, and J. E. Carroll, "Large-signal dynamic model of the DFB laser," IEEE Journal of Quantum Electronics, vol. 28, no. 3, pp. 604-611, Mar. 1992.

Zhong et al., 2004a: Y. Zhong, X. Zhu, G. Song, Y. Huang, and L. Chen, "Effect of metal contact's reflection on the effective coupling coefficient of second-order DFB laser diodes," Microwave and Optical Technology Letters, vol. 42, no. 4, pp. 339-342, Aug. 2004.

Zhong et al., 2004b: Y. Zhong, X. Zhu, G. Song, Y. Huang, and L. Chen, "Two-dimensional simulation of high-order laterally-coupled GaAs-AlGaAs DFB laser diodes," Semiconductor Science and Technology, vol. 19, no. 8, pp. 971–974, Jun. 2004.

Appendix A|

Extraction of the modal gain

The optical gain is an important parameter that relates the output characteristics (*e.g.* threshold current) of a laser diode to its semiconductor structure physical properties. The material optical gain, G, is related to the modal optical gain, g, as follows (Casey and Panish, 1978):

$$g(\lambda) = \Gamma G(\lambda) - \alpha_{total} \tag{A.1}$$

where Γ is the optical confinement factor, which measures the overlap between the transverse optical mode and the active layer; α_{total} is the total optical loss, which consists of internal loss (α_{int}) and mirror loss (α_{mirr}):

$$\alpha_{total} = \alpha_{int} + \alpha_{mirr} = \alpha_{int} + \frac{1}{2L}\ln(\frac{1}{R_1 R_2}) \tag{A.2}$$

where R_1 and R_2 are the mirror reflectivities, L is the laser cavity length.

Despite that different techniques can be used for the measurements of the optical gain, we have applied the Hakki-Paoli method (Hakki and Paoli, 1975) in this thesis. The extraction of the modal gain has been carried out from the sub-threshold optical spectra (*i.e.* amplified spontaneous emission) of Fabry-Perot (FP) devices – fabricated in the same wafer as the corrugated ridge waveguide DFB lasers. In general better results would be obtained for shorter FP cavities since they have a "clean" ASE spectrum (*i.e.* the intensity contrast is much clear for accurate reading). In this work, we extracted the gain from a 500 µm-long FP device (with a ridge width of 4 µm, $I_{threshold}$=30mA). An example of ASE spectrum is shown in Fig.A. 1(a), where the FP device has been biased at 24 mA.

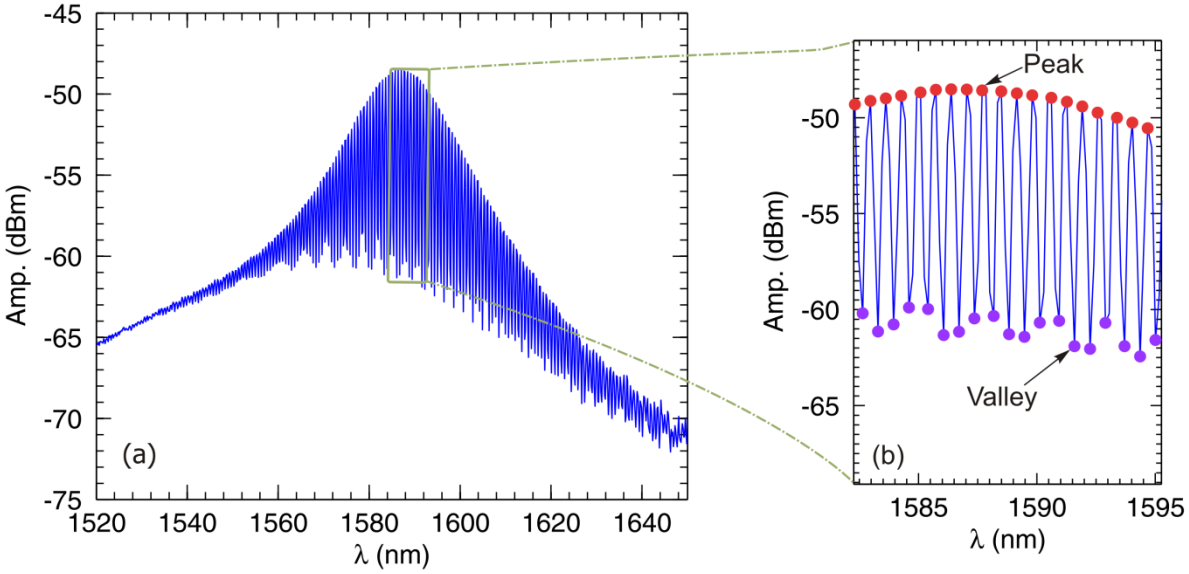

Fig.A. 1. (a) Example of sub-threshold optical spectrum measured at 24 mA for a FP device; (b) zoom around 1590 nm that shows the different peaks and valleys

The H-P technique consists of (Hakki and Paoli, 1975):

- Calculating the depth of modulation dm_i as defined in (A.3) by localising the optical intensity peaks (P_i) and valleys (V_i) from the amplified spontaneous emission spectrum, as shown in Fig.A. 1(b).

$$dm_i = \frac{P_i + P_{i+1}}{2V_i} \tag{A. 3}$$

- Once the depth of modulation is calculated, the modal gain can be determined from (A.4) as:

$$g_{mod} = \frac{1}{L}\ln\frac{{dm_i}^{1/2}+1}{{dm_i}^{1/2}-1} + \frac{1}{L}\ln\sqrt{R_1R_2} \tag{A. 4}$$

In (A. 4) L is the cavity length, R_1 and R_2 are facet reflectivities from the right and left facets, respectively. In general in as-cleaved FP devices we can set R_1=R_2=R, which can be determined as:

$$R = \frac{(n_{eff} - 1)^2}{(n_{eff} + 1)^2} \tag{A. 5}$$

where n_{eff} is the effective index of reflection and is determined as:

$$n_{eff} = \frac{\lambda^2}{2L\Delta\lambda} \tag{A. 6}$$

λ is the emission wavelength, Δλ is the longitudinal mode spacing in the FP cavity.

An example of extracted modal gain is shown in Fig.A. 2, where its maximum peaks around 1590 nm at 25°C, with a 3-dB bandwidth of ~ 20 nm.

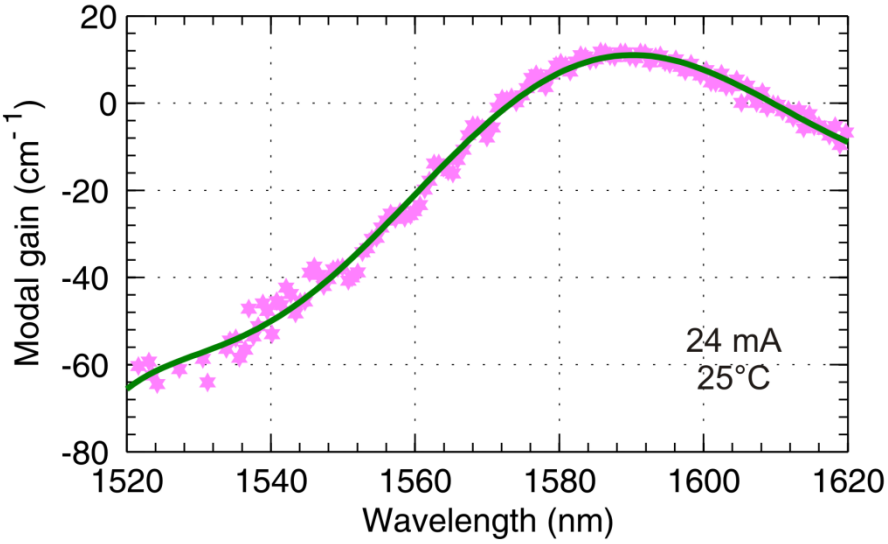

Fig.A. 2. Extracted optical modal gain for a FP device ($I_{threshold}$=30mA) with a cavity length of 500 µm biased at 24 mA at 25°C.

The internal loss α_{int} can be estimated by looking into higher wavelengths side (or into lower photon energy side), where the modal gain converge to α_{int}. For better accuracy one can extract the gain for various sub-threshold currents and do an average on the modal gain obtained at longer wavelengths. Doing so, we observed that all the modal gain almost converge into a value of ~ 11 cm^{-1},

which represents the internal loss for the current FP device. The mirror loss α_{mirr}can be estimated by determining the peak modal gain at lasing threshold. This value is found to be ~19.4 cm^{-1}, which is in a good agreement with the calculated $\alpha_{mirr} = \frac{1}{L}\ln\left(\frac{1}{R}\right)$ of 20 cm^{-1}, where R is calculated by (A.5).

One major observation that can be drawn from the extracted gain in Fig.A. 2 is the spectral shift of about ~ 40 nm between the gain peak wavelength (~ 1590 nm) and the resonance wavelength (1550 nm). We strongly believe that this could be a non-negligible fact behind the higher that anticipated threshold current observed in all of the CRW-DFB characterized in this thesis.

Appendix B|
Linewidth determination

In this thesis, the linewidth measurements of the CRW lasers have been carried out using the delayed self-heterodyne (DSH) technique, which has been originally proposed by Okoshi *et al.* (Okoshi *et al.*, 1980). It consists of an optical interferometer where the optical signal from the laser to be tested is delayed and mixed with frequency-shifted replica before being detected by a photodetector. This gives rise to a beat tone at low frequencies (at the frequency shift) where analysis can be performed with electronic instrumentation. The DSH technique is simple if compared to the heterodyne one because it avoids the requirement of a separate, stable, and narrow linewidth local oscillator laser source (i.e. reference laser). It offers more accuracy than the homodyne techniques, which allow linewidth determination around DC. It is well known that in this very low frequency window commercial electrical spectrum analyzers have high noise levels. Adding to this that the laser intensity noise (*e.g.* 1/f) is strong in this region, the measurement accuracy may be worse. Shifting the RF beat tone away from the DC, as in the DSH technique, would therefore improve the linewidth measurement (Derickson, 1998).

Fig.B. 1 shows the experimental setup for the DSH technique. It basically consists of an interferometer where the beam is split into two portions. One portion is delayed by a 20 km fiber delay line, and the other portion is frequency shifted by an acousto-optic modulator (AOM), which is driven at a constant frequency (110 MHz). The used fiber delay line allows a resolution of 10 kHz for the experimental setup. The superimposition of the two beams through a fiber-optic coupler is then detected by a photo-detector (PD). Its photo-current power spectrum is then analyzed by an electrical spectrum analyzer (ESA) in order to extract the linewidth. In addition, an optical isolator has been used to minimize the back-reflections from the optical fiber into the laser under test.

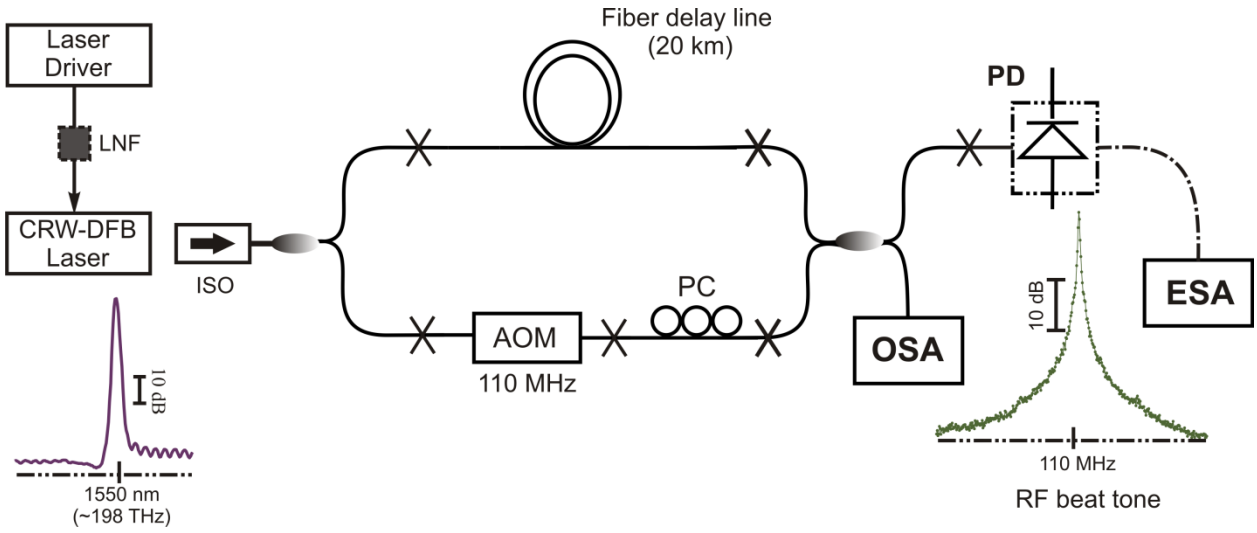

Fig.B. 1. The experimental setup based on the delayed self-heterodyne interferometric technique used for linewidth determination. (LNF: low noise filter; ISO: isolator; AOM: acousto-optic modulator; PC: polarization controller; OSA: optical spectrum analyzer; PD: photo-diode; ESA: electrical spectrum analyser).

Precautions have been undertaken in order to reduce any possible extrinsic noise to which the setup is sensitive. We made sure that all components/equipment, including fiber path cords, have been well fixed and taped into a vibration isolation optical table. Another important precaution consisted in the appropriate selection of the laser driver. Indeed, any input external noise to the laser will be translated into the RF beat tone by broadening its spectrum. A comparison between three different commercial sources (Agilent B2912A, Keithley 2400, and ILX LDX-3620B) is shown in Fig.B. 2. It is clear from this figure how the noise in laser drivers affects the RF beat tone at the electrical spectrum analyzer. The use of the ultra-low noise gives a close RF beat note response to the actual expected ideal response of a semiconductor laser.

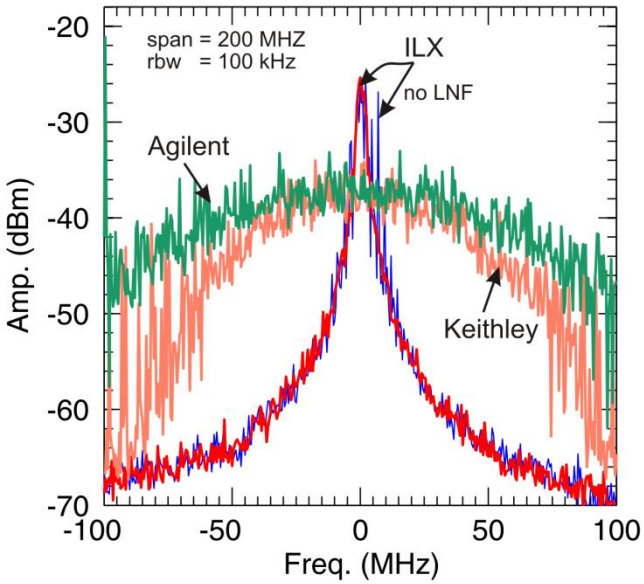

Fig.B. 2. Effect of the laser driving source on the RF beat note for a 1500 μm-long CRW-DFB laser biased at 200 mA using the setup as in Fig.B. 1. The laser sources are Agilent B2912A, Keithley 2400, ILX LDX-3620B.

The ILX- LDX-3620B unit is an ultra-low noise current source that has a built-in battery with its charger. Fig.B. 3(a-b-c) show the RF beat note obtained when the battery is OFF (*i.e.* the AC power switch of the unit is turned ON: the battery is charging while permitting full use of the ILX unit. Much noise is present in this configuration). Fig.B. 3(d-e-f) show the RF beat note recorded when the battery is ON (*i.e.* no AC power supplied to the unit: AC power switch turned OFF). In both cases, the effect of using an in-line low noise filter (LNF-320) is also shown, where the noise is reduced in either configurations. We would like to emphasize that only one source was available on a loan-basis from Communications Research Centre (CRC) for short period of time.

The effect of the isolator on the RF beat tone was also studied as shown in Fig.B. 4. It is clear that removing the isolator would result in strong feedback to the laser under test, which in turn will narrow further the linewidth. The effect of running the battery ON/OFF and the use of the LNF are also shown.

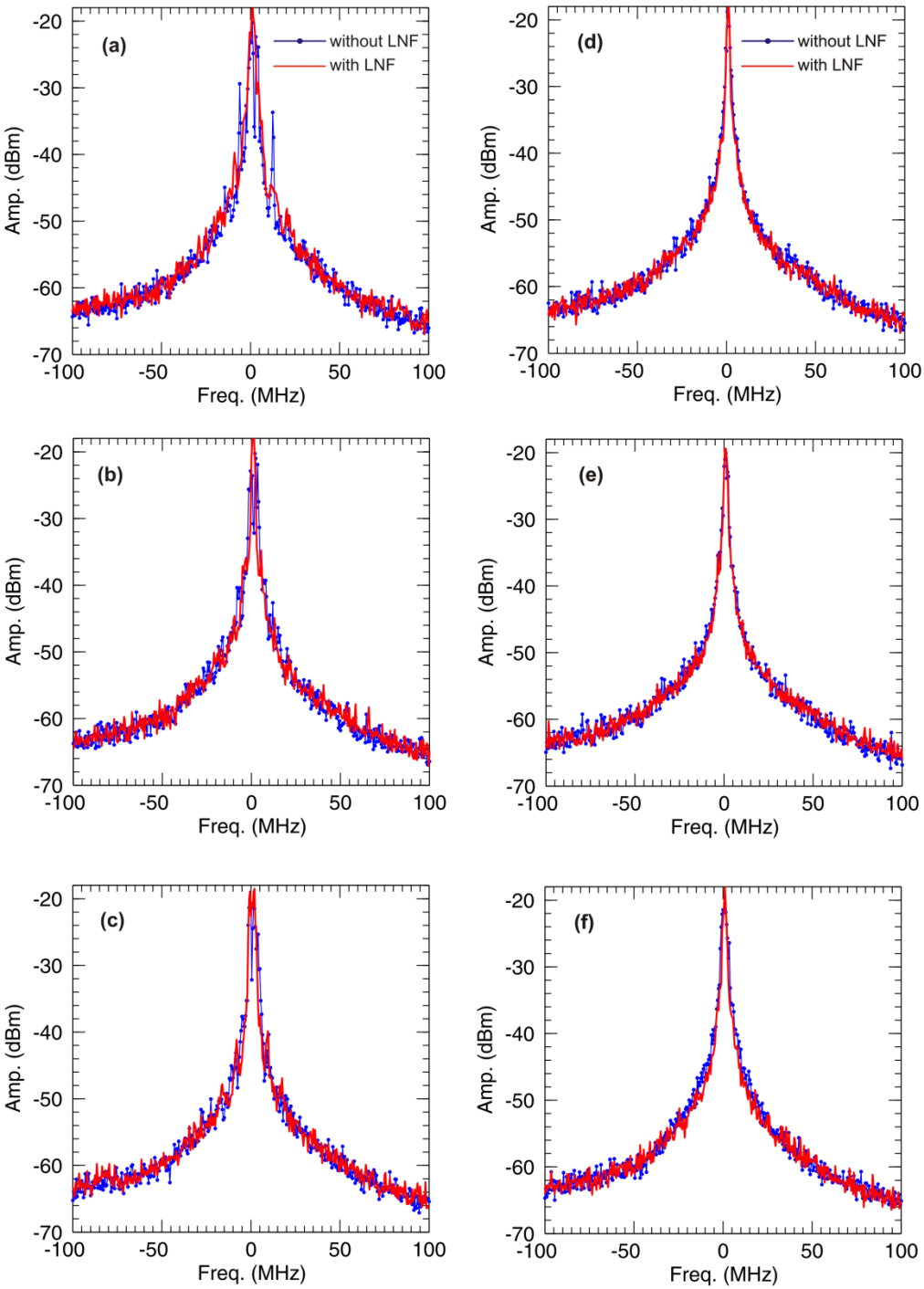

Fig.B. 3. Battery mode effect on the RF beat note spectrum; (a-b-c): battery OFF, and (d-e-f): battery ON. The effect of using a low noise filter (LNF) is also shown.

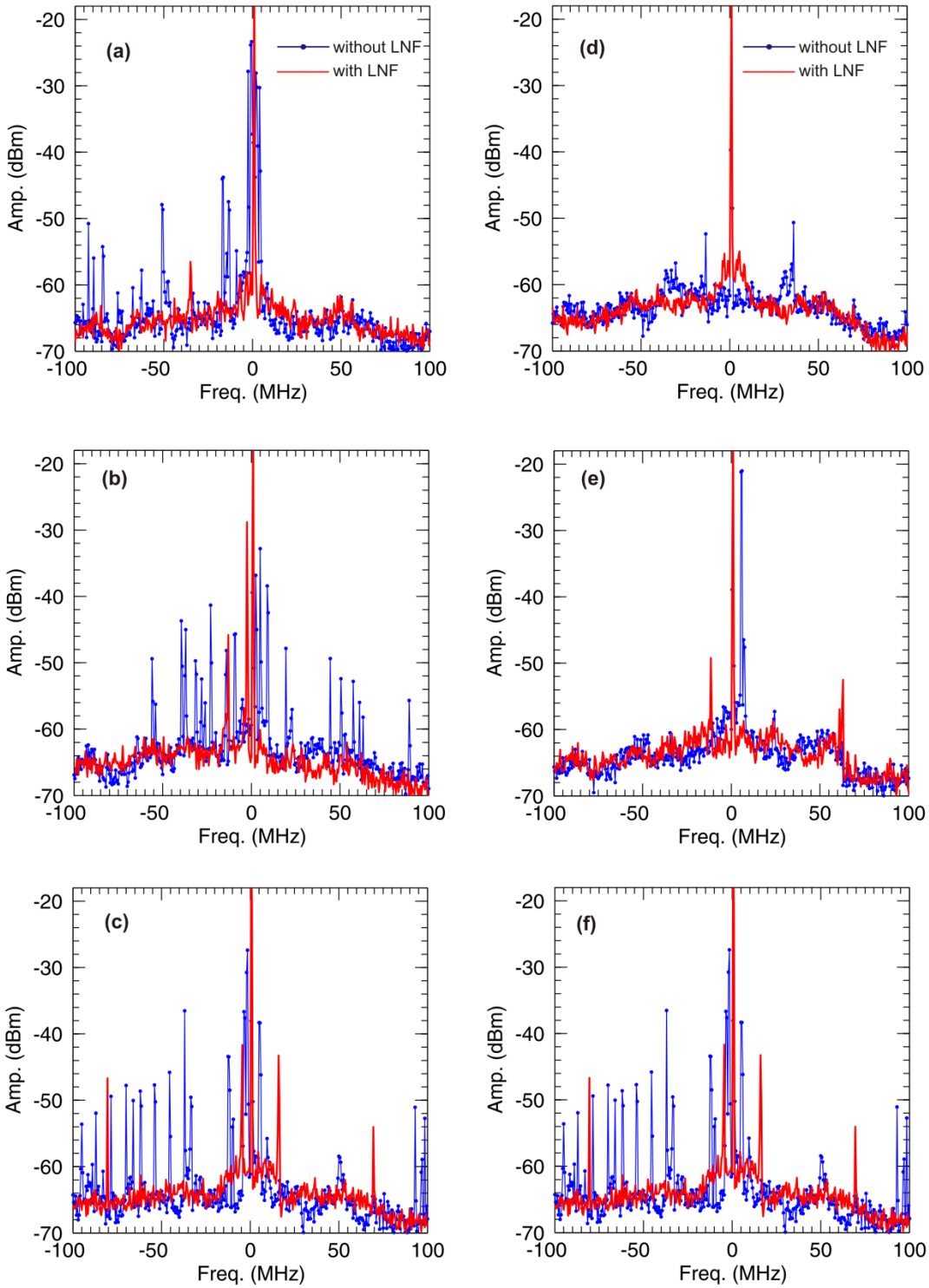

Fig.B. 4. RF beat tone spectrum for 1500 µm-long CRW-DFB laser biased at 200 mA with the isolator removed from the setup in Fig.B. 1: (a-b-c) ILX battery OFF; and (d-e-f) ILX battery ON.

The linewidth measurements were carried out using the setup as in Fig.B. 1. The lasers under test were driven with the ultra-low noise current source (battery ON) together with the LNF. The isolator was also kept connected to avoid back-reflections to the device under test. An example of a measured RF delayed self-heterodyne (DSH) beat tone for a 1500 µm-long CRW laser biased at 220 mA is shown in Fig.B. 5. Fig.B. 5(a) shows a large view for a DSH beat tone spectrum together with the noise floor for the setup (recorder by turning OFF the laser under test. The noise floor is considered to be far enough from the desired response, which means that our measurements were accurate. Fig.B. 5(b) and (c) show a close view around the DSH signal with a span of 200 and 10 MHz, respectively.

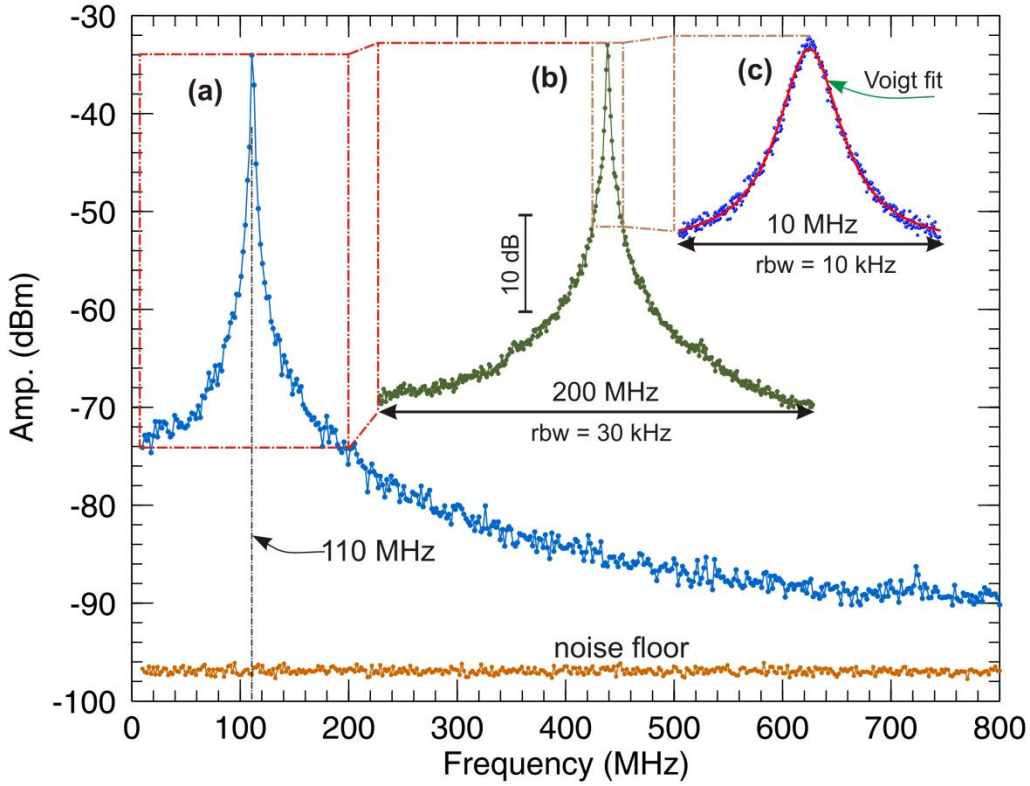

Fig.B. 5. Example of an RF delayed self-heterodyne beat note spectrum for 1500 µm two-electrode CRW laser biased at a total current of 220 mA (Resolution bandwidth in the electrical spectrum analyzer (ESA) is 30 kHz). The noise floor of the setup is also shown. (rbw: ESA resolution bandwidth)

From Fig.B. 5(c), some broadening is observed in the lineshape near the center of the beat note spectrum forcing it to have a non-Lorentzian lineshape. It is rather a Gaussian broadening, which is due to extrinsic (technically avoidable) noise introduced by the immediate environment (Spiessberger *et al.*, 2010; Telkkala *et al.*, 2011). In such situations it is important to know the intrinsic or the real linewidth of the laser under testing. The Voigt profile – a convolution between Gaussian and Lorentzian profiles – allows simultaneous quantification of the effect of extrinsic noise (mapped by the Gaussian part) and the intrinsic linewidth (mapped by the Lorentzian part). We can therefore apply a Voigt fitting procedure (Spiessberger *et al.*, 2010; Telkkala *et al.*, 2011) to the measured normalized RF beat spectrum as illustrated by Fig.B. 6. In this figure the DSH signal was recorded in linear scale rather than in logarithm scale to simplify the application of the Voigt lineshape fitting. In this case the linewidth will be extracted from the Voigt full width at half maximum.

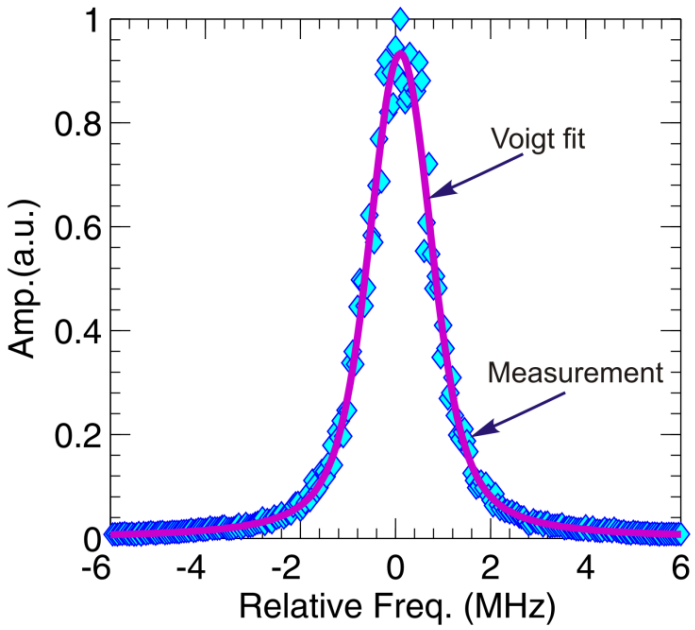

Fig.B. 6. Example of DSH RF beat note for a 1500 µm-long CRW-DFB laser with the Voigt fitting.

In Fig.B. 6 the fitted Voigt profile to the measured RF beat note spectrum gives a full width at half maximum (FWHM) of 1.58 MHz, from which the extracted Lorentzian and Gaussian FWHMs are 0.8 and 1 MHz, respectively.

Given that the DSH technique is used for the linewidth determination, the intrinsic Δv is half the Lorentzian part (Derickson, 1998); i.e. the final intrinsic linewidth is 0.4 MHz.

The fitting has been performed using Matlab® and OriginLab®, where the Voigt function is given by:

$$V = A\frac{2\ln 2}{\pi^{3/2}}\frac{w_L}{w_G^2}\int_{-\infty}^{+\infty}\frac{e^{-t^2}}{\left(\sqrt{\ln 2}\frac{w_L}{w_G}\right)^2+\left(\sqrt{4\ln 2\frac{\nu-\nu_0}{w_G}}-t\right)^2}dt \qquad \text{(B.1)}$$

In this function,

- A is the area of the Voigt peak
- w_L and w_G are the full width at half maximum (FWHM) of the Lorentzian and Gaussian profiles, respectively.
- ν_0 is the line center frequency; in this work it is set as the AOM's frequency (110 MHz).

The function in (B. 1) has been fitted to the experimental data by using a Levenberg-Marquardt (L-M) algorithm in order to adjust the w_G and w_L parameters. The derived Voigt FWHM (w_V) can be computed at the end of the fitting process as follows:

$$w_V = 0.5346w_L + \sqrt{0.2166w_L^2 + w_G^2} \qquad \text{(B. 2)}$$

For multi-electrode devices a precise probing system has been designed, where thin needles controlled via micromanipulators were used in order to provide the injection current to the device under test as shown in Fig.B. 7. Besides, given that only one ultra-low noise current source was available in this work; a small circuit based on current divider was mounted as shown in Fig.B. 8.

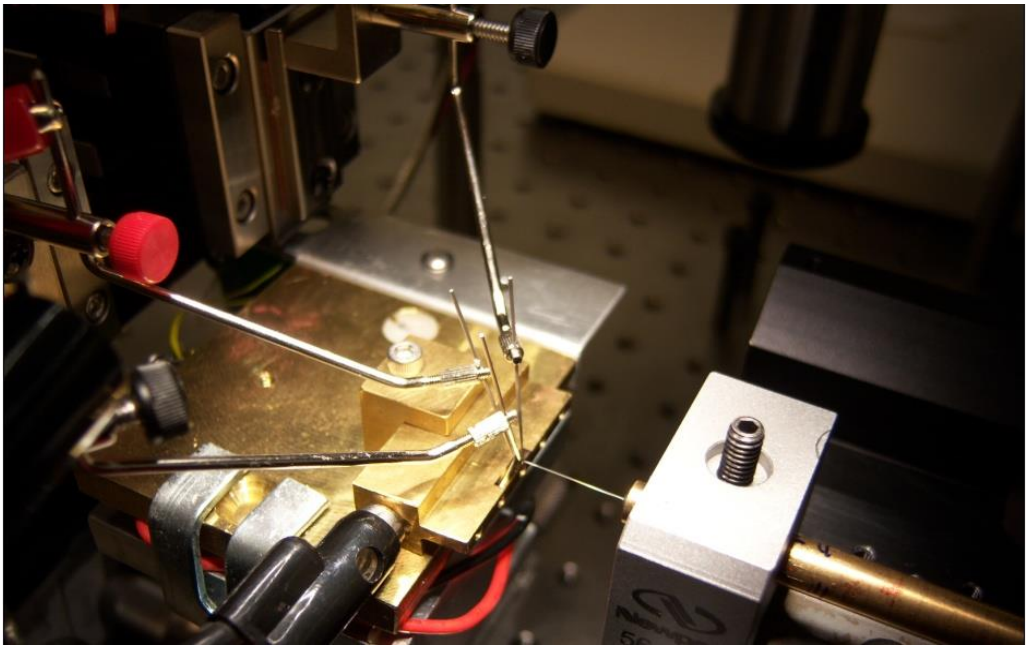

Fig.B. 7. Probing system for multi-electrode CRW-DFB lasers testing

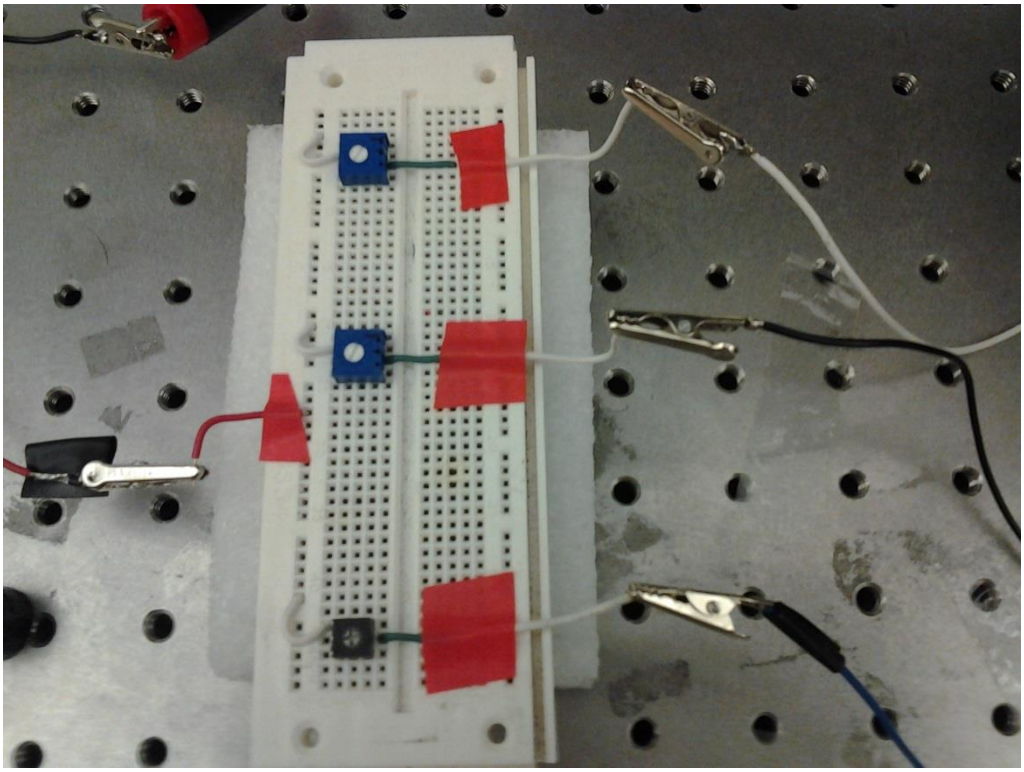

Fig.B. 8. Injection current circuit for the multi-electrode CRW-DFB lasers